The Effect of Juxtaposition of Sandstone and Claystone across Faults on Thermo-elastic Stress Changes and Induced Fault Slip

MSc. Thesis

Esther Zijlstra

TUDelft

The Effect of Juxtaposition of Sandstone and Claystone across Faults on Thermo-elastic Stress Changes and Induced Fault Slip

MSc. Thesis

by

Esther Zijlstra

to obtain the degree of Master of Science in Applied Earth Sciences,
specialized in Geo-Energy Engineering
at the Delft University of Technology,
to be defended publicly on Wednesday July 10, 2024 at 15:30 PM.

Student number:	4849752	
Project duration:	February 12, 2024 – July 10, 2024	
Thesis committee:	Dr. A. M. Muntendam-Bos,	TU Delft, supervisor
	Prof. Dr. Ir. J.-D. Jansen,	TU Delft
	Dr. L. Buijze,	TNO, supervisor

An electronic version of this thesis is available at `http://repository.tudelft.nl/`.

Acknowledgements

I want to give my thanks my daily TNO supervisor Loes Buijze and TU Delft supervisor Annemarie Muntendam-Bos for guiding me through the process of my final project at the TU Delft. Your help and explanations gave me insight and interest in a topic relatively new to me. I'd like to thank Jan-Dirk Jansen for taking place on the committee and giving valuable feedback. And of course my friends and family for their support, not only during my master thesis but throughout my studies in Delft.

Abstract

The presence of faults in the subsurface, crossing geothermal targeted aquifers introduces concerns related to induced seismicity. Improving the understanding of geomechanical processes due to geothermal operations is therefore important. Previous research has indicated that thermally induced stresses can have a significant effect on fault stability, especially in the long term. In depleting gas fields, the effect of fault offset has been studied and found to promote the onset of fault reactivation. However, little research has been conducted on this effect in geothermal reservoirs. This thesis will investigate the effect of juxtaposition of sandstone and claystone across faults on thermo-elastic stress changes and induced fault slip in geothermal projects targeting porous sandstone reservoirs.

This research question will be answered by constructing three different model geometries in a semi-analytical 2D plane-strain model assessing thermo-elastic stress changes and fault slip. The geology and properties of the Pijnacker Geothermie reservoir, located in the West Netherlands Basin and targeting the Delft Sandstone Member as its reservoir rock are used for the input of the model. The three geometries include a model scenario in which sandstone is fully juxtaposed against sandstone, a scenario in which sandstone is fully juxtaposed against claystone and lastly, a scenario with half-a-reservoir-thickness fault offset, juxtaposing sandstone against both sandstone and claystone. These geometries were chosen to represent a fault that experiences cooling on both sides, on a single side and on both sides, but with an offset. A comparison was made between the three model scenarios using base cases and evaluating the differences in stress changes and fault slip. A sensitivity analysis was performed in order to determine the key parameters influencing the results the most. Then, three metrics were extracted from the base cases and plotted against the varying key parameters. These metrics are: the temperature change needed to reactivate the fault, the maximum slip and the slip patch length. Lastly, heterogeneous friction was used in the model in order to assess its effect and make a step towards a slightly more realistic model.

The results showed that the double sided cooling case with fault offset was the most destabilizing configuration, needing the least amount of cooling before reaching the onset of fault reactivation and also consistently experiencing the largest maximum slip. The single sided cooling model scenario is the most stable, however its slip patch length is the most sensitive to variations in key parameters, generating the largest slip length for destabilizing values of the key parameters. The inclusion of heterogeneous friction had a destabilizing effect on all scenarios. As the degree to which sandstone is juxtaposed against sandstone affects the amount of thermo-elastic stress changes and slip a fault experiences, it should be considered to include fault offset when assessing fault slip in geothermal projects. Not including fault offset will likely underestimate the thermo-elastic stress changes and subsequent induced fault slip.

Panther can capture the effect of thermo-elastic stress changes in a first-order assessment on a simple reservoir geometry containing the essential parameters while avoiding extra model complexity.

Further improvements to the model can be made to capture the effect of certain aspects that have been proven to affect thermo-elastic stress changes. These include property contrasts between the reservoir and surrounding rock as well as the addition of clay-rich layers in the sandstone formation and vice versa. Further geological work could be performed to decrease the uncertainty around the location of the fault and its dip angle.

Contents

List of Figures

List of Tables

List of Variables

Variable	Symbol
Normal stress	σ
Largest principle stress	σ_1
Smallest principle stress	σ_3
Angle between σ_1 and σ_3	δ
Shear stress	τ
Effective stress	σ'
Pore pressure	P_p
Cohesion	C
Friction coefficient	f_s
Angle of internal friction	ϕ
Stress path parameter	γ
Biot's coefficient	α
Thermal expansion coefficient	η
Shear modulus	μ
Poisson's ratio	ν
Young's modulus	E
Thermal diffusivity	κ_T
Rock density	ρ_r
Fluid density	ρ_f
Thermal conductivity	K
Heat capacity rock	C_r
Heat capacity fluid	C_f
Aquifer or reservoir thickness	h
Mass injection rate	$\dot{m}$

Table 1: List of variables

1 Introduction

The demand for greener and sustainable sources of energy is growing and one promising source is geothermal energy (Geothermie & DAGO, 2021). As geothermal energy is not season or weather dependent and can produce a constant and high rate of heat to help ensure a security of supply. Therefore this form of energy is fit as a base for sustainable energy production (Geothermie & DAGO, 2021).

In The Netherlands targets for geothermal energy production are deep sedimentary porous aquifers (C. Willems, Nick, Goense, & Bruhn, 2017). In most Dutch geothermal projects the fluid propagates through the rock matrix and in a few cases through fault and fracture permeability. The heat is extracted from the subsurface through doublet systems (Moeck, 2014). Warm water is produced from the subsurface and once at the surface the heat is extracted. Then the cooled water is re-injected back into the aquifer. (H. F. Mijnlieff, 2020) A schematic is shown in Figure 1.1.

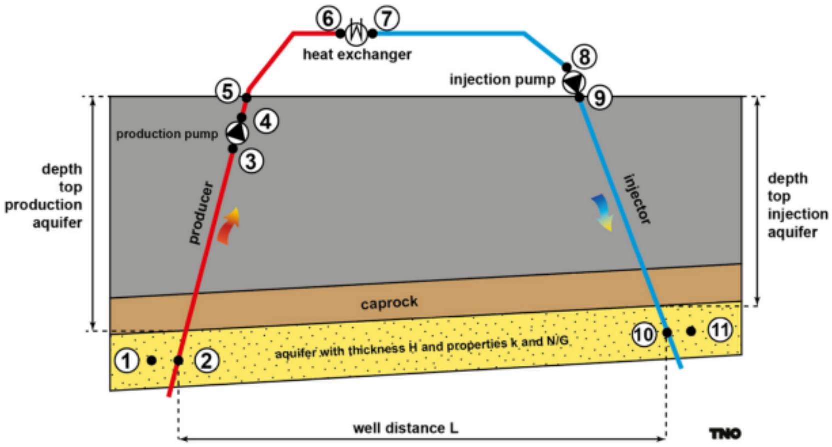

Figure 1.1: Schematic of a geothermal doublet (H. Mijnlieff et al., 2014)

Geothermal potential is dependent on a combination of a high enough temperature and a well enough transmissivity. In general a deeper aquifer results in a higher temperature. However, as transmissivity is correlated to both aquifer thickness and permeability, a deeper burial will generally result in less favourable permeability and thus by extent transmissivity. (H. F. Mijnlieff, 2020) (Pluymaekers et al., 2012) The regions with the highest potential for geothermal energy are the West Netherlands Basin (WNB) and at the edges of the Texel-Ijsselmeer High (TYH). The main targets in the WNB are the Upper Jurassic-Lower Cretaceous Nieuwerkerk Formation and the Vlieland Group. Geothermal projects in the TYH aim at the Rotliegend Slochteren Formation. The promising conditions are clearly visible from the doublet placement in Figure 1.2 (H. F. Mijnlieff, 2020)

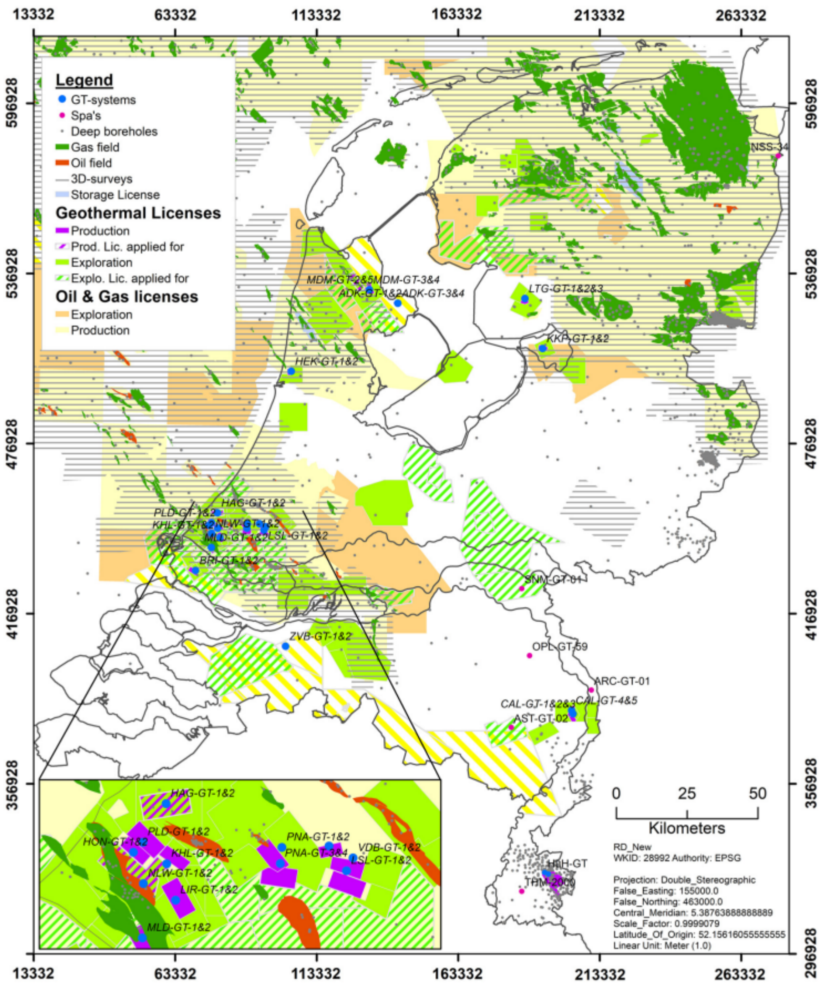

Figure 1.2: Locations of geothermal projects in The Netherlands (H. F. Mijnlieff, 2020)

Within the targeted reservoirs the presence of faults introduce a potential issue related to the production of geothermal energy: induced seismicity, which is an arising concern regarding geothermal energy as an energy source (L. Buijze, van Bijsterveldt, et al., 2019) (Evans, Zappone, Kraft, Deichmann, & Moia, 2012) (Foulger, Wilson, Gluyas, Julian, & Davies, 2018). This risk negatively influences the further development of geothermal energy (Zang et al., 2023). Seismicity is not something new in The Netherlands, where both natural and induced earthquakes have been measured. The majority of the naturally occurring, tectonic seismic events are located in the South-Eastern part of The Netherlands, in the Roer Valley Graben and most measured induced cases are related, although not limited, to the gas extractions in the Groningen gas field. (A. G. Muntendam-Bos et al., 2022) Induced events have also been linked to salt solution mining, gas storage and post-mining water ingress (A. G. Muntendam-Bos et al., 2022) (Ruigrok, Spetzler, Dost, & Evers, 2019). A study by Buijze et al. (2019) showed that possible induced events as a result of geothermal energy production in shallow porous sandstone reservoirs are not likely to surpass a magnitude of 2.0 and will therefore not be felt (L. Buijze, van Bijsterveldt, et al., 2019). However, thermal effects can be significant in fault stability, especially on the long term as the cold front grows over time (Hutka, Cacace, Hofmann, Mathur, & Zang, 2023) (Parisio, Vilarrasa, Wang, Kolditz, & Nagel, 2019) (Kivi, Pujades, Rutqvist, & Vilarrasa, 2022) (L. Buijze, Veldkamp, & Wassing, 2023) (Wassing et al., 2021). Moreover the significance of fault offset, which promotes the onset of fault reactivation in depleting gas fields, has been proved important in several studies (Van den Bogert, 2015) (Van Wees et al., 2017) (L. Buijze, Van Den Bogert, Wassing, Orlic, & Ten Veen, 2017) (L. Buijze, Van den Bogert, Wassing, & Orlic, 2019) (Mulders, 2003). Therefore it is important to improve the understanding of geomechanical processes due to geothermal operations. The focus of this study is the effect of juxtaposition of sandstone and claystone formations across faults on thermo-elastic stress changes and induced fault slip in geothermal projects.

Problem statement

In research done within the KEM-15 program, results showed that fault properties such mineral composition, fault roughness and frictional properties of faults play a key role in injection-induced seimicity (Hofmann et al., 2024). However, the effect of juxtaposition of different formations with different hydraulic and frictional properties across a fault is often not taken into account or modelled. However in the case of gas extraction several studies have already shown that fault offset promotes fault reactivation as stress tends to concentrate on the fault (L. Buijze, Van den Bogert, et al., 2019) (Mulders, 2003) (Orlic & Wassing, 2013) (L. Buijze, Fokker, & Wassing, 2021) (Jansen, Singhal, & Vossepoel, 2019) (Van den Bogert, 2015). The effect of fault throw can even exceed the effect of poro-elastic parameters (L. Buijze et al., 2021). The effect of fault offset on stress changes and fault slip in geothermal projects is therefore an important topic to investigate.

A tool that is currently used to assess seismic hazard and seismic risk in geothermal projects in The Netherlands is SRIMA (Seal and Reservoir Integrity through Mechanical Analysis). This is a semi-analytical tool is used in the Standard extended Seismic Hazard Analysis (Fokker, Buijze, & Pluymaekers, 2023) (H. Mijnlieff, de Vries, Jaarsma, & Vogelaar, 2023). SRIMA can assess stress changes and fault slip due to temperature and pressure changes. The reservoir is assumed to be radially symmetric and can incorporate a gradual temperature and pressure change distribution over the reservoir. However, this tool cannot include fault offset. Another tool, DIANA, can be used for a similar purpose as SRIMA and is able to model fault offset as well as more complex, realistic reservoir geometries. The downside is that the higher complexity makes DIANA computationally expensive, resulting in long runtimes.

In order to incorporate fault offset without the need for long runtimes, the tool "PANTHER" will be used. Similarly to SRIMA it is semi-analytical and it can take into account the effect of fault offset, like DIANA. It is a 2D plane-strain model that assumes the reservoir to consist of two rectangular reservoir compartments divided by a fault which can have a certain dip angle and offset. (Fokker et al., 2023) (L. Buijze et al., 2021)

Research objective

The main question to be answered in this study is:

- **How does the juxtaposition of sandstone and claystone formations across faults affect thermo-elastic stress changes and induced fault slip in geothermal projects targeting porous sandstone reservoirs?**

The sub-questions formulated to help steer towards the main research question are:

- What are key factors for induced seismicity according to other studies?

- How do the results from the sensitivity analysis compare to the results from other research?

- What do the final results of this research imply for existing models?

Approach

In this study a base case model will be made to assess the effect of juxtaposition of sandstone and claystone formations across a fault on temperature and stress changes. The geothermal site of Pijnacker Geothermie will be used as an example for geological and geomechanical properties. This site is located within the West Netherlands Basin and the targeted reservoir rock is the Delft Sandstone Member. The data for the input of geological and geomechanical properties of the model will be taken from literature, site specific research and the "winningsplan". The base case will be constructed in PANTHER. To answer the main research question three scenarios will be constructed: (1) a fully juxtaposed sandstone-to-sandstone scenario without fault offset, (2) fully juxtaposed sandstone-to-claystone scenario and (3) partially juxtaposed sandstone-to-claystone scenario with half-reservoir-thickness offset. A sensitivity analysis will be performed based on the base case using parameter ranges based on literature. The goal is to determine the parameters with the most significant effect on stress changes and fault slip. The effect will be explored further by using three different metrics: maximum slip, total slip and temperature change at which reactivation first occurs. The effect of heterogeneous friction will also be addressed.

Thesis structure

The structure of this master thesis is as following:

- Chapter 1: Introduction of the topic, the problem and the research questions
- Chapter 2: Describes the geological background
- Chapter 3: Explains the important basic concepts of fault reactivation
- Chapter 4: Introduces the case study used in this thesis
- Chapter 5: Explains the methods used in this study
- Chapter 6, 7, 8 & 9: Discuss the results of the base case, sensitivity analysis, the metrics and the inclusion of heterogeneous friction
- Chapter 10: Contains the discussion
- Chapter 11: Concludes the findings of this thesis and gives recommendations

2

Geological setting

This section will provide background information on the geological basin and targeted reservoir rock this research is focused on. The geological history of the West Netherlands Basin will be described as well as the Nieuwerkerk Formation.

2.1. Geology of the West Netherlands Basin

The West Netherlands Basin is located in the South-West of the Netherlands, as indicated in Figure 2.1 and originates from the period between the Late Jurassic and the Late Cretaceous when it opened as a result of NW-SE oriented rift basins (Ziegler, 1990). During the Hauterivian the active faulting came to a halt and entered a post-rift phase. The basin subsided and the environment shifted to a marine setting. The subsidence continued until the Late Cretaceous, when the area went through a compressional phase. This compressional phase lead to inversion and uplift of the West Netherlands Basin. The pre-existing normal faults from the rifting period were reactivated into reverse faults. (Den Hartog Jager, 1996) The infill can be subdivided into three groups, fluvial clastics, marine clastics and pelagic carbonates (Den Hartog Jager, 1996). The fluvial sediments were deposited during the rifting phase which opened the basin. As the depositional environment became more marine, the marine clastic and later the pelagic carbonated were deposited. (Den Hartog Jager, 1996)

The WNB is built from several formations as shown in Figure 2.2. The base is the Triassic Upper Germanic Group, followed by the Jurassic Altena Group (purple and dark blue, 7 & 8) which contains the oil prone source rock Posidonia Shale. The Posidonia Shale is the source of oil fields in the WNB, as well as the Broad Fourteens and the Vlieland Basin (Racero-Baena & Drake, 1996). The main rock type forming the Altena Group is shallow-marine clays but also contains some carbonates and sandstones (Weert et al., 2024). The Schieland Group (light blue, 5) covers the Altena Group and consists of the Nieuwerkerk Formation, meaning that the Delft Sandstone Member is included. This Group originates from the period between the Late Jurassic and the Early Cretaceous. (Weert et al., 2024) This Group is followed by the transgressional clastic sediments from the Cretaceous Rijnland Group (dark green, 4). On top of this the Chalk Group (light green, 3) from the Late Cretaceous was deposited. This was during the time when the main inversion of the WNB took place. A schematic overview of a SW-NE oriented cross section and a NW-SE oriented cross section are shown in Figure 2.2 and Figure 2.3. The legend to the colours are indicated in the last column of Figure 2.4.

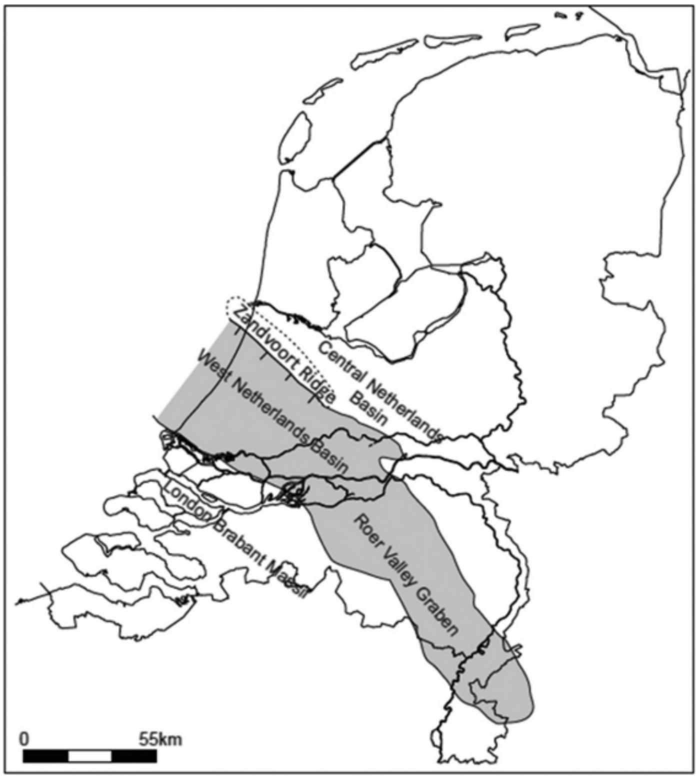

Figure 2.1: Location of the West Netherlands Basin (WNB) (C. J. Willems et al., 2020)

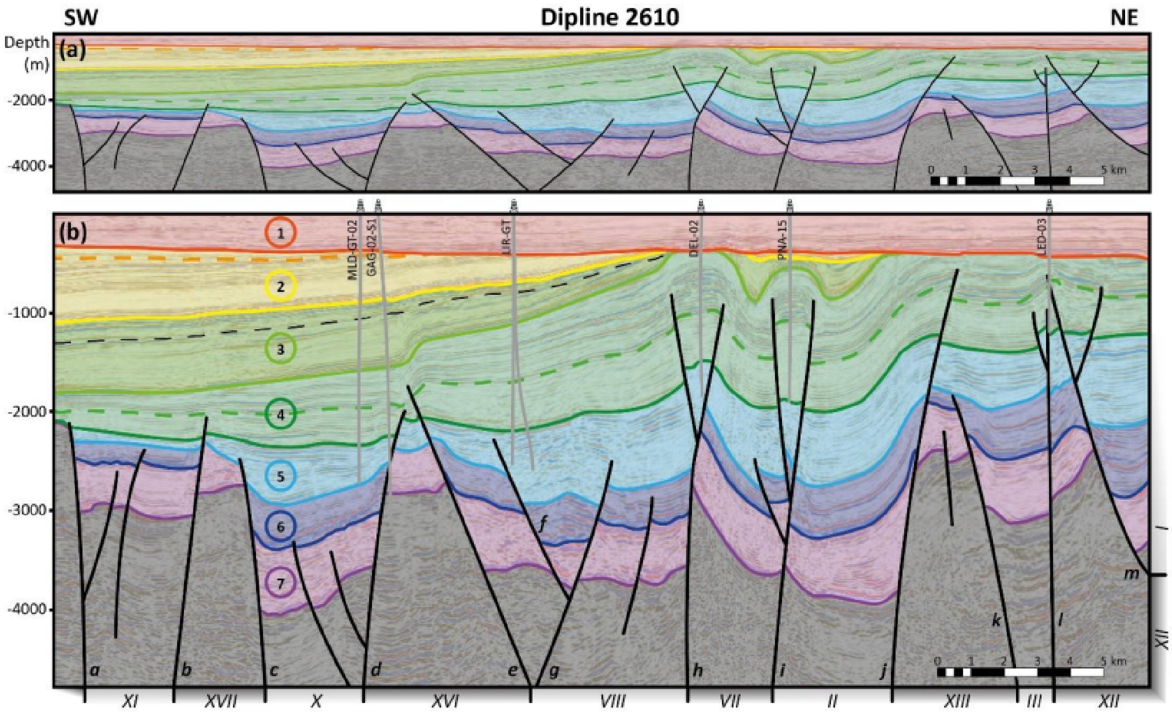

Figure 2.2: Seismic section and interpretation of the dipline 2610 through the WNB (Weert et al., 2024)

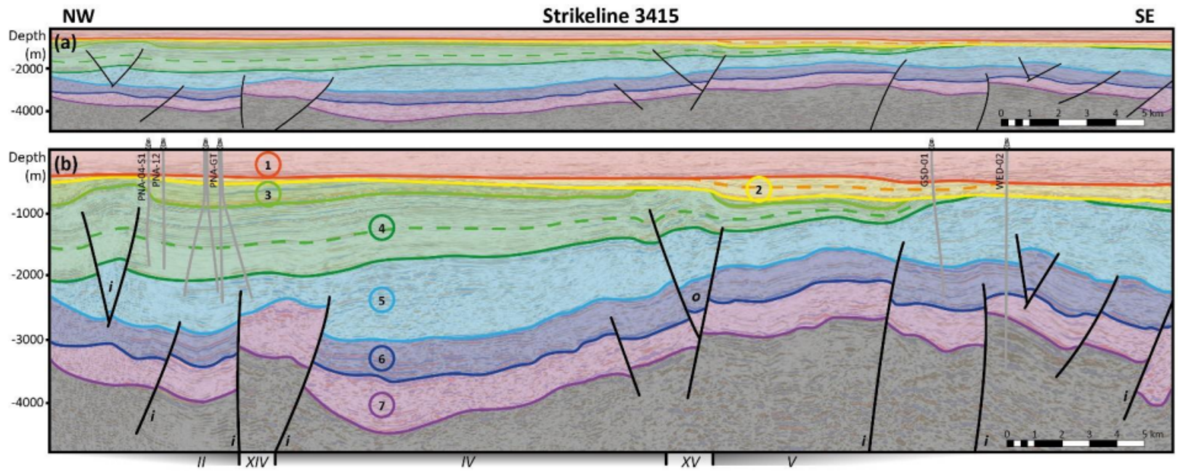

Figure 2.3: Seismic section and interpretation of strikeline 3415 through the WNB (Weert et al., 2024)

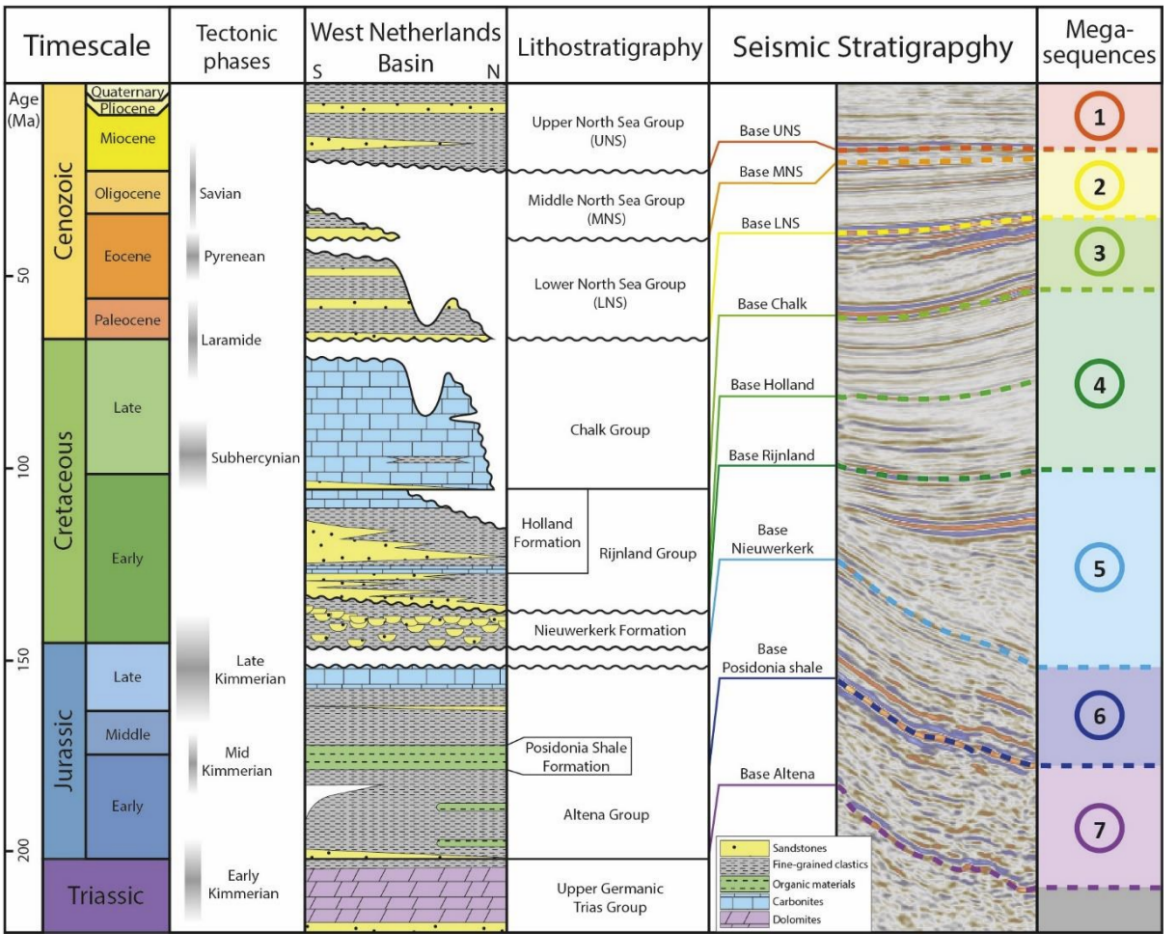

Figure 2.4: Stratigraphy West Netherlands Basin with legend of the colours in the seismic sections (Weert et al., 2024)

2.2. Nieuwerkerk Formation

The Nieuwerkerk Formation is indicated by the light blue colour, or number 5, in Figures 2.2 and 2.3. It overlays the Posidonia oil prone source rock (purple, 6) and is overlain by the Rijnland Group (dark green, 4). The Nieuwerkerk Formation originated from the Early Cretaceous and was deposited while rifting was active in the WNB in a fluvial environment. It can reach a thickness of 1km at certain locations (DeVault & Jeremiah, 2002) The formation includes three Members: the Alblasserdam Member at the base, followed by the Delft Sandtstone Member and the Rodenrijs Claystone Member at the top (Van Adrichem Boogaert & Kouwe, 1993). Their ages and an indication of their lateral variability can be seen in Figure 2.5.

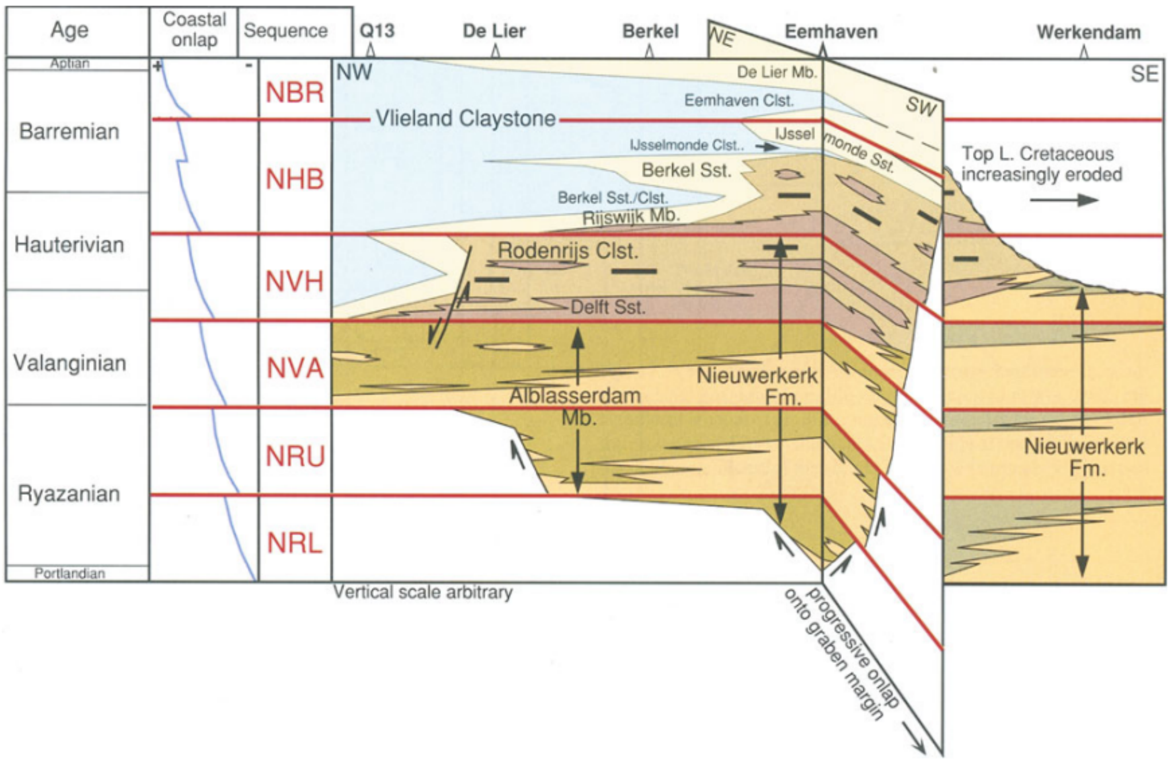

Figure 2.5: Lateral variability Nieuwerkerk Formation and its Members

2.3. Alblasserdam Member

The Alblasserdam Member forms the base of the Nieuwerkerk Formation and overlays the Altena Group (DeVault & Jeremiah, 2002). Well logs indicate this Member contains loosely stacked sandstone bodies deposited by meandering rivers. The remaining part is made up from fluvial-plain clay- and siltstone (Donselaar, Groenenberg, & Gilding, 2015). Lateral continuity is low and thus connectivity as well, giving the Alblasserdam Member a lower geothermal potential than the overlying Delft Sandstone Member, even though being warmer (C. J. Willems et al., 2020). The thickness of this Member lies between 100m to 1300m, as a result of syn-tectonic sedimentation (Vondrak, Donselaar, & Munsterman, 2018).

2.4. Delft Sandstone Member

The sand-rich part of the Nieuwerkerk Formation is the Delft Sandstone Member (Den Hartog Jager, 1996) (Van Adrichem Boogaert & Kouwe, 1993). It can be subdivided into three units based on the net-to-gross ratios according to (Donselaar et al., 2015). The first unit has a high N/G ratio of 30 to 60% and was deposited in an environment with meandering rivers and little accommodation space. The results are amalgamated, stacked multi-storey sandbodies with high vertical as well as lateral continuity. Some mudstones are present in between the sandbodies. (Donselaar et al., 2015) (Vondrak et al., 2018) The second unit has a low net-to-gross ratio of less than 15%. This unit originates from a time with a high rate of accommodation space, as shown by the individual sandstone beds surrounded by claystones and siltstones which were deposited in floodplains. Coal layers can also be found in this unit. The third unit has a medium net-to-gross ratio of approximately 15 to 30 %. It was deposited in a similar environment as the second unit, although with less accommodation space. (Donselaar et al., 2015)

However, this above described sedimentary architecture does not extend over the whole region. A shift in the sandstone rich depocentre from west during Late Ryanzanian to east during the Early Valanginian was explained by Willems et al. (2017) (C. J. Willems, Vondrak, Munsterman, Donselaar, & Mijnlieff, 2017). The Valanginian deposits are traditionally attributed to the Delft Sandstone Member but some have attributed units with amalgamated sandstone bodies of the Late Ryanzanian age to the Delft Sandstone Member instead of the Alblasserdam Member. Some others are convinced the multi-storey sandstone bodies can occur throughout the Nieuwerkerk Formation and therefore opening the possibility that the Alblasserdam Member could be a geothermal target (Jeremiah, Duxbury, & Rawson, 2010) (DeVault & Jeremiah, 2002).

The source river flowed from south-east to north-west, which is consistent with a decease in net-to-gross ratio moving along this axis (Racero-Baena & Drake, 1996) The river type changed from more braided type at the bottom of the Delfland Group towards a more meandering type towards the top. (Racero-Baena & Drake, 1996) This was caused by a change in tectonic activity and paleo-climate. The bottom part of the Delft Sandstone Member was deposited in times of active rifting and the upper part in times of subsidence, leading to the decrease in accommodation space. Moreover, the climate became more humid and more vegetation was present, changing the river type from braided to meandering with a increased degree of lateral migration. (Racero-Baena & Drake, 1996) (C. J. Willems et al., 2017)

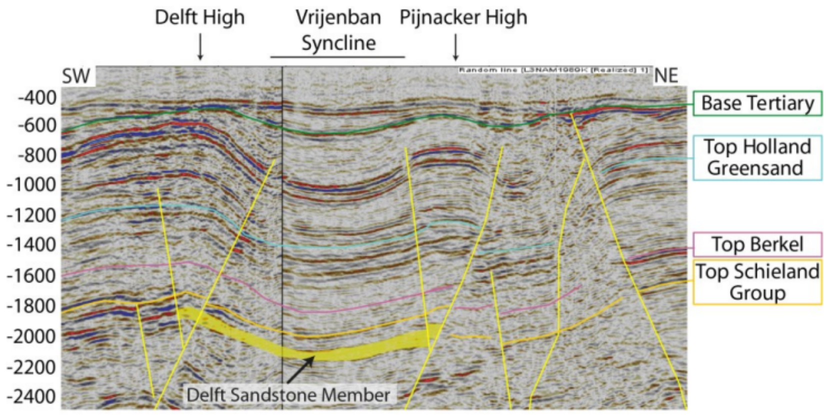

Figure 2.6: Seismic section of the WNB with the Delft Sandstone Member indicated (Donselaar et al., 2015)

2.5. Rodenrijs Claystone Member

The Delft Sandstone Member transitions into the overlaying claystone Rodenrijs Member by becoming increasingly more clay-rich. The depositional environment shifted from a lower delta with floodplains and marches, lakes and rivers to a more marine or lagoonal environment. Locally the Rodenrijs Claystone Member contains marine sandstone facies. (Den Hartog Jager, 1996)

3

Geomechanical background

This chapter will start from the basic concepts, explain the general concept of fault reactivation through the Mohr-Coulomb failure criterion, go into thermo-poroelasticity and talk about the difference between depletion and cooling induced fault reactivation. Lastly operational and geological parameters influencing fault reactivation and the effect of fault throw will be discussed at the end of this chapter.

3.1. General concept of fault reactivation

The state of stress in the subsurface can be described through three principle stresses. Notation-wise the largest stress is indicated as σ_1, the smallest stress as σ_3 and the one in between as σ_2. Their relative magnitudes formulate the stress regime, in The Netherlands the vertical stress σ_V is represented as σ_1 and the horizontal stresses σ_{Hmax} and σ_{Hmin} as σ_2 and σ_3. This means the tectonic stress regime in The Netherlands corresponds to a normal faulting regime, according to the Anderson's fault theory (Anderson, 1905) (Zoback, 2010)

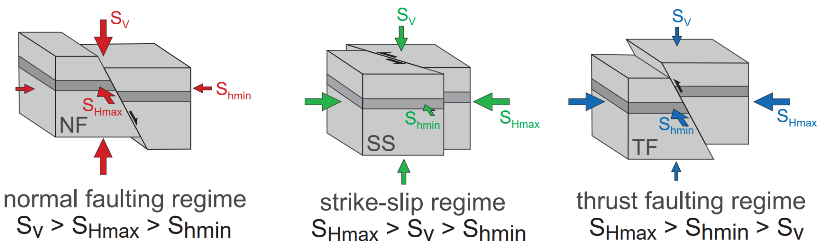

Figure 3.1: The three different tress regimes based on their relative magnitudes (Heidbach et al., 2016)

The controlling factor for rock behaviour is the effective stress, which can be calculated by subtracting the pore pressure from the normal stress as shown in Equation 3.1.

$$\sigma' = \sigma - \alpha P_p \tag{3.1}$$

where σ' is the effective stress, σ the normal stress, P_p the pore pressure and α the Biot's coefficient (Terzagi, 1923). The Biot's coefficient is a measure of the relative contribution of the effective stress which is put on the fluid relative to the effective stress put on the matrix of the porous rock. The effective vertical stress σ'_v can be calculated through (Jaeger, Cook, & Zimmerman, 2009):

$$\sigma'_v = \int_z^0 \rho(z) g dz \tag{3.2}$$

in which ρ is the density of the overburden, g gravity and z the depth. The effective horizontal stresses are often assumed to be equal and can be determined through:

$$\sigma'_H = \sigma'_h = \frac{\nu}{1-\nu}\sigma'_v \tag{3.3}$$

in which ν is the Poisson's ratio.

When the principle stresses act on a failure plane in the subsurface they can be used to formulate the normal stress σ_n and shear stress τ acting perpendicular on and along the plane as follows:

$$\sigma'_n = 0.5(\sigma'_1 + \sigma'_3) + 0.5(\sigma'_1 - \sigma'_3)cos2\delta \tag{3.4}$$

$$\tau = 0.5(\sigma'_1 - \sigma'_3)sin2\delta \tag{3.5}$$

where σ_1 is the maximum principle stress, σ_3 the minimal principle stress and δ the angle between σ_3 and the plane.

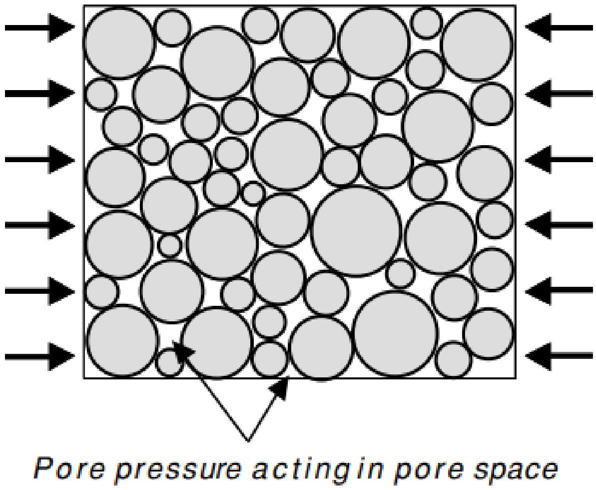

Figure 3.2: Pore pressure acting on the grains of the matrix (Zoback, 2010)

Fault planes are subjected to Mohr-Coulomb criterion for shear failure, formulated as (Jaeger et al., 2009):

$$\tau_{max} = C + \sigma'_n tan(\phi) \tag{3.6}$$

where c is the cohesion and ϕ is the angle of internal friction. $tan(\phi)$ can also be noted as f_s, the static friction coefficient. A point of the fault will start to slip when the shear stress at this point reaches its shear strength τ_{max}.

This state of stress can be depicted graphically through the Mohr-Coulomb circle as seen in Figure 3.3. Changes in horizontal, vertical, normal effective and shear stresses can be visualized though shifting and size changes of the circle(s). The failure criterion is depicted as the line, under an angle determined by the internal friction angle and offset by cohesion. The displacement from the original location on the Mohr-Coulomb circle to a new position is called a "stress path". Failure can occur if either the Mohr-Coulomb circle enlarges, indicating an increased differential stress ($\sigma'_1 - \sigma'_3$) or if the circle moves to the left, indicating a decrease in mean stress.

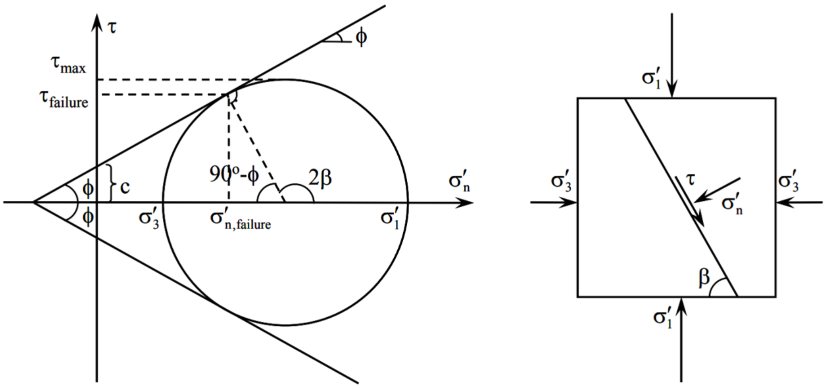

Figure 3.3: Mohr-Coulomb circle and failure criterion (Mulders, 2003)

There are a number of metrics used to evaluate the proximity to failure of a fault plane. One way to measure this is through the Shear Capacity Utilization (SCU). This is a ratio of the actual shear stress τ at a point divided by the shear strength of the fault (maximum shear stress the fault can sustain before failing τ_{max}). If τ reaches τ_{max}, the SCU is equal to 1 and therefore means the fault plane fails.

$$SCU = \frac{\tau}{\tau_{max}} = |\frac{\tau}{C + f_s \sigma'_n}| \tag{3.7}$$

where τ is the shear stress acting on a plane, τ_{max} the maximum shear stress the plane can sustain, C is the cohesion and f_s is the friction coefficient.

Elastic moduli

How a rock responds to these stresses is dependent on their elastic moduli. The most important elastic moduli discussed in this thesis are the Young's modulus, the Poisson's ratio and shear modulus. The Young's modulus shows how a material resists to compression, it represents the rock's stiffness. The Poisson's ratio is a measure of deformation laterally when loaded vertically and the shear modulus is a ratio between the applied shear stress to the shear strain and is a measure of rigidity (Zoback, 2010)

3.2. Thermo-poroelasticity

Depletion and cooling of a reservoir rock can both result in fault failure, although the mechanism is slightly different. In the case of depletion the gas extraction leads to a reduction in reservoir pressure. If linear poro-elasticity is assumed the reservoir will contract due to the pressure drop and subsequent negative strain (Geertsma, 1973). In the vertical direction the resulting volume change translates to compaction as the surface acts as a free surface and the overburden remains unchanged. In the lateral direction however the reservoir rock is connected to the surrounding rock. When a part of a reservoir wants to deform due to pressure and/or temperature changes but is hindered by the surrounding rock, anisotropic changes in total stress might be induced. (Soltanzadeh & Hawkes, 2008)

A ratio of the change in total stress to the change in pore pressure within the reservoir can be quantified through stress arching ratio (Soltanzadeh & Hawkes, 2009) (Mulders, 2003) (Segall & Fitzgerald, 1998). These ratios can provide an indication of the stability of the fault. Stress arching ratios can be applied on poro-thermoelasic materials, with a linear relationship between stress change and pore pressure in the poroelastic case and temperature in the thermoelastic case. The poro-elastic ratios are denoted as

$$\gamma_{\alpha(H_1)} = \frac{\Delta\sigma_{H_1}}{\alpha\Delta P}, \gamma_{\alpha(H_2)} = \frac{\Delta\sigma_{H_2}}{\alpha\Delta P}, \gamma_{\alpha(V)} = \frac{\Delta\sigma_V}{\alpha\Delta P}, \tag{3.8}$$

the γ being the poroelastic normalized horizontal and vertical stress arching ratios, $\Delta\sigma$ the horizontal and vertical stress changes and ΔP the reservoir pore pressure change. (Soltanzadeh & Hawkes, 2008)

The degree to which these stress changes occur are dependent on elastic rock properties, reservoir geometry and contrast in elastic properties between reservoir rock and surrounding rock. For simple reservoir geometries poro- and thermoelastic stress changes can be calculated analytically (Geertsma, 1973) (Segall, 1989) (Segall, Grasso, & Mossop, 1994).

As mentioned above in the vertical direction the compaction caused by the pore pressure reduction translates to compaction. If a reservoir is laterally extensive reservoir, deformation is assumed to be uniaxial. This means that the total vertical stress change $\Delta\sigma_v$ will be minimal and can be assumed to be zero (Soltanzadeh & Hawkes, 2008) (Soltanzadeh & Hawkes, 2009) (Segall et al., 1994). The horizontal stress change can be determined through the following three relations which hold according to the theory of poroelasticity in combination with Equation 3.3.

$$\Delta\sigma_v = \Delta\sigma'_v + \alpha\Delta P \tag{3.9}$$

$$\Delta\sigma_H = \Delta\sigma'_H + \alpha\Delta P \tag{3.10}$$

$$\Delta\sigma_h = \Delta\sigma'_h + \alpha\Delta P \tag{3.11}$$

If the total vertical stress change $\Delta\sigma_v$ is assumed to be equal to zero then the vertical effective stress change $\Delta\sigma'_v$ can be denoted as:

$$\Delta\sigma'_v = -\alpha\Delta P \tag{3.12}$$

And the notation for the effective horizontal stress can be based on the stress arching ratios and Equation 3.11:

$$\Delta\sigma'_h = \gamma_h\alpha\Delta P - \alpha\Delta P = -(1-\gamma_h)\alpha\Delta P \tag{3.13}$$

Using this formulation in combination with the relation between σ'_v and σ'_h (Equation 3.3) and Equation 3.11 results in the following formulation of the horizontal stress change:

$$\Delta\sigma_h = (\frac{1-2\nu}{1-\nu})\alpha\Delta P \tag{3.14}$$

Inserting the formulations of the total vertical and horizontal stress changes into Equation 3.8 gives the form of the stress arching ratios for a laterally extensive reservoir:

$$\gamma_{\alpha(H_1)} = \gamma_{\alpha(H_2)} = \frac{1-2\nu}{1-\nu}, \gamma_{\alpha(V)} = 0 \tag{3.15}$$

These formulations show that for a certain Biot's coefficient and Poisson's ratio, the vertical effective stress change will be larger than the horizontal effective stress change. The differential stress will therefore increase. Translating this to the Mohr-Coulomb circle this would be visualized by a growing circle moving to the right along the x-axis. The stress path is towards the top right, as depicted in Figure 3.4.

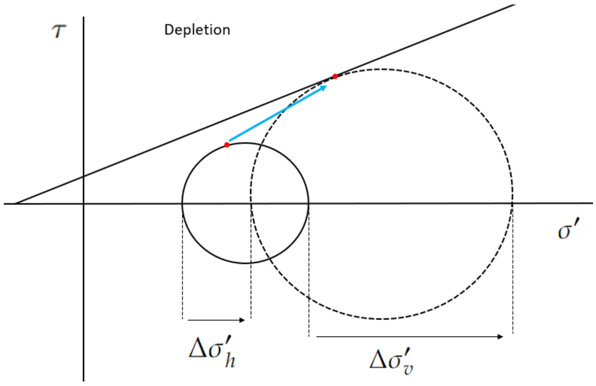

Figure 3.4: Stress path in case of depletion

In case of cold water injection thermo-elastic stresses are introduced. In reality then both poro-elastic and thermo-elastic stresses will act in the reservoir and on the fault plane. This thesis focuses solely on the temperature induced stress changes and therefore assumes drained conditions.

The cold injected water cools the hot reservoir rock. This cooling makes the rock want to shrink. Similarly to the depletion case the tendency of the rock to shrink can be accommodated in the vertical direction as there is no change in the overburden and the surface acts as a free surface. In the horizontal direction the rock is attached to surrounding rock, leading to horizontal stress changes. Similar to the poro-elastic stress arching ratios there exist thermo-elastic stress arching ratios:

$$\gamma_{T(H_1)} = \frac{\Delta\sigma_{H_1}}{\eta\Delta T}, \gamma_{T(H_2)} = \frac{\Delta\sigma_{H_2}}{\eta\Delta T}, \gamma_{T(V)} = \frac{\Delta\sigma_V}{\eta\Delta T} \tag{3.16}$$

where η is the linear thermal expansion coefficient and ΔT the change in temperature. Poro-elastic stress arching ratios can be converted into thermo-elastic ones through the following relation (Soltanzadeh & Hawkes, 2009):

$$\gamma_{T(ij)} = \frac{2\mu(1+\nu)}{1-2\nu}\gamma_{\alpha(ij)} \tag{3.17}$$

Combining the thermo-elastic stress arching ratios (Equation 3.16), Equation 3.17 and the poro-elastic stress arching ratios for a laterally extensive reservoir as previously derived (3.15) results in:

$$\Delta\sigma_h = \eta\Delta T\frac{(1-2\nu)}{(1-\nu)}\frac{2\mu(1+\nu)}{(1-2\nu)} \tag{3.18}$$

Using that $E = 2\mu(1+v)$ leaves:

$$\Delta\sigma_h = \frac{E\eta\Delta T}{(1-\nu)} \tag{3.19}$$

As it is assumed there are no pore pressure changes the vertical effective stress changes are zero.

$$\Delta\sigma_h = \Delta\sigma'_h = \frac{E\eta\Delta T}{(1-\nu)}, \Delta\sigma_v = \Delta\sigma'_v = 0 \tag{3.20}$$

This translates to a larger Mohr-Coulomb circle as the effective horizontal stress will decrease while the vertical effective stress remains unchanged. The stress path is towards the top left, as depicted in Figure 3.5.

The thermo-elastic stress path parameter is indicative for the response of the horizontal stress changes. Exact calculations can be made by using the stress arching ratios corresponding to the (simple) reservoir geometry.

More information on the theory of inclusions and the different forms of stress arching ratios can be found in the work by Segall & Fitzgerald (1998) (Segall & Fitzgerald, 1998), Soltanzadeh (2008) (Soltanzadeh & Hawkes, 2008), Soltanzadeh & Hawkes (2009) (Soltanzadeh & Hawkes, 2009).

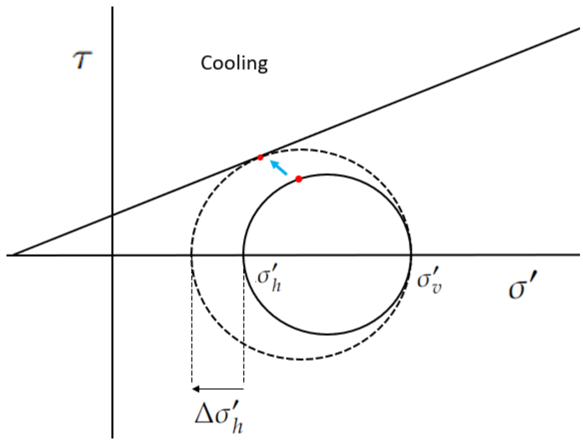

Figure 3.5: Stress path in case of cooling

Thermal effects mainly play an important role in the long term, as the cold front expands and cools down more of the surrounding rock (Hutka et al., 2023) (Parisio et al., 2019). In geothermal projects the thermoelastic effects can be significant and could have the potential to reactivate faults if they are situated within the cooled region (Segall & Fitzgerald, 1998) (L. Buijze et al., 2021). These effects are not contained within the reservoir but the cooling induced contraction and stress reduction affects the stress distribution outside of the reservoir. (De Simone, Vilarrasa, Carrera, Alcolea, & Meier, 2013) (Vilarrasa, Olivella, Carrera, & Rutqvist, 2014) (Parisio et al., 2019) (Jeanne et al., 2014)

3.3. Operational parameters

Work by Hutka et al. (2023) found that a reduction in injected volume of cold water did reduce the potential of an induced seismic event, however a link between magnitudes and injected volume has not been established (Hofmann et al., 2024). Larger temperature changes could result in larger thermal stresses, however only a weak correlation was found between the magnitude of the seismic event and the difference between reservoir and injection temperature. (Hofmann et al., 2024) (A. J. L. Buijze, 2020) (Hutka et al., 2023) Hincks et al. (2018) found that for deeper geothermal systems the risk of induced events increases, and work by Buijze et al. (2019) indicates a similar trend. In this work seismic events exceeding a magnitude of 2 were only induced in geothermal systems reaching a temperature difference of 100 °C or higher. (Hincks, Aspinall, Cooke, & Gernon, 2018) (L. Buijze, van Bijsterveldt, et al., 2019) The overall trend is the smaller the perturbations, the smaller the seismic risk, although the effect of operational parameters is highly dependent on local geological conditions, which might therefore be considered as more critical in assessing seismic risk (Hofmann et al., 2024).

3.4. Geological parameters affect fault reactivation

Among the important parameters influencing fault reactivation are size of the fault (Hofmann et al., 2024) and the initial tectonic stresses acting on the fault in question (L. Buijze, van Bijsterveldt, et al., 2019). Additionally the cohesion and friction of the fault, as well as the dip in combination with the faulting regime are of key importance (Hofmann et al., 2024) The poro-thermoelatic response of the rock is governed by its elastic moduli, of which the Young's modulus, Poisson's ratio and bulk modulus are found to be of importance (Mathur, Hofmann, Cacace, Hutka, & Zang, 2024) (Hutka et al., 2023) (Zang et al., 2023). In terms of thermal properties the thermal expansion coefficient is most significant (Mathur et al., 2024).

3.5. Effect of fault throw

In cases where cooled and depleted reservoirs contain a fault throw which offsets compartments, stress tends to concentrate. This increases the tendency of reactivation for normal faults. (L. Buijze et al., 2021) A similar conclusion was made by (Van den Bogert & van Eijs, 2020) and (L. Buijze et al., 2017) (L. Buijze, Van den Bogert, et al., 2019), where the minimum amount of depletion needed to reactivate the fault was at a reservoir-thickness fault offset. Thereafter the depletion pressure started to increase again. If a fault is located in a normal faulting regime, depletion will result in an increase of shear stress at the top of the hanging wall and the base of the footwall (Van den Bogert & van Eijs, 2020). The extent to which slip patches will overlap is caused by the degree of fault offset (Orlic & Wassing, 2013). Oppositely, at the bottom of the hanging wall and top of the footwall a reduction in shear stress will take place. The negative shear stress can prevent further fault slip propagation into the base and seal surrounding the affected reservoir (Van den Bogert & van Eijs, 2020) (L. Buijze et al., 2017) (Jansen et al., 2019).

3.6. Seismic and aseismic fault slip

When fault slip occurs it does not necessarily cause seismic activity. Whether a fault behaves seismic or aseismic after reactivation is determined by its mechanical stability, which depends on its frictional properties. Low-cohesive sandy formations and clay-rich fault gouges are less prone to seismic slip than for example granites (Hunfeld, Niemeijer, & Spiers, 2017). Although aseismic slip can transfer stress to rocks which are more prone to seismic slip (A. J. L. Buijze, 2020) (Eyre et al., 2019). The presence of clay in the fault gouge has been found to lubricate the fault, making it slip as a result of lower stress changes compared to coarser material, however with aseismic slip rather than seismic (Niemeijer & Spiers, 2005). Aseismic slip changes into seismic slip when a certain slip patch length has been reached due to increasing stress on the fault, the critical nucleation length (Uenishi & Rice, 2003).

4

Pijnacker Geothermie

In this thesis the geology of the Pijnacker Geothermie project (PNA-GT) is used as the basis for the geomechanical properties. The site is located within the West Netherlands Basin and targets the Delft Sandstone Member as the reservoir rock. The wells PNA-GT-05 and PNA-GT-06 were drilled in 2018 and are used for greenhouse heating. The yearly extracted heat is estimated to be 450000 GJ (*Winningsplan Ammerlaan Geothermie*, 2019). Located nearby these wells a pair of older, abandoned wells also exists, which are currently prepared to be used in the TKI DHARA project to monitor induced seismicity.

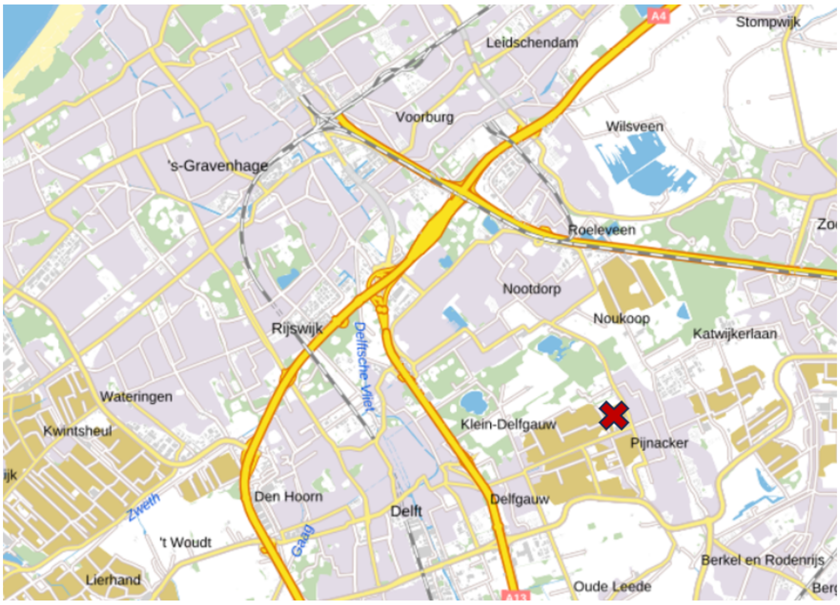

Figure 4.1: Location of the geothermal site

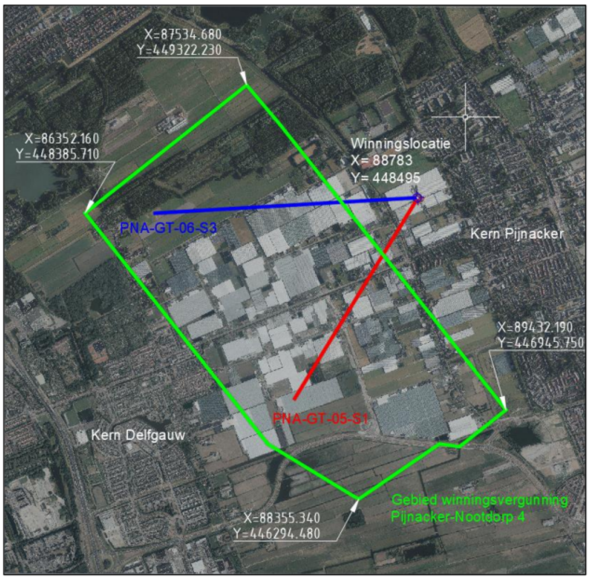

Figure 4.2: Geothermal license area and well trajectories (*Winningsplan Ammerlaan Geothermie*, 2019)

4.1. Local structural geology

A seismic section of the Pijnacker reservoir is shown in Figure 4.3, with the tops and bases of several formations and groups. The Pijnacker reservoir went through two phases which formed its structural geology. The first phase took place during the Early Cretaceous when a pull-apart basin was formed. A schematic of this process can be seen in Figure 4.4. Then, when the West Netherlands Basin went through a time of compression and inversion, the Pijnacker reservoir experienced the same forces. Normal faults were reactivated as reverse faults and the existing negative flower structure developed into a pop-up structure as a result of this compression. (Racero-Baena & Drake, 1996) A schematic of this second phase is depicted in Figure 4.5.

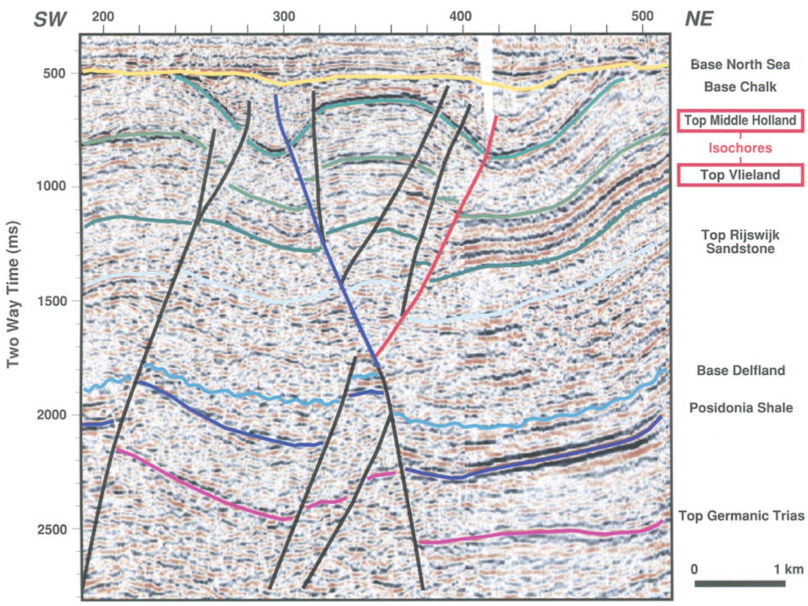

Figure 4.3: Seismic section of the Pijnacker field (Racero-Baena & Drake, 1996)

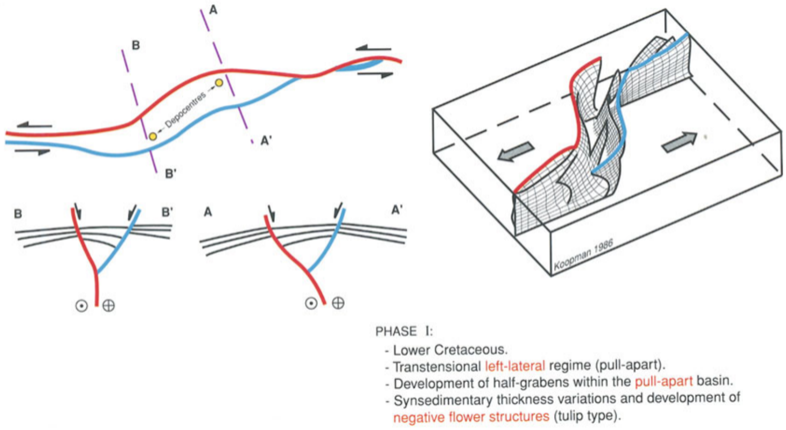

Figure 4.4: Phase I of structural evolution Pijnacker field in which a pull-apart basin developed (Racero-Baena & Drake, 1996)

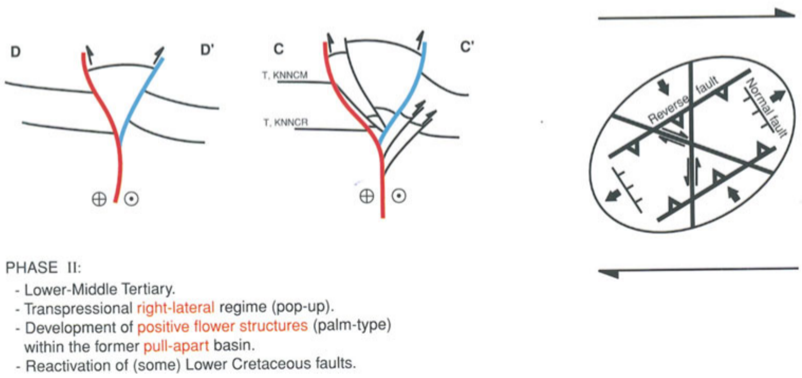

Figure 4.5: Phase II of structural evolution Pijnacker field in which reverse faulting occurred and pop-up structures formed as a result of compression (Racero-Baena & Drake, 1996)

4.2. Fault located within the reservoir

The reservoir is crossed by multiple faults, as shown in Figure 4.3. These fault are the key aspects of this research as they have the potential to be reactivated during geothermal projects. For the analysis to be performed in this thesis the most nearby fault will be used as this fault will have the highest reactivation potential. Figure 4.6 by PanTerra shows the top depth of the Delft Sandstone, the faults they interpreted to be near the injector, the injector location and the geothermal well trajectories (PNA-GT-05 and PNA-GT-06).

4.2.1. Distance to injector

There is some discrepancy between sources on the distance between the injector and the most nearby fault. PanTerra concluded that the distance is approximately 325m (PanTerra, 2023) while Stefan Peeters found it to be at 450m distance (Peeters, 2024), all assuming mid-depth. The main reason for the difference is that both sources interpreted a different fault to be closest to the injector. Figure 4.7 shows the fault interpretation done by PanTerra, the black curved line indicates the well trajectory of the PNA-GT-06 injector well and the yellow coloured fault is the nearest fault. Figure 4.8 shows the interpretation by Stefan with the white curved line indicating the well trajectory and the green line indicating the near by fault, in stead of the bright coloured fault above it, which is the chosen fault by PanTerra. The fault assumed to be the closest by PanTerra is an Upper Cretaceous transpressional fault, while the other fault is a normal fault originating from the Jurassic (Peeters, 2024).

4.2.2. Dip of the fault

As described above sources consider different faults and therefore the dip also shows discrepancy. PanTerra uses a dip of 75 degrees, while Stefan Peeters and AGE use 65 degrees. The dip angle of a fault is of great importance to and has a large effect on fault slip, therefore this difference is important for the analysis.

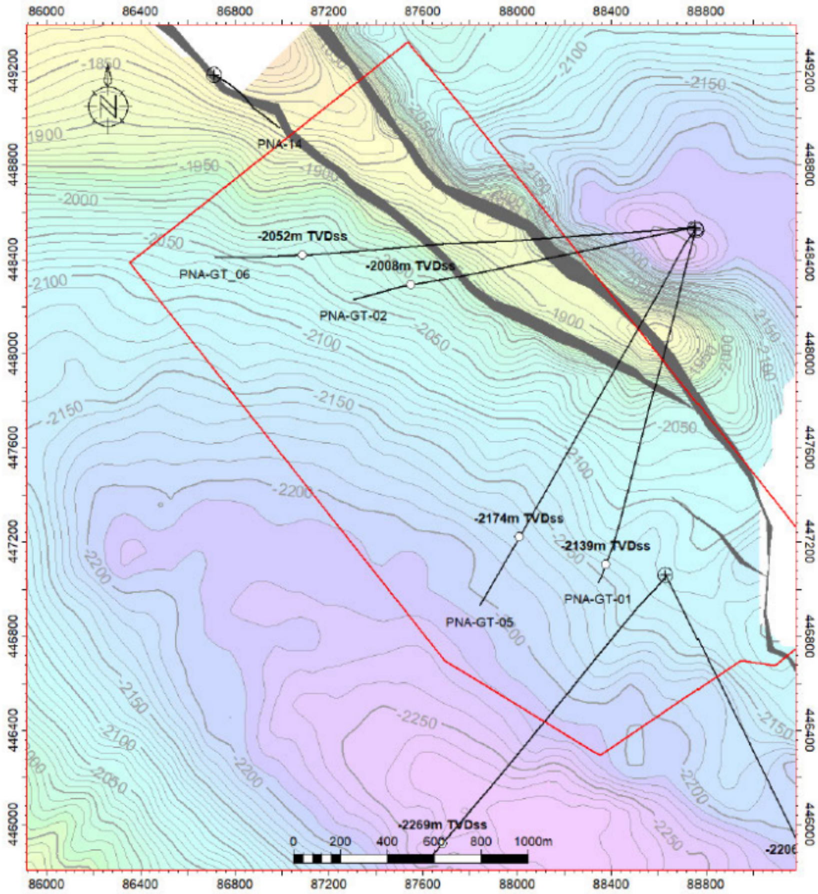

Figure 4.6: Top map Delft Sandstone with locations and trajectories of wells (PanTerra, 2023)

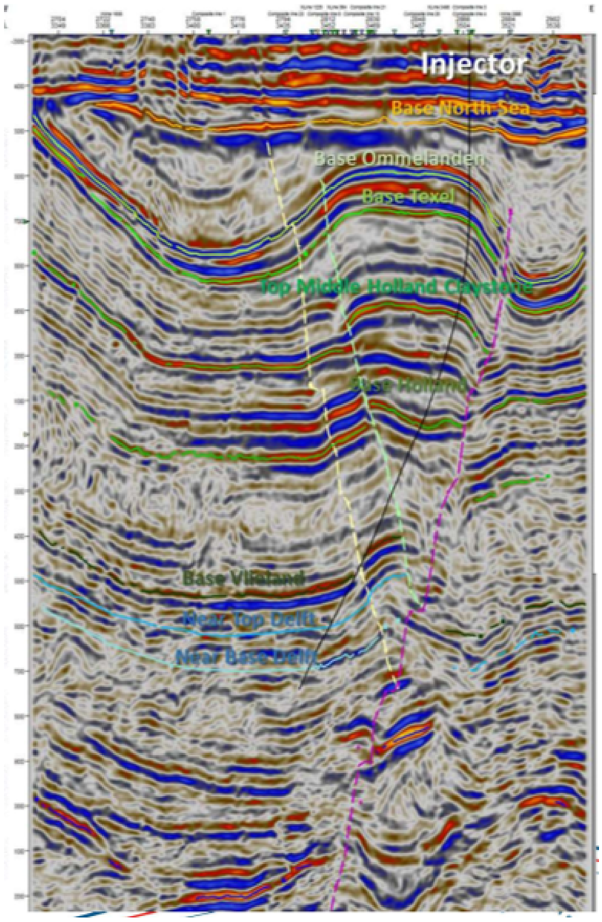

Figure 4.7: PNA fault interpretation by PanTerra (PanTerra, 2023)

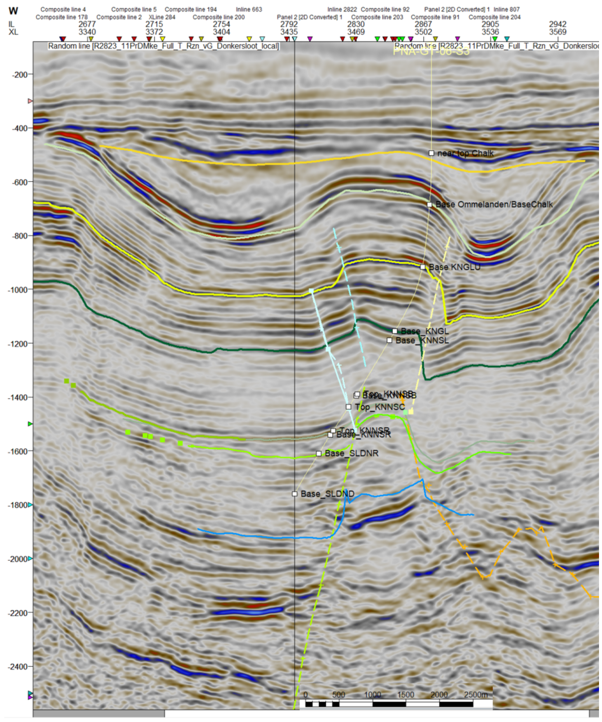

Figure 4.8: PNA well and fault in seismic section (Peeters, 2024)

4.3. Delft Sandstone and Ablasserdam Member

The approximate location of the Delft Sandstone is indicated in Figure 4.9. The thickness of the Delft Sandstone is different on each side of the fault, as the sediments were deposited while the normal fault was active, which created more accommodation space on the hanging wall side. This means that the sandstone is fully juxtaposed against the underlying Alblasserdam Member, which has an approximated net-to-gross ratio of 30%, while the net-to-gross ratio of the Delft Sandstone is estimated to be between 90 to 95 %. The Alblasserdam Member in the graben contains more sand than in the horst, as the preferential flow path of rivers was in the fastest subsiding areas. (Peeters, 2024)

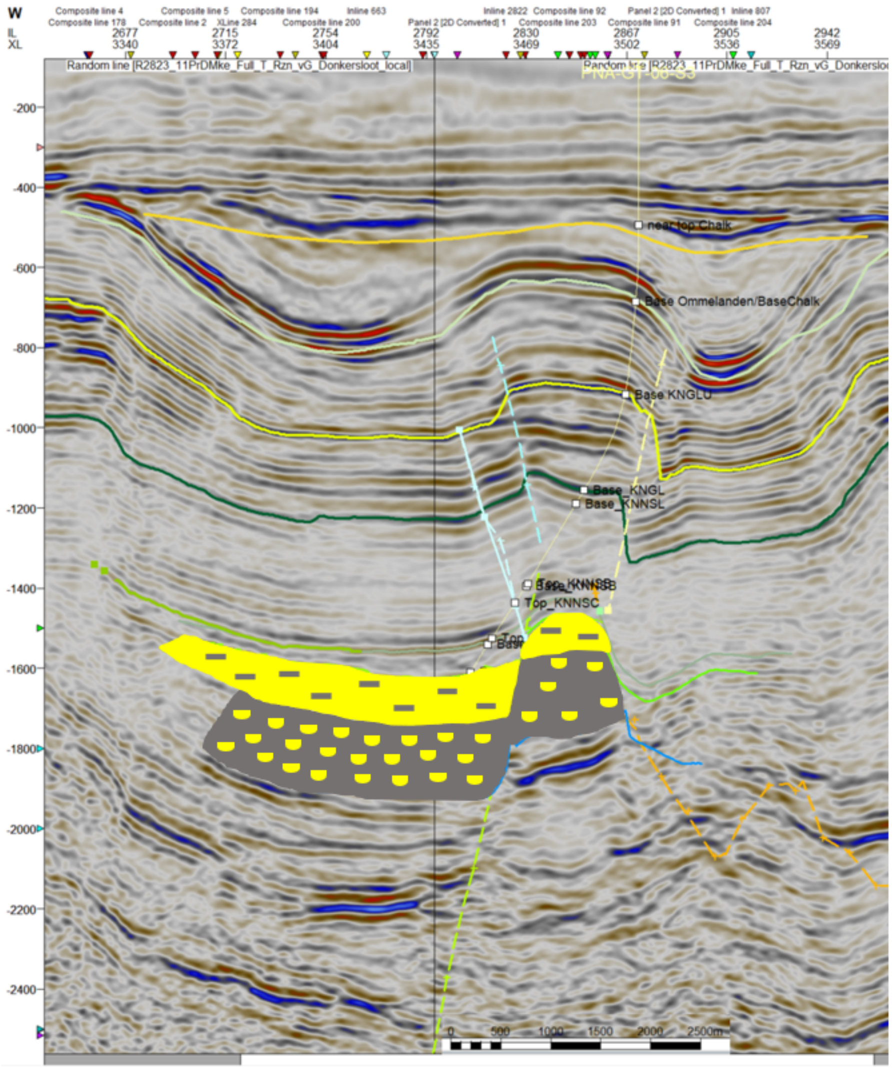

Figure 4.9: Approximate indication of Delft Sandstone and Alblasserdam

5
Methodology

This section will give information on the model and the assumptions there are made in terms of the modelled reservoir geometry and the pressure and temperature changes. Furthermore the validation of the model choices and reasoning behind the reservoir geometry are discussed. Lastly this chapter contains a table with the used variable input.

5.1. PANTHER

The "Physics-based semi-ANalytical Tool for Human-induced Earthquake Rupture", or "PANTHER", can be used to assess the stress changes on a fault due to temperature and pressure changes and the resulting fault slip. The model is a semi-analytical, 2D plane-strain model and uses simplified geometries as shown in the schematic in Figure 5.1 (L. Buijze & van der Heiden, 2024). A reservoir consists of two compartments divided by a fault which offsets the compartments. A uniform pressure and temperature distribution is assumed over the whole compartment, as well as vertical diffusion of pressure and temperature into the base and seal. The compartments can have different pressure and temperatures. The poro-thermoelastic stress behaviour is based on the closed-form solutions van Jansen, Singhal and Vossepoel (2019) (Jansen et al., 2019), but oppositely to their work Panther can include the effects of aseismic slip and diffusion. It can, however, not take into account a contrast in elastic properties between the reservoir and the base or seal. On the other hand Panther does consider fault offset, which is essential to this study. The model also contains a stochastic module useful for analysing key factors for fault reactivation. Panther can be applied as a first assessment of stress changes and fault slip. (L. Buijze & van der Heiden, 2024) (L. Buijze et al., 2021)

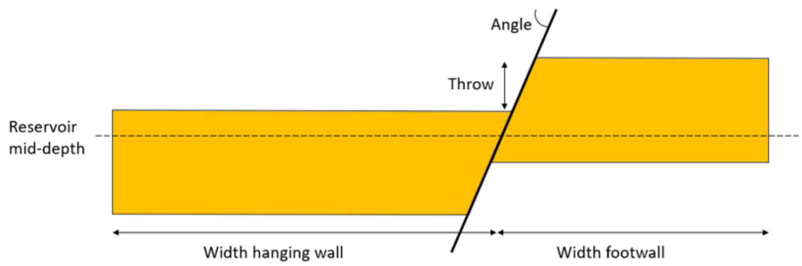

Figure 5.1: Reservoir geometry used in Panther

Geometry

The geometry of the reservoir is assumed to be rectangular in which the thickness and width can be adjusted. The width of the hanging wall and footwall, divided by a fault, can be changed independently from each other. Panther works with a reservoir mid-depth which, in case of an offset fault, is the middle of both compartments, as shown in Figure 5.1.

Behaviour medium and fault

Linear elasticity is assumed for both the reservoir and surrounding rock and the elastic moduli are taken to be uniform over the model. There is therefore no contrast in elastic properties between the reservoir and the surrounding rock in the model. The behaviour of the fault is subject to the Mohr Coulomb failure criterion (Equation 3.6). The cohesion, static and dynamic friction coefficient, dip angle, dip azimuth and throw can be assigned in Panther. There is an option to "switch on or off" aseismic slip, which would occur if the Shear Capacity Utilization (Equation 3.7) exceeds a value of 1.

Initial stress, temperature and pressure

The initial minimum and maximum stress are σ_h and σ_v. The vertical stress is given by the vertical stress gradient and the initial horizontal stress is a function of the initial vertical stress according to a stress ratio of K_0: $\sigma_h = K_0\sigma_v$. The initial pressure is prescribed through a pressure gradient $\frac{\Delta P}{\Delta y}$. A additional pressure offset, over-pressure and a reservoir pressure gradient can also be applied. The initial temperature follows the predefined geothermal gradient $\frac{\Delta T}{\Delta y}$.

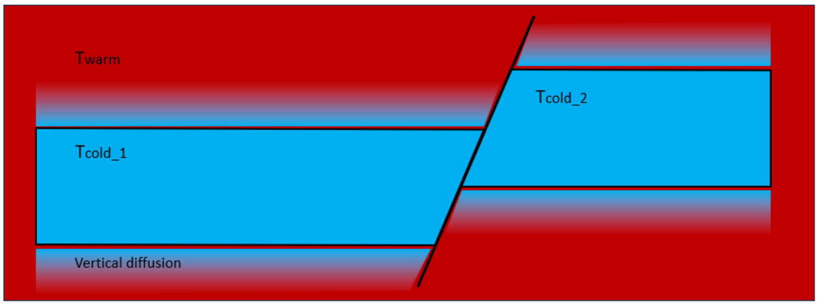

Figure 5.2: Assumption temperature distribution Panther

Poro- and thermo-elastic stress behaviour

The poro- and thermo-elastic stress changes are calculated using the closed-form solutions by Jansen, Singhal and Vossepoel (2019) (Jansen et al., 2019). These solutions consider only the most essential features of a fault with offset. The reservoir is considered to be an inclusion in a elastic medium experiencing displacements through poro- and thermo-elastic changes, for which a solution can be found with the use of Green's functions, according to the Theory of Inclusions (Jansen et al., 2019) (Eshelby, 1957). The Theory of Inclusions is then used to derive closed-form solutions for stress arching ratios. These ratios give an indication of the stress changes patterns, as discussed in Chapter 3.2.

5.2. Model scenarios

Three geometries will be considered based on the radius of the cooled region and the distance between the injector and the fault. A schematic of the geometry of the first scenario is depicted in Figure 5.3. This first geometry represents the case in which the fault does not have an offset and where sandstone is juxtaposed against sandstone. The cold front surpasses the fault and the fault experiences double sided cooling. The fault is therefore assumed to be permeable.

Figure 5.3: Schematic of geometry first scenario with double sided cooling of the fault

In the second scenario, Figure 5.4 represents the case in which the fault has an offset larger than the reservoir thickness and where sandstone is fully juxtaposed against claystone. As claystone has a low permeability it can be assumed the cold front does not flow past the fault, only to a small extent through diffusion, the fault is cooled on only a single side. This scenario can also represent the case in which the fault is assumed to be impermeable, independent of the lithology on the other side of the fault.

Figure 5.4: Schematic of geometry second scenario with single sided cooling of the fault

The third model scenario represents a combination of the first and second model scenario, in which the fault has a half-reservoir-thickness offset. Here sandstone is juxtaposed against sandstone for one half and juxtaposed against claystone for the other half. The fault therefore experiences double sided cooling but with an offset, as shown in Figure 5.3.

Figure 5.5: Schematic of geometry third scenario with double sided cooling of the fault, with a half-reservoir-thickness offset

5.3. Pressure

As discussed in the background chapter the injection of cold water not only affects the temperature in the reservoir but the pressure as well. Pressure changes are mainly concentrated near the injection point and decay rapidly, as shown in Figure 5.6. This plot uses the input from Table 5.1. The original reservoir pressure is 22.2 MPa, the pressure change caused by the cold water injection reaches a maximum of approximately 1 MPa within the first tens of meters around the well. At the location of the presumed fault the change in pressure is even less than 0.5 MPa. In this research drained conditions are assumed and therefore does not consider poro-elastic stresses. The focus lies on the thermo-elastic effects as these are seen as the driver behind induced seismicity in geothermal projects (L. Buijze et al., 2021). Panther contains the option to "switch off" pressure or temperature in order to focus on either of them. On the base of the above mentioned considerations the pressure effects were "switched off", and therefore drained conditions apply.

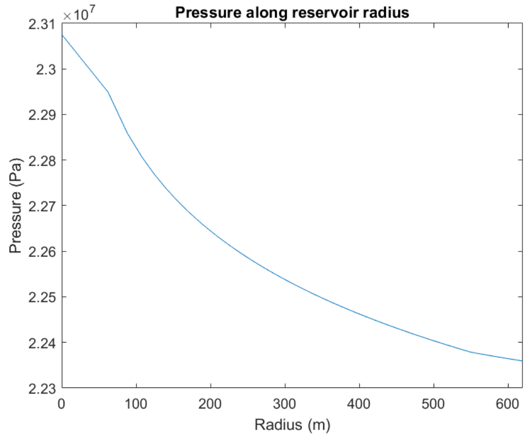

Figure 5.6: Pressure distribution along reservoir caused by injection

5.4. Temperature

Panther assumes a uniform temperature distribution and cooling over the whole reservoir, as shown in the schematic in Figure 5.2. To determine the temperature change that is to be used in the model a simplified temperature curve is plotted using the following equation (Mossop, 2001), which was also used by Fokker et al. (2023) (Fokker et al., 2023):

$$T_{aq}(r,t) = T_0 + \Delta T_0 erfc[\frac{ar^2}{\sqrt{t-cr^2}}]H(t-cr^2) \tag{5.1}$$

with

$$a = \frac{\pi K_{rock}}{\dot{m}C_{fluid}\sqrt{\kappa_T}}; b = \frac{1}{2\sqrt{\kappa_T}}; c = \frac{\pi h \xi \rho_{fluid}}{\dot{m}}$$

$$\kappa_T = \frac{K_{rock}}{(\rho C)_{rock}}; \xi = \frac{(\rho C)_{rock}}{(\rho C)_{fluid}}$$

where T_0 is the initial temperature [K], ΔT_0 the temperature difference between the initial temperature of the rock and the injection fluid [K], r the radial distance from the well bore [m], t the time since the start of injection [s], H the Heaviside function, κ_T the thermal diffusivity [m^2/s], ρ density [kg/m^3], K the thermal conductivity [W/mK], C the heat capacity [J/kgK], h the aquifer thickness [m] and $\dot{m}$ the mass injection rate [kg/s]. The values used for the calculations can be found in Table 5.1. They are based on average values for sandstones taken from literature or based on data taken from the Winningsplan (*Winningsplan Ammerlaan Geothermie*, 2019) and PanTerra (PanTerra, 2023). The plot of the resulting curve can be seen in Figure 5.7.

Two assumptions need to be made based on this curve, a single value for the cooled reservoir temperature and the width of the footwall. The approach for the single temperature value was to use the temperature at the fault after 35 years of injection, as that is the location of interest. The calculations show that at the presumed location of the fault, at 450m (see Chapter 4.2), the temperature is approximately 39°C or 312 K after 35 years of cold water injection. This means that the reservoir will experience a cooling of 40 degrees, as the original reservoir temperature was 79°C (PanTerra, 2023).

The approach for the footwall width was to use a temperature range with the temperature at the fault (39°C or 312K) as the average and the injection temperature (31°C or 304K) as the lowest end. This means that the highest end of the range is 47°C or 320 K, which corresponds to a distance of approximately 100m away from the fault. This 100m was used as the footwall width.

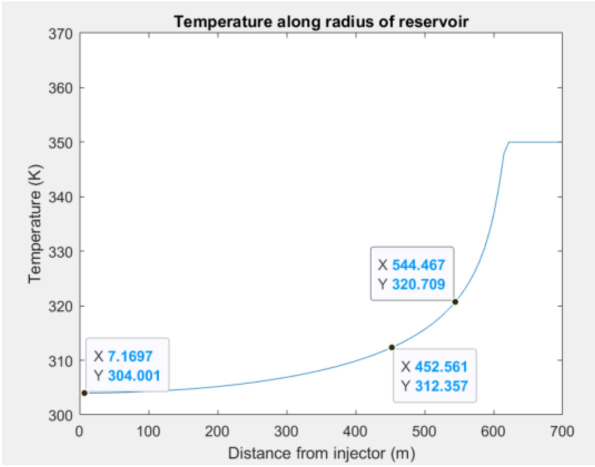

Figure 5.7: Temperature along reservoir after 35 years of cold water injection

Variable	Symbol	Value	Unit	Source
Initial temperature	T_0	352	K	(*Winningsplan Ammerlaan Geothermie*, 2019)
Difference between the initial rock temperature and injected water temperature	ΔT	40	K	(*Winningsplan Ammerlaan Geothermie*, 2019)
Thermal conductivity rock	K_{rock}	2.5	W/mK	(Blackwell & Steele, 1989) (Clark, 1966)
Density rock	ρ_{rock}	2200	kg/m^3	(GPG, 2017)
Density fluid	ρ_{fluid}	1154	kg/m^3	(Hutka et al., 2023)
Specific heat capacity rock	C_{rock}	870	J/kgK	(Xiong et al., 2020)
Specific heat capacity fluid	C_{fluid}	4180	J/kgK	(Manya, Antal Jr, Kinoshita, & Masutani, 2011)
Height reservoir	h	225	m	(Peeters, 2024)
Mass injection rate	$\dot{m}$	88.9	kg/s	(*Winningsplan Ammerlaan Geothermie*, 2019)

Table 5.1: Overview variables used in the pressure and temperature calculations and their values

5.5. Input parameters

All input parameters in Panther are listed in Table 5.2. The variables were grouped based on their properties and effects.

Group	Variable
Reservoir Geometry	
	Width HW
	Width FW
	Thickness
Fault Properties	
	Dip
	Dip Azimuth
	Throw
	Static Friction Coefficient
	Dynamic Friction Coefficient
	Critical Slip Distance
	Cohesion
Medium properties	
	Youngs modulus
	Thermal Expansion Coefficient
	Thermal diffusivity
	Biots Coefficient
	Poissons Ratio
Hydraulic efffects	
	Hydraulic diffusivity
Stresses	
	Ratio sH/sh
	Ratio sh/sv

Table 5.2: Overview of all variables available in Panther and their assigned group

All variables were changed one by one to assess which factors had an effect on stress changes and fault slip. The variables that did not show any effect were filtered and for the remaining variables appropriate values for a PNA base case were taken from the Winningsplan, Instemmingsbesluit, studies conducted by PanTerra and Stefan Peeters, as well as taken from or based on literature. The source of each value is indicated in Table 5.3. The values for the variables that did not affect the results were kept on the default value used in Panther, unless a clear value was found in the reports or literature. For example, the direction of σ_H did not influence fault slip but a clear value was found in literature, therefore this value was used for completeness.

Group	Variable	Value	Range	Source
Reservoir Geometry				
	Width HW	1000 m		
	Width FW	0m (single sided), 100m (double sided)		
	Thickness	225 m	175 - 275	(Peeters, 2024)
Fault Properties				
	Dip	65	55 - 75	(Peeters, 2024)
	Throw			
	Static Friction Coefficient	0.6	0.5 - 0.7	(PanTerra, 2023)
	Cohesion	0 MPa	0 - 4	(PanTerra, 2023)
Medium properties				
	Youngs modulus	15 GPa	10 - 19 GPa	(Soustelle, ter Heege, Buijze, & Wassing, 2022) (A. Muntendam-Bos, 2021)
	Thermal Expansion Coefficient	$1.5e^{-5}$ K^{-1}	1.0 - $2.5e^{-5}K^{-1}$	(Kirk & Williamson, 2012) (Soustelle et al., 2022)
	Thermal diffusivity	1.9 $e^{-6}m^2/s$	1.5 - 2.3	(Fuchs et al., 2021)
	Poissons Ratio	0.15	0.1 - 0.25	(Soustelle et al., 2022)
Stresses				
	sh	15.8 MPa/km		(A. Muntendam-Bos, 2021) (PanTerra, 2023)
	sH	15.8 * 102 or 103% MPa/km (anisotropy between horizontal stresses is 2-3%)	16.1 - 16.3 MPa/km	(Van Eijs, 2015)
	sv	22.5 MPa/km	22 - 23 MPa/km	(Verweij, Boxem, & Nelskamp, 2016)/ (PanTerra, 2023)
	Ratio sH/sh	1.025	1.02 - 1.03	
	Ratio sh/sv	0.7	0.69 - 0.72	

Table 5.3: Overview of variables affecting fault slip in Panther and their 'group' and value for the base case

Parameter	Value
Geothermal gradient	31 °C/km
Temperature gradient offset	10 °C
Pressure gradient	10.5 MPa/km
Pressure gradient offset	0 MPa/km
Hydrostatic overpressure	0 MPa/km
Pressure gradient reservoir fluid	10.5 MPa/km

Table 5.4: Temperature and pressure gradient input used in Panther

Reservoir Geometry
As discussed more elaborate in Chapter 4.2, the distance between the injector and the fault is 450m according to the interpretation of Stefan Peeters. This distance and the estimated radius of the cooled region are important for the width of the hanging wall and footwall. The diameter of the cooled region sets the length of the modelled reservoir section, which is 1100m. As the fault is located 450m away from the injector in the middle of the cooled region, the total width of the hanging wall is 1000m. The injector is not modelled but as the cold water would propagate radially outwards the middle of the cooled region is taken as the injector location. The footwall width is 100m, as that is the distance the cooled region extents beyond the fault. In the case of single sided cooling the footwall width is set to 0m and the hanging wall width stays 1000m.

PanTerra estimated the top depth to be 2040m (PanTerra, 2023) and Stefan Peeters interpreted the total thickness to be 250m and the net-to-gross ratio 0.9 (Peeters, 2024). Therefore the thickness used in the model is 225m. The half-reservoir-thickness offset used in the third model scenario is 113m.

Fault Properties
As discussed in Chapter 4.2 there is a discrepancy between interpretations done on the faults near the wells, and therefore also on the dip angle of the fault. The dip is set to 65 degrees, as per the interpretation of Stefan Peeters which is used in this project. (Peeters, 2024)

The static friction coefficient is taken to be 0.6, which is a relatively standard value and the cohesion is taken to be 0 MPa, which are both used by PanTerra in their research on the Pijnacker location and acts as a conservative assumption.

Medium properties
The Young's modulus used in the model is 15 GPa. This is based on the results from Soustelle, ter Heege, Buijze and Wassing (2022). The porosities in this model are slightly lower than in the paper, so the Young's modulus was taken as slightly higher.

The thermal expansion coefficient used in the model is 1.5 K^{-1}. (Kirk & Williamson, 2012)

The thermal diffusivity used in the model is 1.9 $e^{-6}m^2/s$, taken from the work by (Fuchs et al., 2021), which gave an indication of the thermal diffusivity of a sandstone based on its porosity.

The Poisson's ratio used in the model is 0.20, based on the results from Soustelle, ter Heege, Buijze and Wassing (2022).

Stresses
The value for sh was taken from (A. Muntendam-Bos, 2021), 15.8 MPa/km. As the anisotropy of the horizontal stresses is 2-3% (Van Eijs, 2015) the value for the sH/sh ratio is 1.02-1.03. The value 1.02 is used in the model.

The vertical stress in the WNB is 22 MPa/km (or 23 MP/km) and the ratio of sh/sv used in the model is therefore 0.72 (Verweij et al., 2016)

5.5.1. Base case

The three model geometries described above will be used in Panther and the resulting stress changes compared to each other. Cases will be run without aseismic slip and diffusion at first the evaluate the most basic form of the results. After that one additional step in terms of complexity will be made by applying the effect of diffusion. Lastly, aseismic slip will also be considered to create the most realistic case. The values used for the parameters in the base cases will be taken from Table 5.3.

5.5.2. Sensitivity analysis

A sensitivity analysis will be performed on the variables that showed to cause stress changes. The input range will be taken from Table 5.3. Through the sensitivity analysis it can be determined which parameters have the largest influence on stress changes and induced fault slip.

5.5.3. Metrics

The most important parameters and their effect in each model scenario will be plotted against three metrics indicative for fault (in)stability and give a summarizing overview. These metrics include (1) the temperature change needed for fault reactivation, (2) the maximum slip the fault experiences and (3) the slip patch length.

5.5.4. Inclusion of heterogeneous friction

In order to make a step towards a more geologically correct model an attempt will be made to include the effect of heterogeneous friction on stress changes and fault slip. Other research has already showed the importance of frictional properties on stress changes and fault slip (Hofmann et al., 2024) and therefore this inclusion of heterogeneous friction is an interesting addition to this study. In the previous results a single value for the frictional properties of sandstone were used, also in parts where the fault cuts through claystone. In reality the fault plane is not homogeneous and will have variations along the plane, even when flanked by sandstone on both sides. To mimic the variations in frictional properties the static friction coefficient was varied through the addition of a sin function.

In the double sided cooling model scenario without offset a value was used for the friction coefficient of claystone based on literature (0.5 (Bek, Jeftić, Strelec, & Jug, 2021)) This value was used in the base and seal, while the sandstone friction coefficient was used in the reservoir section of the fault plane. A schematic is included for clarity in Figure 5.8. The y-axis represents depth with $y = 0$ being $y_{mid-depth}$.

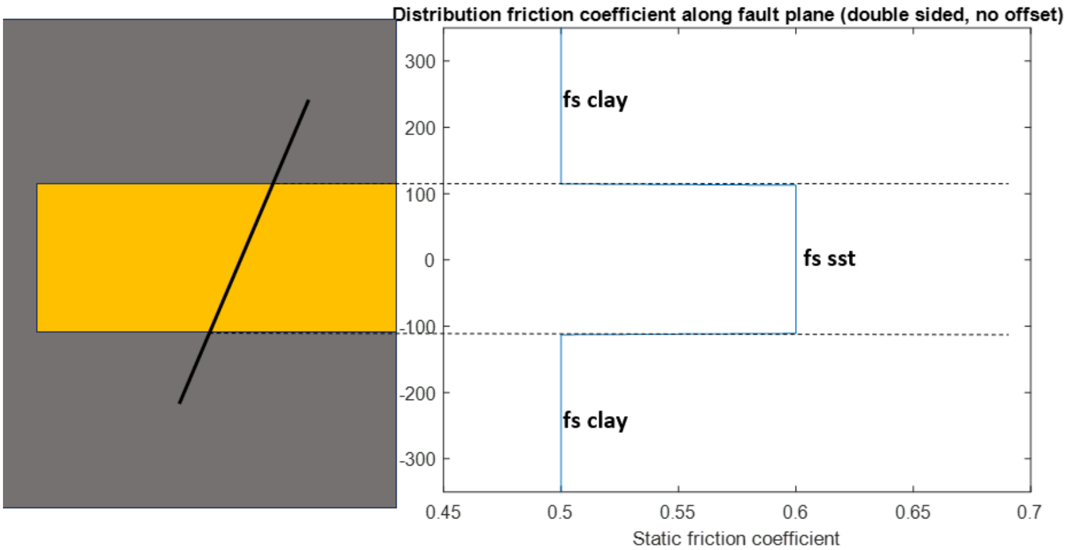

Figure 5.8: The distribution of the heterogeneous friction coefficient along the fault plane based on sandstone and claystone

In the single sided cooling model scenario the average of the claystone and sandstone friction coefficients was used (0.55). This value was used across the whole model, under the assumption that the fault plane will contain both sandstone and claystone along the fault, as it is found that fault planes with offset which have different rock types on either side contain a varying rock composition (Tesei, Collettini, Barchi, Carpenter, & Di Stefano, 2014). As discussed in the section on geometry, this single sided cooling scenario can represent the case in which the fault is impermeable or the case in which the footwall is not near the hanging wall anymore, indicating that the fault has experienced a lot of slip. By using the average value of claystone and sandstone the second case is assumed for this analysis.

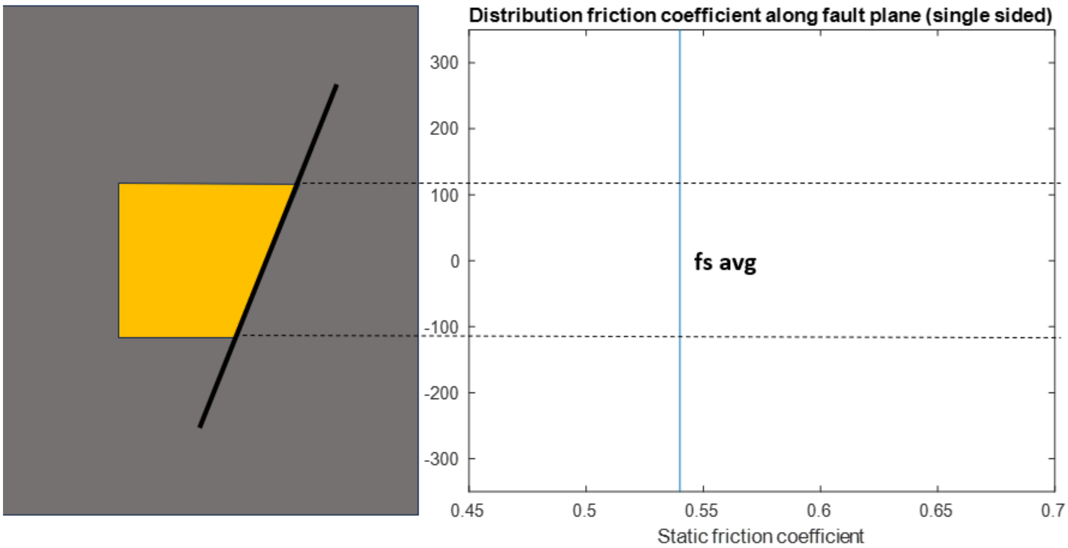

Figure 5.9: Distribution of heterogeneous friction coefficient along the fault plane based on the average value of sandstone and claystone

In the double sided cooling scenario with fault offset a combination of the above-discussed methods were used. In the reservoir-to-reservoir juxtaposed part mainly sandstone will be present, so along this section the sandstone friction coefficient will be used. In the sandstone-to-claystone juxtaposed parts the same average friction coefficient value as used in the single sided scenario will be applied. Lastly the claystone-to-claystone juxtaposed parts use the claystone friction coefficient. A schematic is included for clarity in Figure 5.10.

The results will be visualized through the usage of the same three metrics as used in the analysis of the original data.

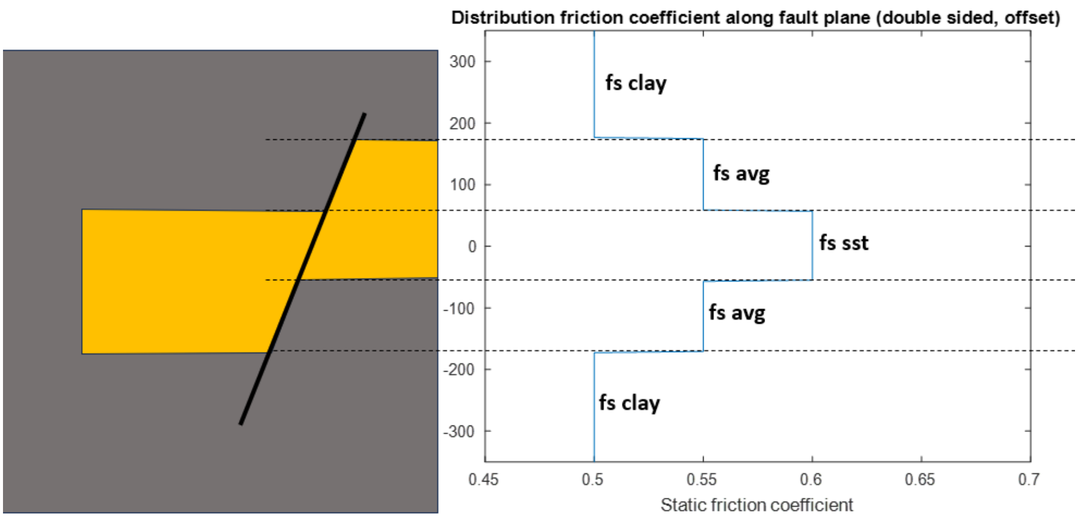

Figure 5.10: Distribution of heterogeneous friction coefficient along the fault plane based on the friction coefficients of sandstone, claystone and the average of both

6

Results Base Case

This chapter contains the results of the three base case scenarios (model geometries). These are (1) single sided cooling of the fault, (2) double sided cooling, without fault offset and (3) double sided cooling, with fault offset. They mimic the cases in which sandstone reservoir rock is fully juxtaposed against low-permeable claystones, sandstone reservoir rock is fully juxtaposed against sandstone and sandstone is juxtaposed a half-reservoir-thickness against low-permeable claystone and half-reservoir-thickness against sandstone, respectively. Input variables for the base cases can be found in Table 5.3. This chapter serves as an introduction to the way the results are depicted and will explain what can be seen and why. The goal is to discuss the effect of the different modelling scenarios on stress changes and fault slip.

The results from a run contain five graphs with the temperature, normal and shear stresses, Shear Capacity Utilization and slip on the fault over a depth range of -1850 until -2400. The reservoir is located between -2040m and -2290m.

6.1. Three scenarios without aseismic slip and diffusion

Panther has the option to "switch off" aseismic slip and diffusion, which will be used for the first results in order to focus on the effect of the different geometries, leaving out extra influences from aseismic slip and diffusion.

Figures 6.1, 6.2 and 6.3 show the base case results of the three model scenarios, with their geometries on the left of the results.

The leftmost plot shows the temperature distribution along the fault. The temperature in the seal and base follows the geothermal gradient of 31 °C/km while the fault experiences 40 degrees of cooling throughout the reservoir, as is prescribed in Panther (see Chapter 5.4). As there is no diffusion at work between the reservoir and the base and seal in this scenario, the temperature jumps between the geothermal gradient and the cooled reservoir temperature.

As the temperature change is very sharp, due to the sharp reservoir geometry, the normal and shear stresses show sharp changes in their plots too. In the two model scenarios where sandstone juxtaposes claystone the stress plots show peaks, while in the scenario where sandstone fully juxtaposed against sandstone the stress plots show jumps instead of peaks. These peaks and jumps correspond to the structural interfaces, as shown in Figures 6.1, 6.2 and 6.3. Work by Jansen, Singhal and Vossepoel (2019) also mentions these stress peaks and concludes that they are caused by singularities which occur in the analytical calculations. The origin of this result is the use of sharp reservoir geometries in the model, which are also used in this scenario (Jansen et al., 2019). Mathematically the peaks are infinite but they are cut off by Panther. These stress concentrations are present in reality, although smoother, and are the result of the cooled reservoir rock wanting to contract while the surrounding rock does not (Jansen et al., 2019). Note that the shear stress range of the fully sandstone-to-sandstone juxtaposed case is less than for the other two. The cooled length of the fault in the scenario with half-reservoir-thickness offset is larger as a larger area is (cooled) sandstone at either side of the fault. For all scenarios the stress perturbations affect the fault past the reservoir section. As aseismic slip is not included the Shear Capacity Utilization (see Equation 3.7 in Chapter 3.1) can surpass the threshold value of 1 and no slip occurs. The SCU value is highest in locations where sandstone is juxtaposed against sandstone.

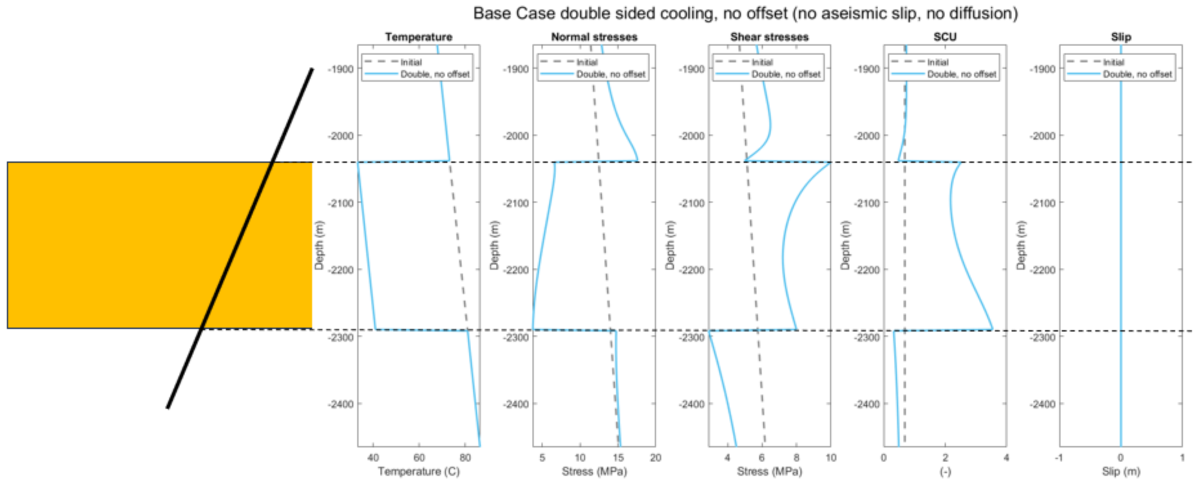

Figure 6.1: Model geometry double sided cooling without offset along with the base case results without aseismic slip and diffusion

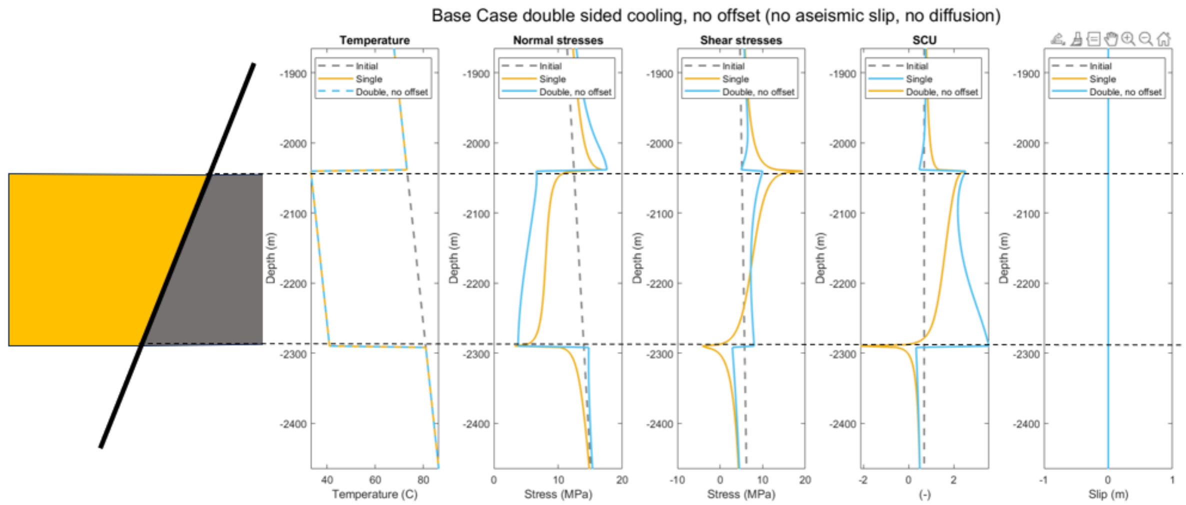

Figure 6.2: Model geometry single sided cooling (yellow) along with the base case results without aseismic slip and diffusion

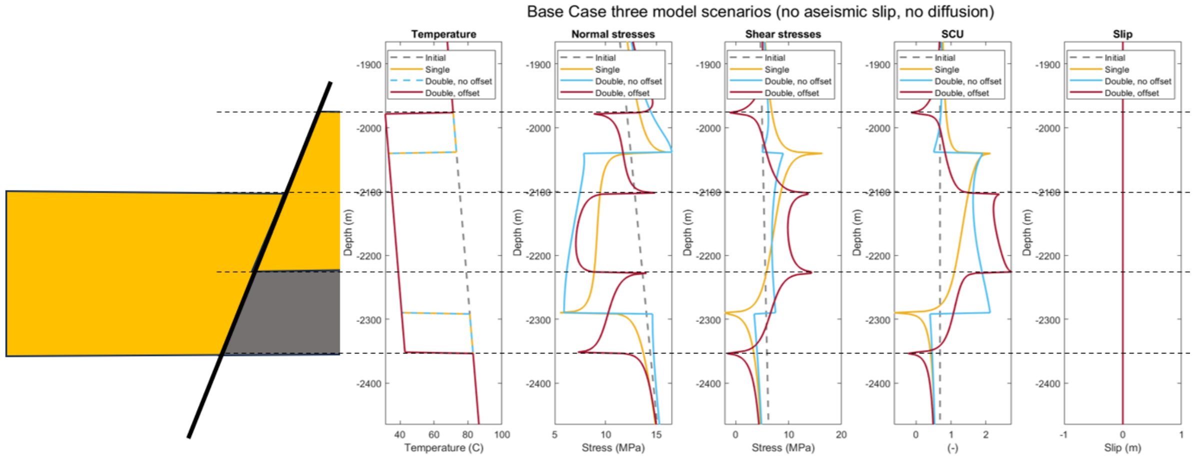

Figure 6.3: Model geometry double sided cooling with fault offset (red) along with the base case results showing peaks corresponding to the interfaces

6.2. Three scenarios without aseismic slip and with diffusion

In Figure 6.4 the aseismic slip remains "off" but diffusion is included. The temperature plot clearly shows that the cold temperature diffuses into the base and seal, where the rock now experiences some degree of cooling. The normal and shear stresses are by extent also affected and now show more rounded peaks at the reservoir-base and reservoir-seal interfaces. Temperature, normal stress and shear stress changes are smoothed out by the presence of diffusion. A similar trend can be noted in the SCU plot, as aseismic slip is not included here the SCU can surpass the threshold value of 1 and the slip remains zero.

The SCU for the single sided cooling case reaches a maximum near the reservoir-seal interface. In the double sided cooling scenario the peaks are at both interfaces, while remaining high throughout the reservoir. A similar pattern can be seen for the scenario including fault offset, with maxima in the sandstone-to-sandstone juxtaposed section. The SCU value of the double sided cooling case with offset is higher, although for a shorter section. The value of the SCU is higher in this case compared to the zero-offset case.

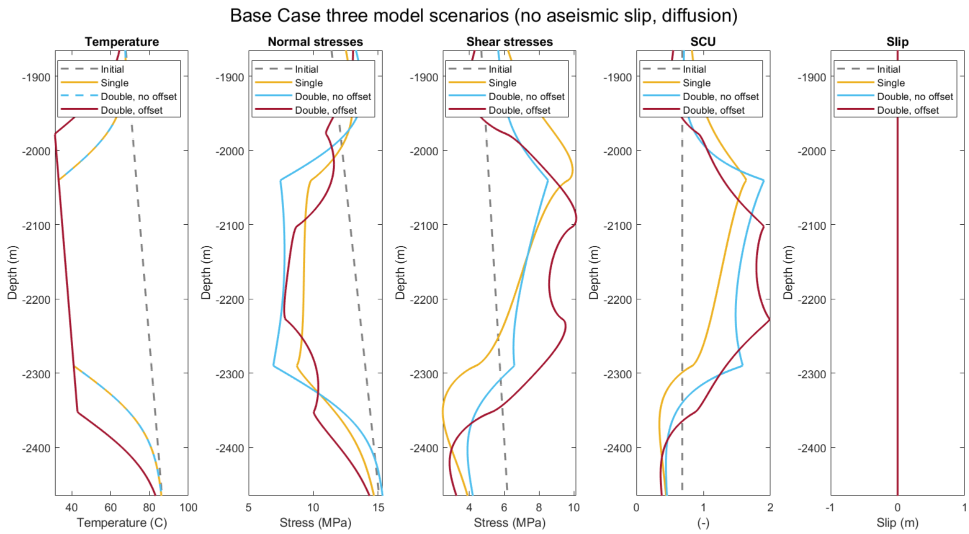

Figure 6.4: Three modelling scenarios without aseismic slip and with diffusion

6.3. Double sided cooling with fault offset, different conditions

Figure 6.5 contains only the model scenario with double sided cooling with fault offset, but for different conditions, which were used in the three figures above: (1) no aseismic slip and no diffusion, (2) no aseismic slip with diffusion and (3) aseismic slip with diffusion. This plot is used to show the effect of the three conditions on the same model scenario. The effect of temperature diffusion into the base and seal, the rounding of the sharp peaks, the effect of the SCU cut-off and shear stress relaxation are clearly noticeable.

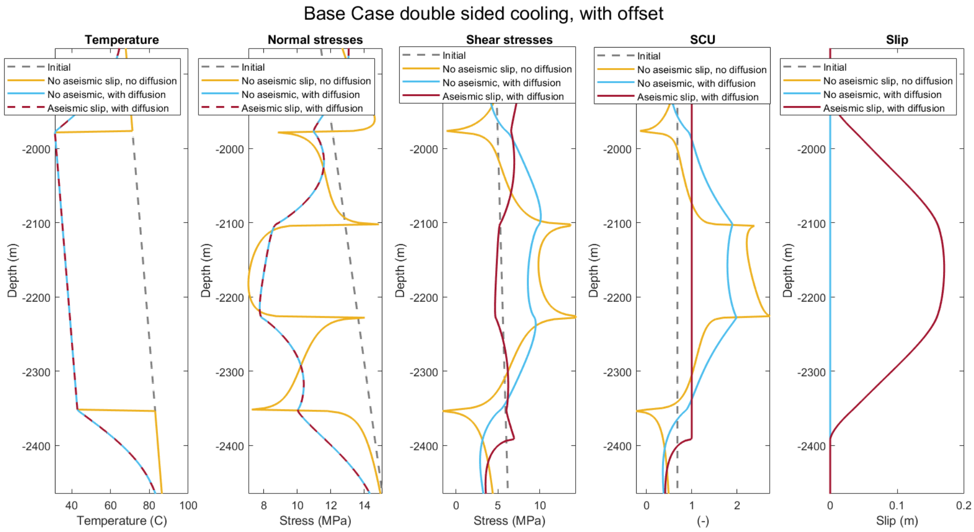

Figure 6.5: Model scenario of double sided cooling with offset for with and without aseismic slip and diffusion

6.4. Three scenarios with aseismic slip and diffusion

In Figure 6.6 both aseismic slip and diffusion are included. The temperature and normal stress plot remain equal to the previous figure. The difference is the SCU cut off at a value of 1, above which slip occurs, as visible in the rightmost graph. When slip occurs, shear stress relaxation takes place. The shear stress is transformed into slip, leading to a reduction in the shear stress over the plane which experiences slip. Note that the area experiencing slip is not contained within the reservoir, but extends into the base and seal. The length of plane experiencing slip in the single sided cooling scenario seems to be similar to the double sided cooling without offset, only slightly shifted upwards. The magnitude of slip is also comparable. In the modelling geometry with double sided cooling with offset the maximum amount of slip is largest.

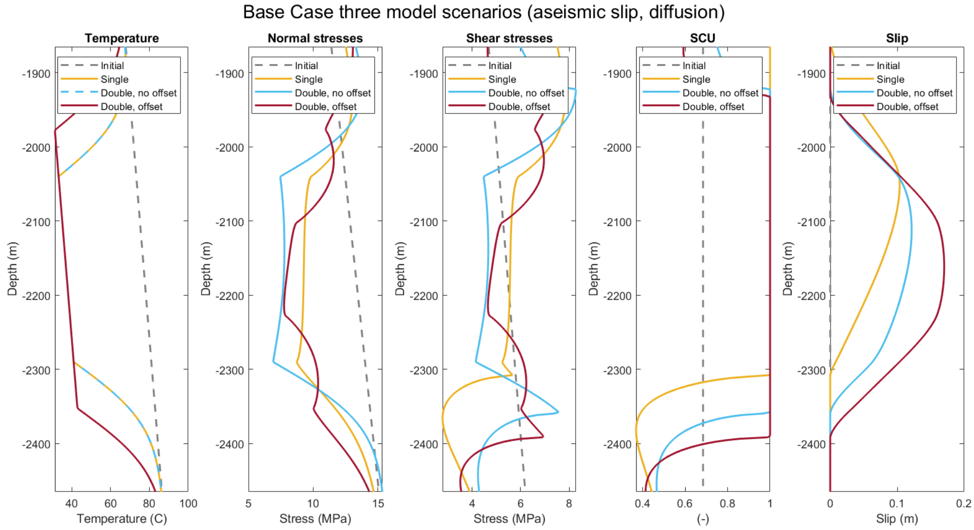

Figure 6.6: Three modelling scenarios with aseismic slip and diffusion

6.5. Conclusions base case

Among the main points of interest are that temperature changes affect a longer portion of the fault in the scenario containing offset and in this case the maximum slip is largest. The highest SCU values are reached at the sandstone-sandstone juxtaposed parts of the fault. Moreover, the zero-offset double sided cooling case is more stable than the offset case and both stress concentrations at the top of the hanging wall and the base of the footwall. Lastly, the single sided cooling case appears to show the least amount of maximum slip. The slip patch is situated at a slightly shallower part of the fault with respect to the other model geometries.

7

Results sensitivity analysis

A sensitivity analysis is performed to evaluate the influence of certain parameters on the temperature, stresses and fault slip. Besides that parameters with the highest destabilizing potential will be determined through this process. The model scenario used for this analysis is single sided cooling as this set-up is likely closest to reality considering the Pijnacker Geothermie case study, with the Delft Sandstone being fully juxtaposed against the Alblasserdam Member (see Chapter 4.3). The results for the other two model scenarios can be found in Appendix A. Ranges for the input are taken from Table 5.3. The result will be discussed and explained through the Mohr-Coulomb failure criterion and the thermo-elastic stress path parameter (Chapter 3).

7.1. Reservoir Geometry

By changing the thickness and width of the hanging wall and footwall the aspect ratio of the reservoir is altered. As discussed in Chapter 3 the aspect ratio influences the stress path, which can clearly be seen in the two figures below. A smaller hanging wall width experiences less stress changes and fault slip than a longer hanging wall. An increasing footwall width shows a similar trend. Additionally it moves the maximum slip increasingly towards the middle of the reservoir. The sensitivity of the changing footwall and hanging wall is essentially the sensitivity of the distance between the injector and the fault.

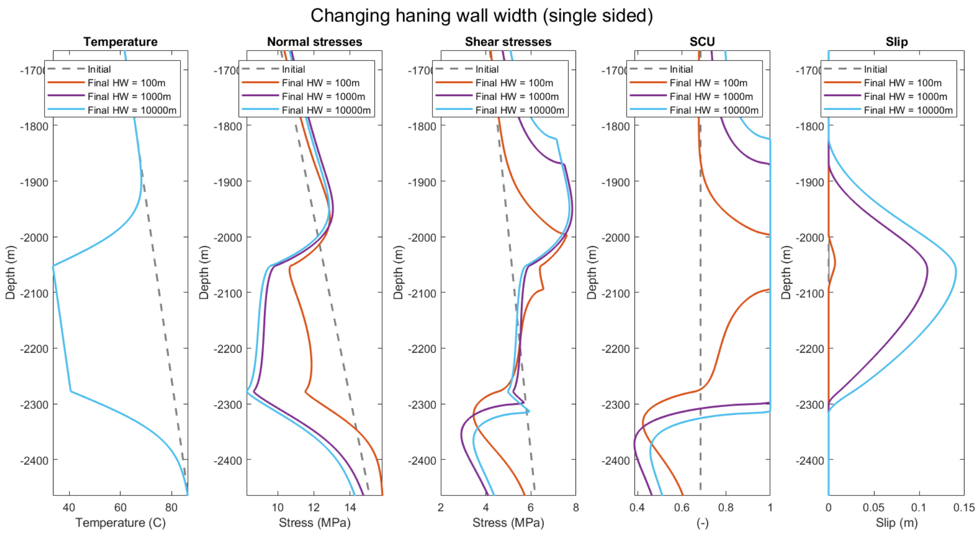

Figure 7.1: Sensitivity hanging wall width single sided cooling

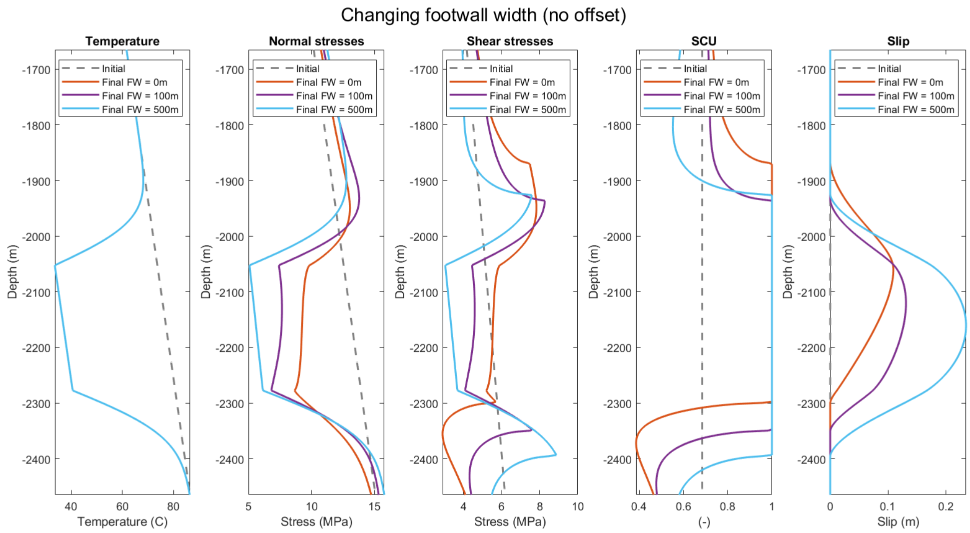

Figure 7.2: Sensitivity footwall width, without offset

Figure 7.3 shows the results of the sensitivity analysis on the effect of thickness in the scenarios of double and single sided cooling. The main effect is that the colder temperature and the resulting effect on the normal and shear stress extends further for a thicker reservoir. A thicker reservoir has a more extensive slip length as well as maximum slip.

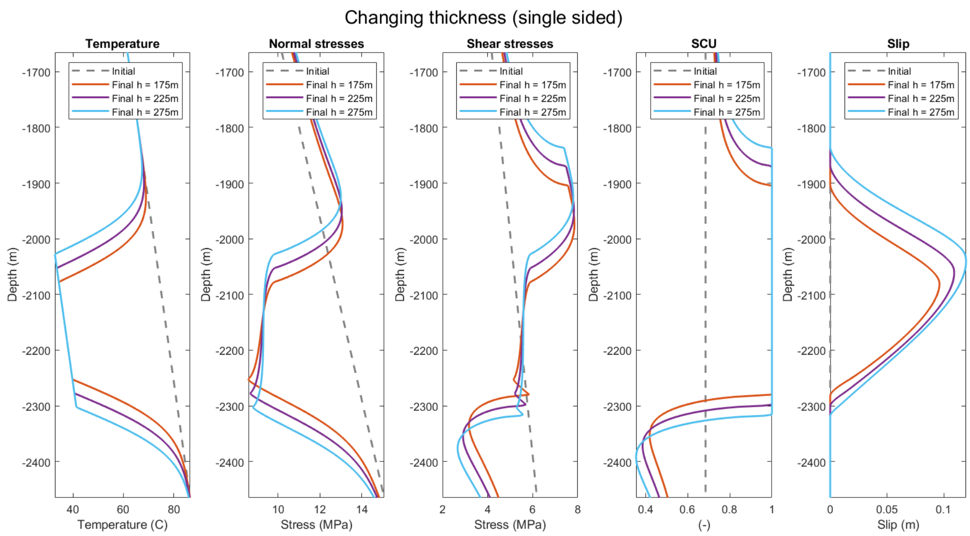

Figure 7.3: Sensitivity reservoir thickness single sided cooling

7.2. Fault properties

Figure 7.4 shows the effect of a changing dip angle on the results. A steeper dip angle results in a lower initial normal and shear stress. The least amount of slip occurs on the steeper slope, and the most in the slope which is 65°. The dip angle used in the base case is therefore the most destabilizing. The optimally oriented dip angle would be 60° but due the relative magnitudes of the stresses the fault is present in a normal faulting regime, the gentler slope of 55° is stabilizing.

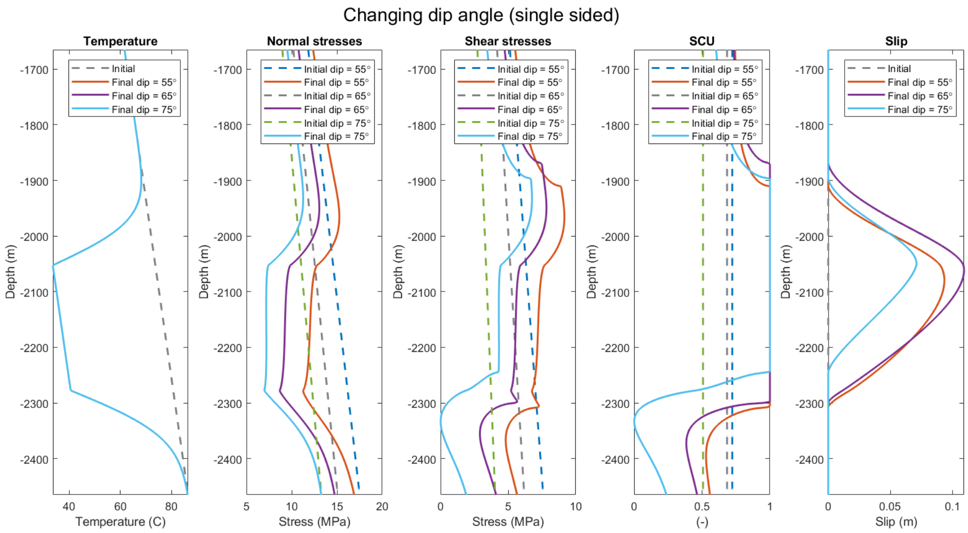

Figure 7.4: Sensitivity dip single sided cooling

Figure 7.5 shows the effect of changing the static friction coefficient. Normal stress is not affected but the shear stress, SCU and slip all are. This makes sense remembering the formulation of the Shear Capacity Utilization and the Mohr-Coulomb failure criterion (Equation 3.6, Chapter 3.1).

$$\tau_s = C + f_s \sigma_n'$$

$$SCU = |\frac{\tau}{C + f_s \sigma_n'}|$$

A reduction in static friction coefficient will result in a gentler failure slope and stress changes could therefore lead to reactivation sooner. The SCU is also directly affected by a decrease in f_s, meaning the threshold value of 1 is reached for a lower shear stress. The effect of changing the cohesion can also be explained with this relationship. If the cohesion increases the failure line moves up which results in a more stable situation, as is shown in the results in Figure 7.6. Similar to the friction coefficient, a reduction in cohesion results in a reduction of the denominator of the SCU formulation, noticeable through the increase in slip.

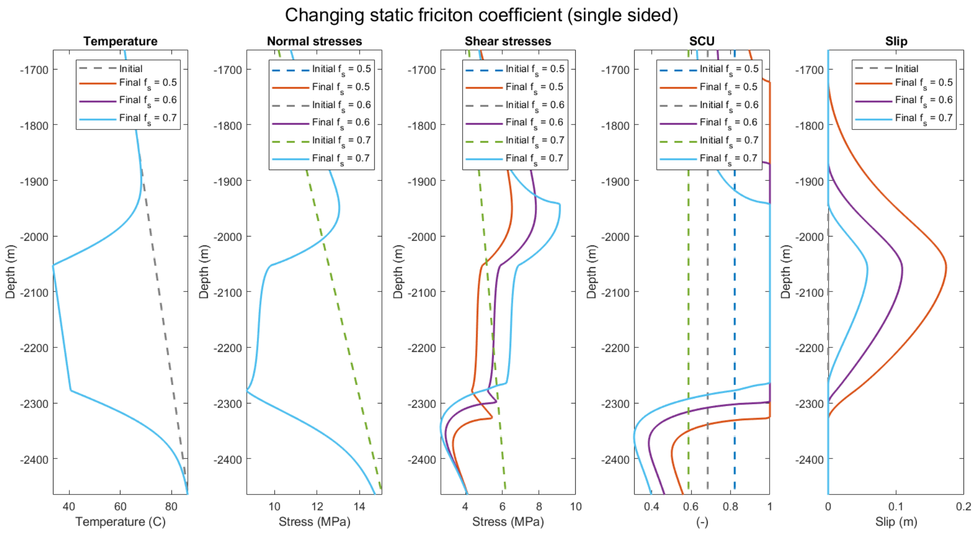

Figure 7.5: Sensitivity static friction coefficient single sided cooling

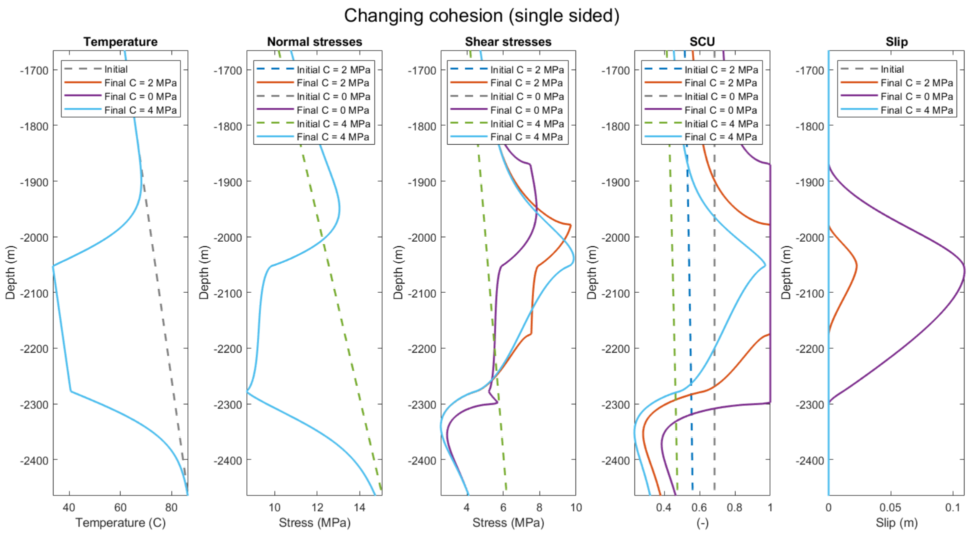

Figure 7.6: Sensitivity cohesion single sided cooling

7.3. Medium properties

The effect of the Young's modulus, the thermal expansion coefficient and the Poisson's ratio can all be explained through the thermo-elastic stress path parameter.

$$\Delta\sigma_h = \frac{E\eta\Delta T}{(1-\nu)}$$

For the same reduction in temperature the change in the minimum horizontal stress well be larger for a larger Young's modulus E and the same holds for a larger thermal expansion coefficient η. As a negative temperature change will cause the change in σ_h' to move towards the origin in the Mohr-Coulomb graph and towards the criterion line. Therefore a higher Young's modulus and thermal expansion coefficient are both more destabilizing. This is in accordance with the results in Figure 7.7 and 7.8, as well as with the work by Segall and Fitzgerald (1998) (Segall & Fitzgerald, 1998), Zang et al. (2023) (Zang et al., 2023) and Hutka et al. (2023) (Hutka et al., 2023). For one degree change in temperature the rock contracts or expands more, it is intuitive that this is more destabilizing. As mentioned before the contrast in behaviour will create stress peaks, they will be higher for a larger difference.

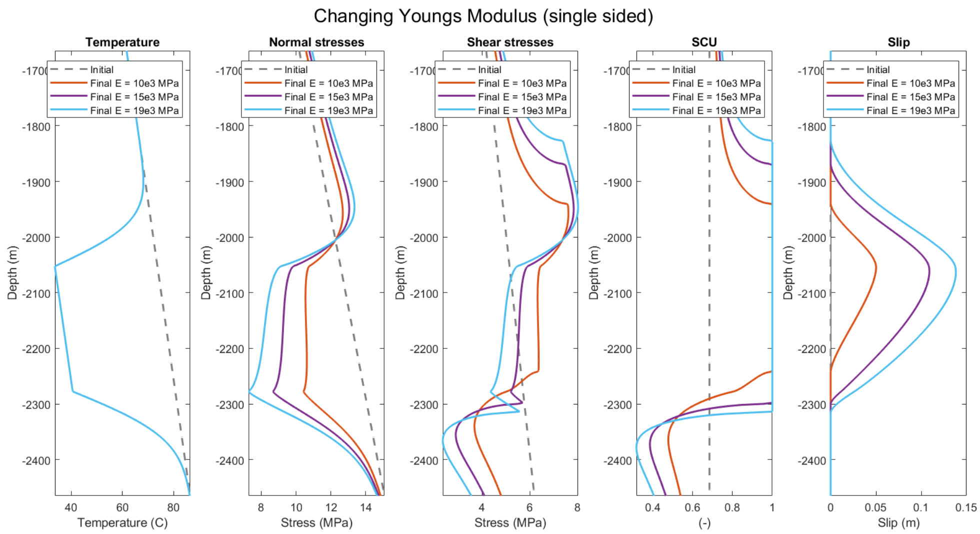

Figure 7.7: Sensitivity Young's modulus single sided cooling

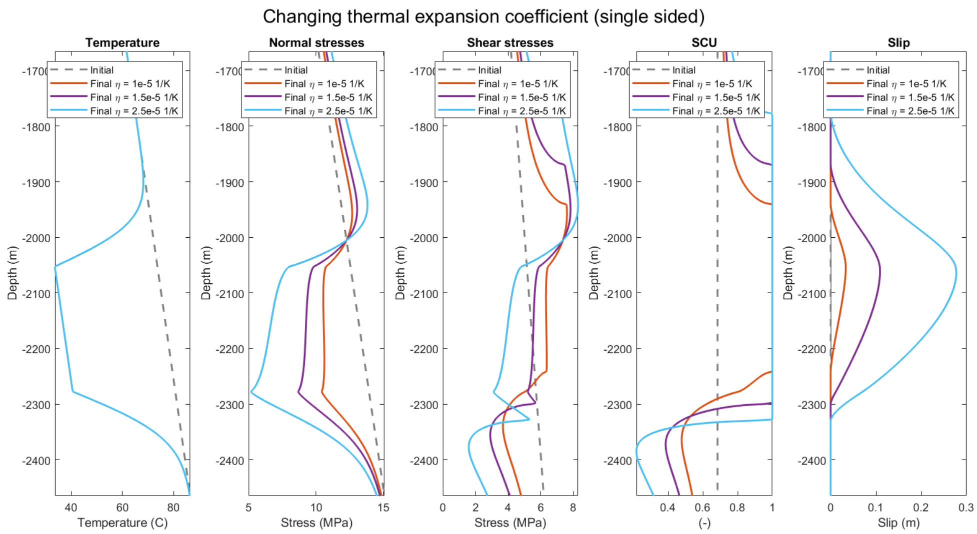

Figure 7.8: Sensitivity thermal expansion coefficient single sided cooling

The effect of the Poisson's ratio can be reasoned using the thermo-elastic stress path parameter as well. An increase in Poisson's ratio will shift the minimum horizontal stress towards the Mohr-Coulomb criterion and will therefore be more destabilizing. The Poisson's ratio is a measure of deformation laterally when loaded vertically, therefore a lower value of ν means that the rock expands less laterally.

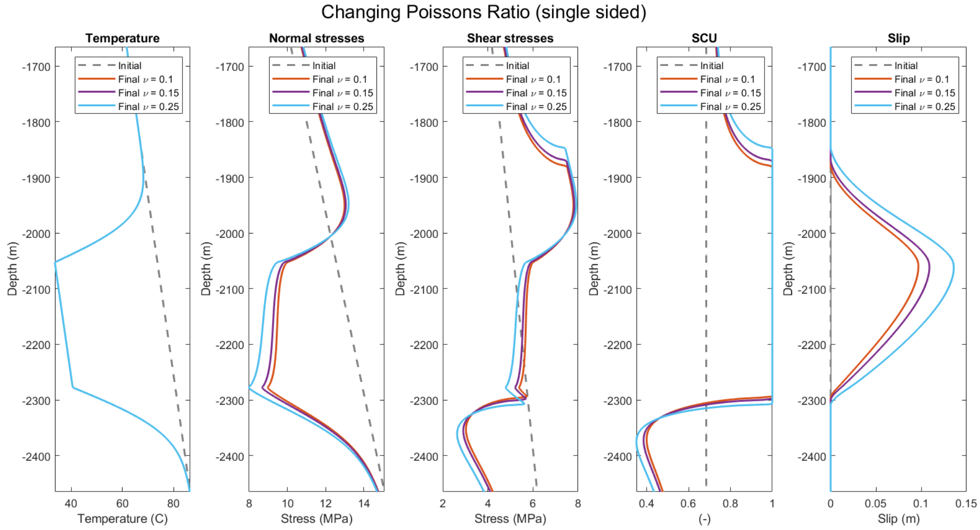

Figure 7.9: Sensitivity Poisson's ratio single sided cooling

The effect of changing thermal diffusivity is noticeable in the slight change in temperature in the base and seal, with more cooling for a higher thermal diffusivity, as was to be expected. The slip patch length is not significantly affected but the amount of slip is slightly larger for increasing thermal diffusivity.

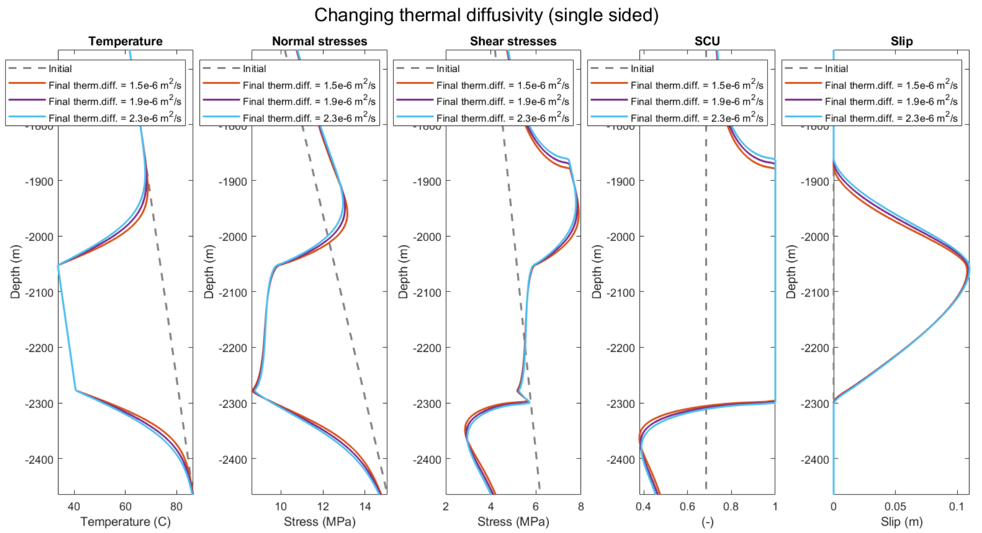

Figure 7.10: Sensitivity thermal diffusivity double sided cooling with offset

7.4. Stresses

The effect of a changing ratio between the minimum and maximum horizontal stress is barely noticeable. Only by focusing on the maximum slip a very minimum amount of more slip can be noticed for a ratio closer to 1. The ratio between the minimum horizontal and the vertical stress on the other hand is significant, which was also found by Zang et al. (2023) (Zang et al., 2023). This was as expected as a larger difference in σ_h' and σ_v' means that the Mohr-Coulomb circle grows, which is destabilizing.

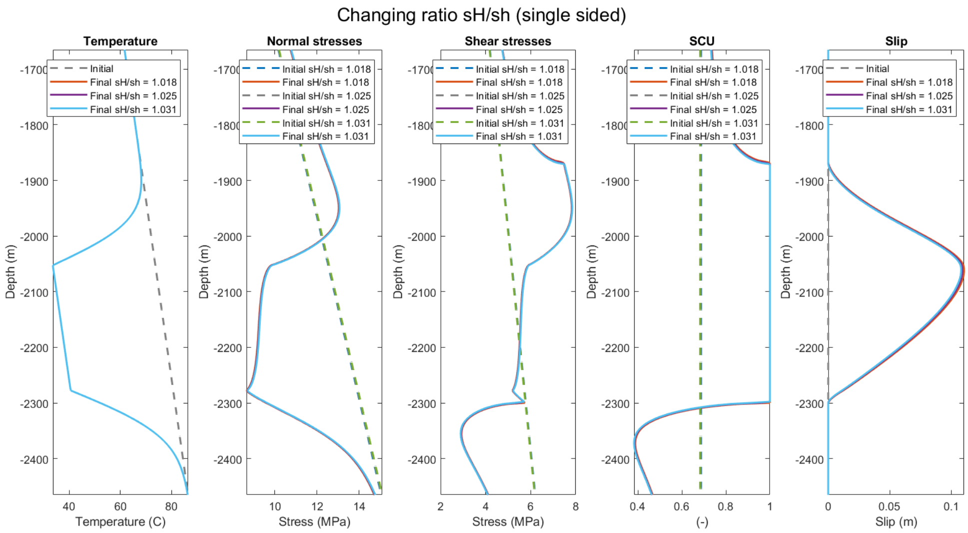

Figure 7.11: Sensitivity ratio sH/sh single sided cooling

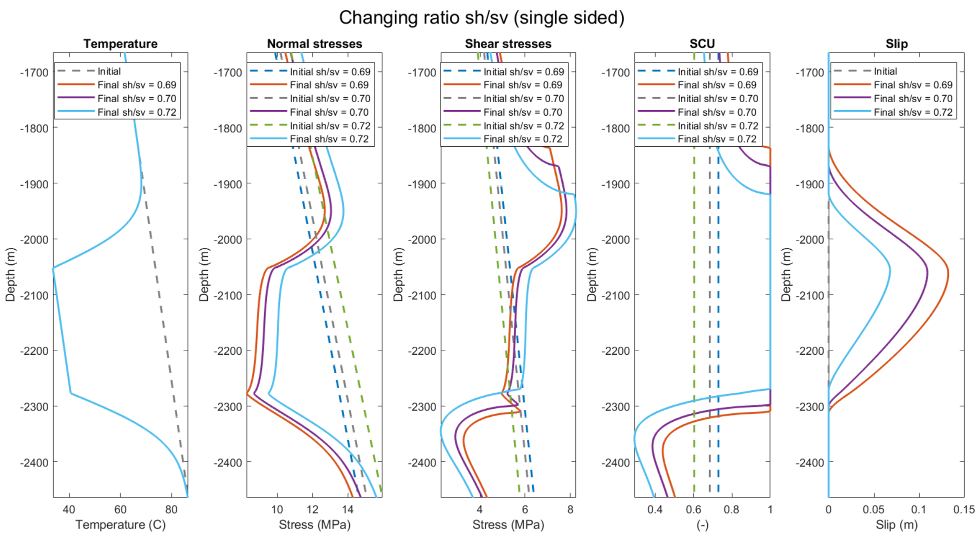

Figure 7.12: Sensitivity ratio sh/sv single sided cooling

7.5. Conclusion sensitivity analysis

The parameters showing the largest effect on fault slip are the Young's modulus, thermal expansion coefficient, static friction coefficient, the sh/sv ratio and the aspect ratio of the reservoir. The first four will be used for the next step, as the parameters affecting the aspect ratio are already investigated through the different scenarios. Data was extracted from the runs for several metrics. These metrics are temperature change needed for reactivation, slip patch length and maximum slip. These metrics are used in order to properly compare the effect of fault offset and single or double sided cooling on stress changes and induced fault slip.

8

Results metrics

In the previous Chapter the most important parameters for temperature induced stress changes and fault slip have been determined. To quantify the results three metrics have been selected, this will also give a clearer image of the combined effect of the most significant parameters and the different model scenarios.

The three metrics deemed applicable and useful are: (1) the temperature change at which the fault slip first occurs ($\Delta T_{reactivation}$), (2) the length along the fault which has experienced slip after 35 years of cold water injection and (3) the maximum slip. The results are depicted in plots with the most significant parameters (E, f_s, η, sh/sv) on the x-axes and the metrics on the y-axes. Each model scenario is indicated using a marker with colours corresponding to the legend of the base case in Chapter 6.

8.1. Young's modulus against the metrics

In the double sided cooling case with offset the temperature change needed to reactivate the fault is consistently lower than the other two, decreasing for a higher Young's modulus. Reactivation occurs for the same amount of cooling in the other two scenarios, except for the value in the middle of the Young's modulus range, where the single sided cooling needs a degree more cooling to reactivate.

The maximum amount of slip is significantly larger in the case of double sided cooling with offset, and the single sided cooling experiences the least amount op slip. However, slip lengths for a Young's modulus of 15GPa are quite comparable and the slip patch length for the highest Young's modulus in the single sided cooling even surpasses the slip patch length of the double sided cooling with offset.

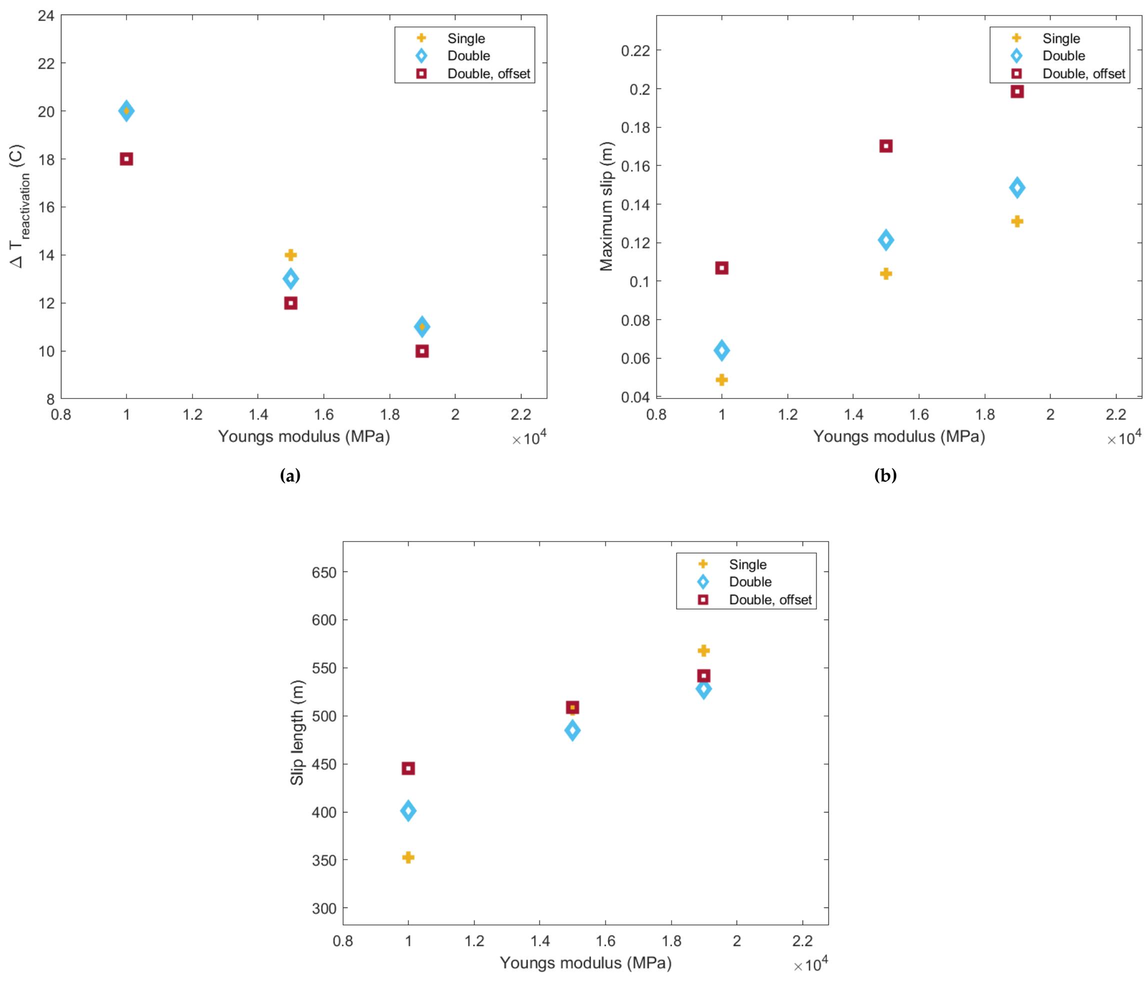

(a) (b) (c)

Figure 8.1: Varying young's modulus against three metrics for each model scenario

8.2. Static friction coefficient against the metrics

Figure 8.2a shows that, similar to the results in Figure 8.1a, the double sided cooling with offset scenario requires the least amount of cooling before slip starts to occur, followed by the other double sided case. Again single sided cooling is the most stable, although the difference between the three scenarios is not big. Again the slip patch length of the single sided cooling case is most sensitive to changes in the key parameter.

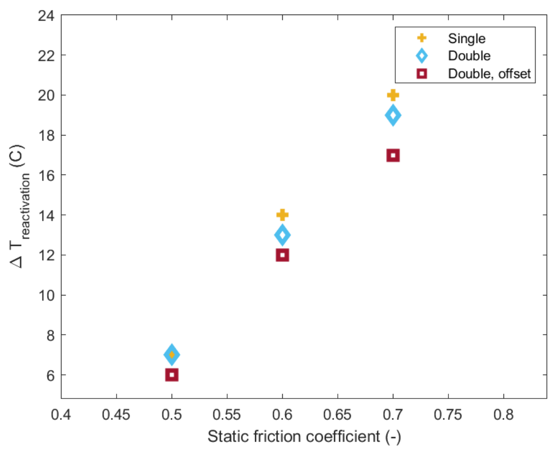

(a)

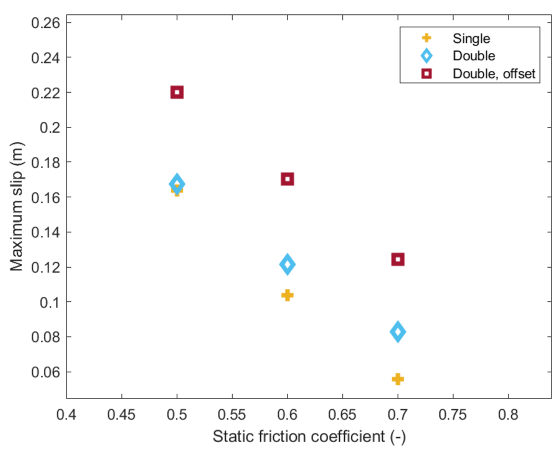

(b)

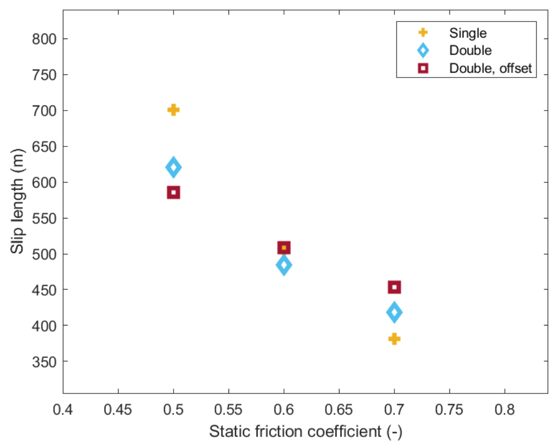

(c)

Figure 8.2: Varying static friction coefficient against three metrics for each model scenario

8.3. Thermal expansion coefficient against metrics

The thermal expansion coefficient and the reactivation temperature are negatively correlated, with the double sided cooling with fault offset generally needing the least amount of cooling. The cooling needed to reactivate all the scenarios becomes less for an increasing thermal expansion coefficient. The maximum slip figure shows the opposite relation, being positively correlated and having data points growing further apart for a larger thermal expansion coefficient. The slip patch length again shows the same pattern as the previous two slip patch length plots: double sided cooling with offset scenario has most slip for a low value of the thermal expansion coefficient but increases less than the single sided cooling increases for a larger thermal expansion coefficient. The double sided cooling without offset has slightly shorter or similar slip length compared to the other double sided cooling case.

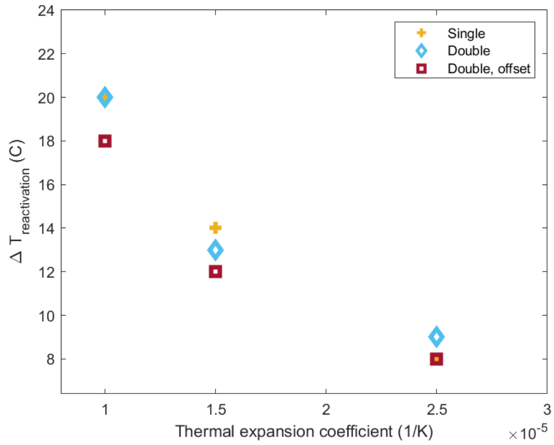

(a)

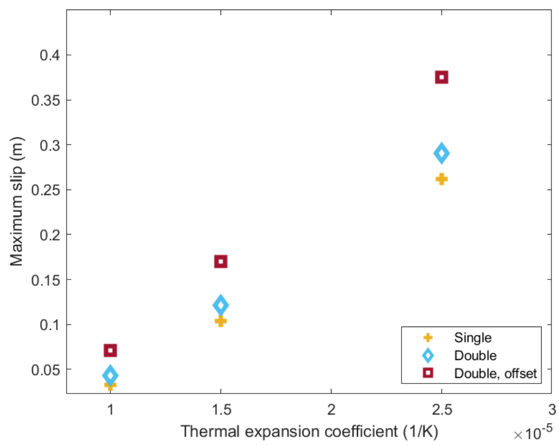

(b)

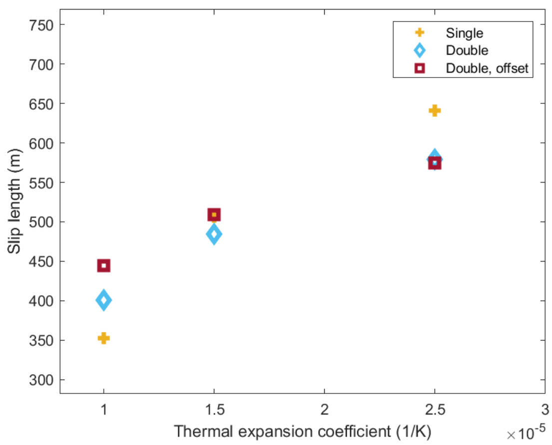

(c)

Figure 8.3: Varying thermal expansion coefficient against three metrics for each model scenario

8.4. Ratio sh/sv against metrics

Similar to the other metrics the offset model scenario experiences the largest maximum slip and needs the least amount of cooling for the onset of aseismic slip. The slip patch length of the single sided cooling scenario is most sensitive to changes in the sh/sv ratio.

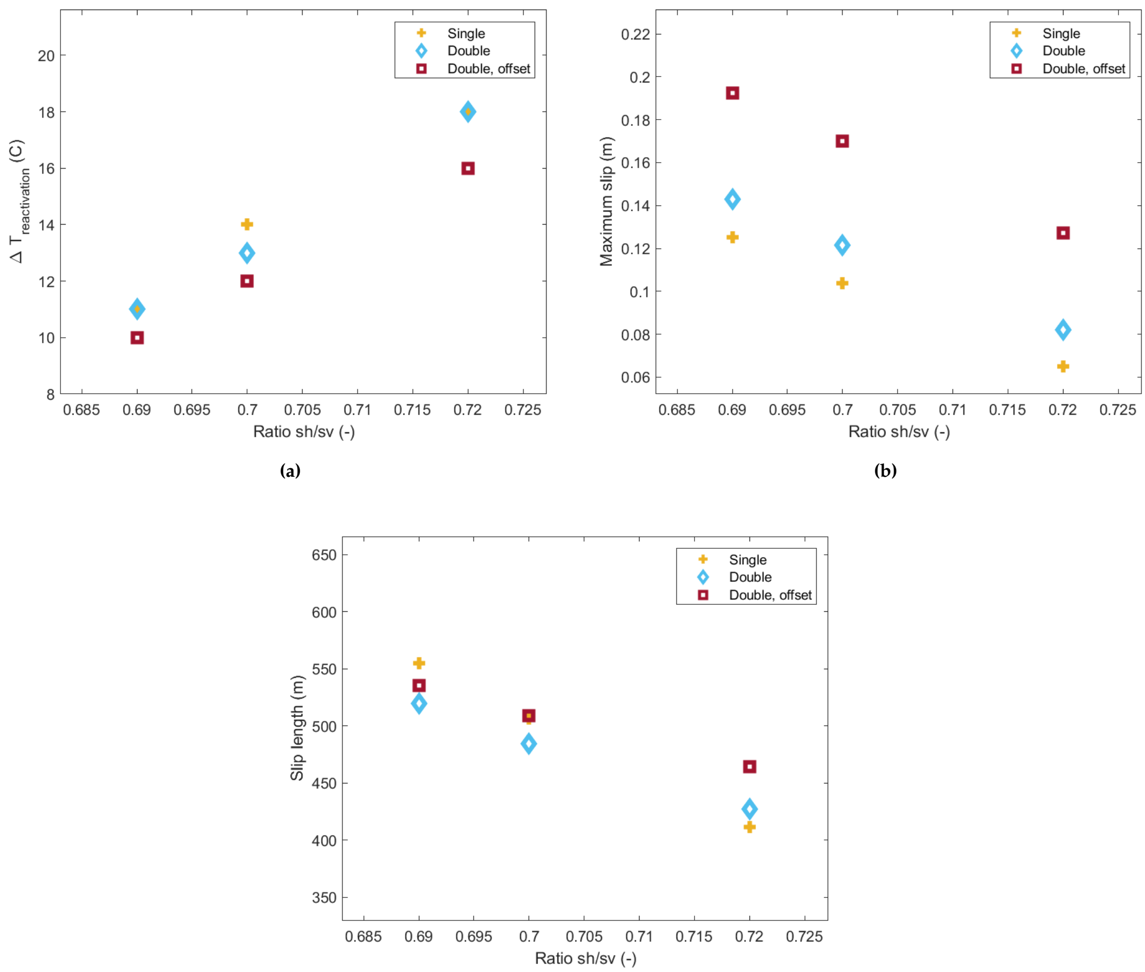

(c)

Figure 8.4: Varying sh/sv ratio against three metrics for each model scenario

8.5. Conclusion metrics

Double sided cooling with offset has highest maximum slip for every value of all parameters. For changing Young's modulus, static friction coefficient and the sh/sv ratio the change in maximum slip seems constant relative to the other two scenarios. For changing thermal expansion coefficient the maximum slip increases more than the other cases. The double sided cooling case also needs the least amount of cooling before the fault reactivates. For a high potential situation single sided cooling experiences the largest length along which slip occurs, while for low potential situations the double sided cooling with offset shows the longest slip patch length. The double sided cooling without offset is generally somewhere in between the other two model scenarios.

9

Results inclusion of heterogeneous friction

This section discusses the results of the inclusion of heterogeneous friction in the fault plane. This was done to make a step towards a more geologically correct model in important aspects of induced stresses and fault slip. The same method was applied as in the previous chapter, using the same metrics and visualization. The way an attempt was made to include heterogeneous friction can be found in Methodology chapter (5).

9.1. Young's Modulus against the metrics

The first thing that stands out is that the reactivation temperature changes are between 5 to 10° lower than the original data with homogeneous friction. A second difference in the reactivation temperature change plot is that the double sided cooling scenario without offset reactivates fastest, in stead of the scenario with offset in the case without heterogeneous friction. This could be due to the fact that in this model scenario the lowest friction coefficient value is used at the location closest to the stress concentrations. In the single sided cooling case the friction coefficient used is slightly higher and in the model scenario with offset the low claystone-based friction coefficient is used in a region further away from the stress concentrations at the structural interfaces.

The amount of maximum slip is overall slightly higher but has the same trends as seen earlier without the inclusion of heterogeneous friction. The case with offset still experiences the largest amount of slip, and the single sided cooling scenario the least. The difference between maximum slip in the single sided and double sided without offset scenario's seems to be smaller than before the addition of heterogeneous friction.

Similar to the maximum slip, the slip patch length is slightly higher than the case with homogeneous friction. Another difference is the somewhat equally sensitive double sided cooling without offset scenario to a changing Young's Modulus compared to the single sided cooling case. Before, the single sided cooling case was clearly the most sensitive.

It was to be expected that the inclusion of heterogeneous friction would result in a lower reactivation temperature difference and an increase in both slip patch length and maximum slip. The variation in friction coefficient as well as the usage of a claystone-based value at the locations where claystone is present will locally result in less stable situations as a lower friction coefficient is destabilizing.

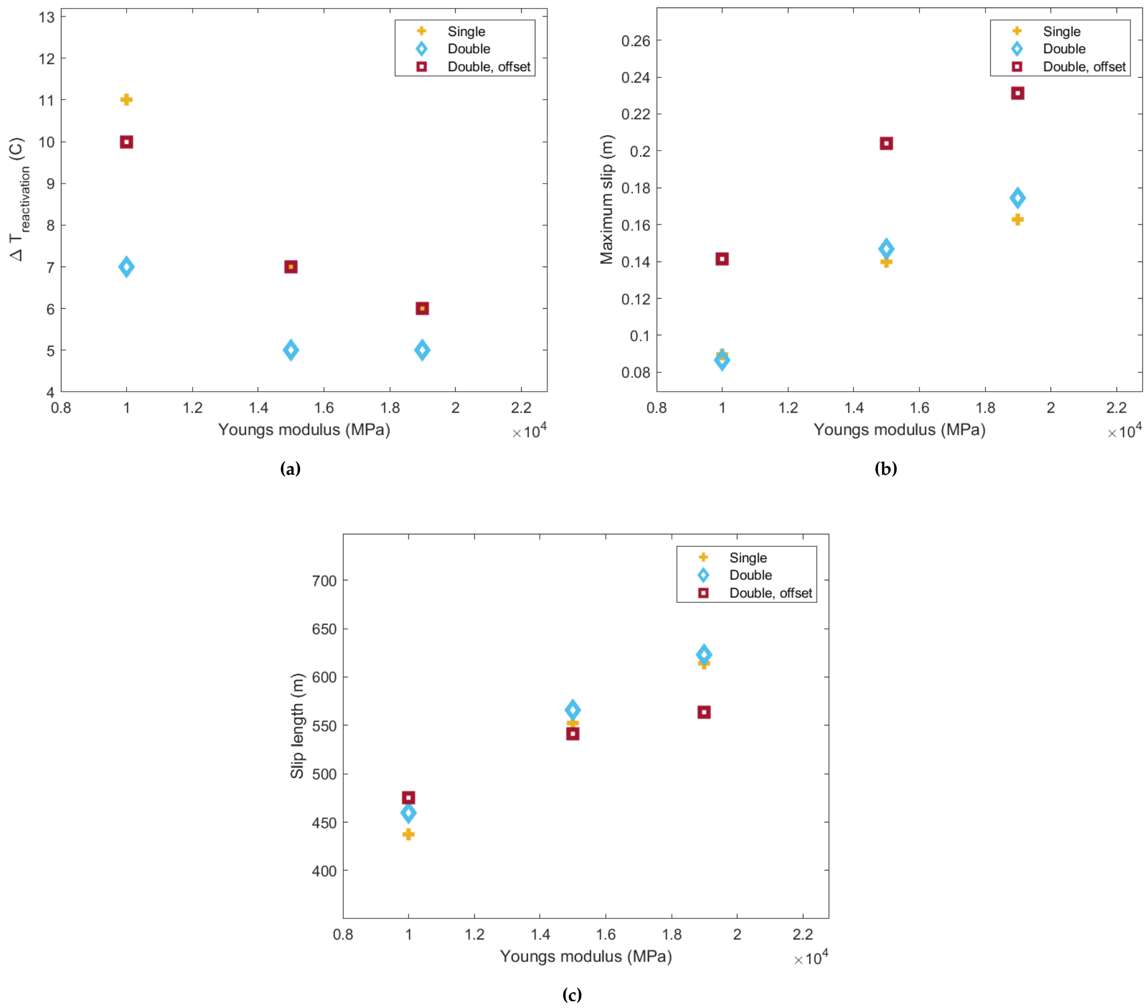

Figure 9.1: Varying young's modulus against three metrics for each model scenario

9.2. Static friction coefficient against the metrics

Similar to the Young's Modulus, the amount of cooling needed for reactivation is between 5 to 10 ° lower than without variations in friction coefficient. A striking feature is the trend of the blue diamonds (double sided, no offset). Even for higher friction coefficients the reactivation temperature difference remains around 5 degrees. It could be argued that the low friction coefficient in the base and seal have a larger effect on stress changes than an increase in friction coefficient in the reservoir, or the fault reactivates outside of the reservoir compartment and therefore a larger friction coefficient in the reservoir has little effect.

The trends seen in the maximum slip plot are similar to the case without heterogeneous friction, although the maximum slip is slightly higher in the case including variations in frictional properties along the fault plane. The exact same applies for the slip patch length results. For this parameter the single sided cooling remains the most sensitive to changes in static friction coefficient.

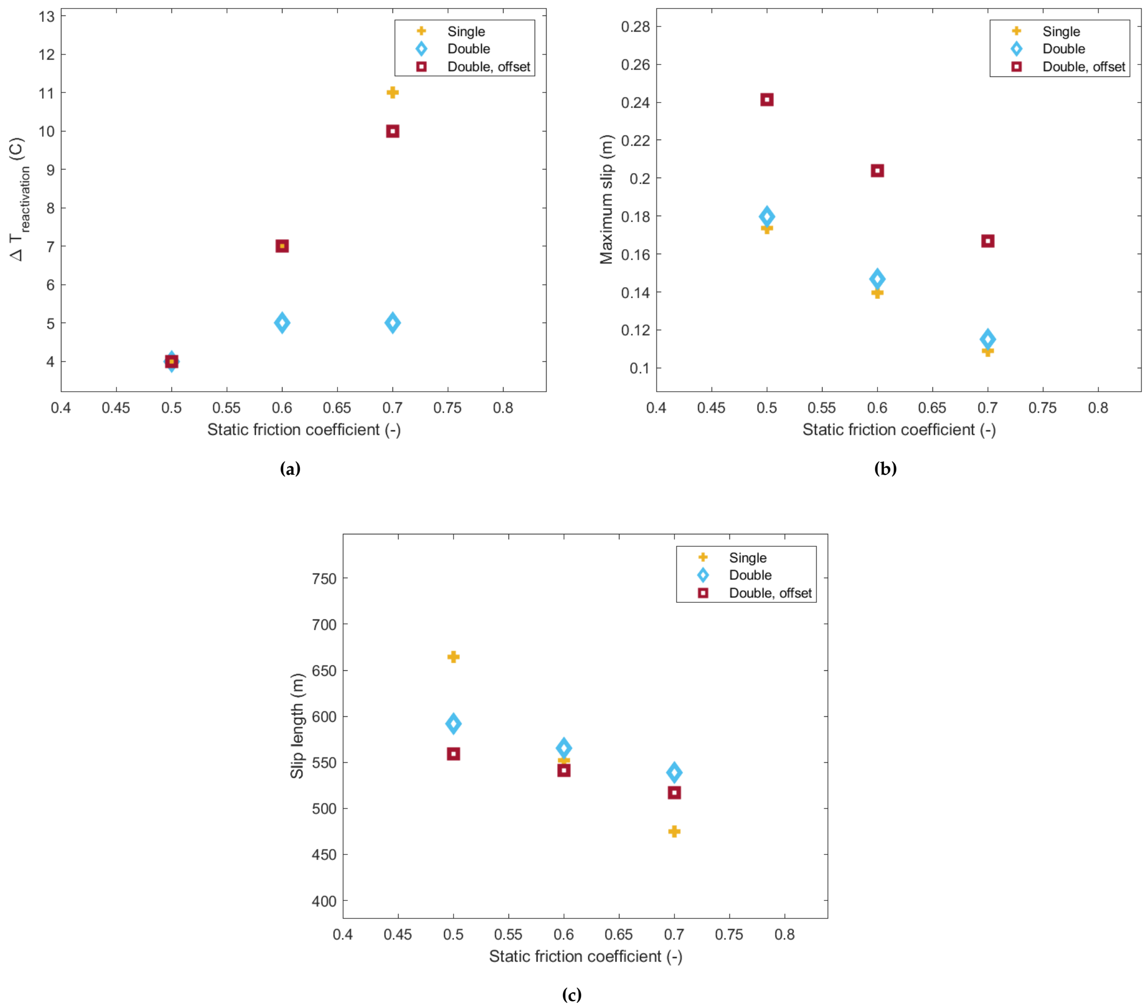

Figure 9.2: Varying static friction coefficient against three metrics for each model scenario

9.3. Thermal expansion coefficient against the metrics

As was also seen in the other two temperature change plots, the reactivation temperature change decreases due to the addition of heterogeneous friction with the double sided cooling scenario without fault offset being the first to reactivate. The maximum slip does shows the same trends as for the previously discussed parameters, again the difference is that there is a slightly higher maximum slip. The slip patch length plot indicates an increase in length compared to the case without heterogeneous slip.

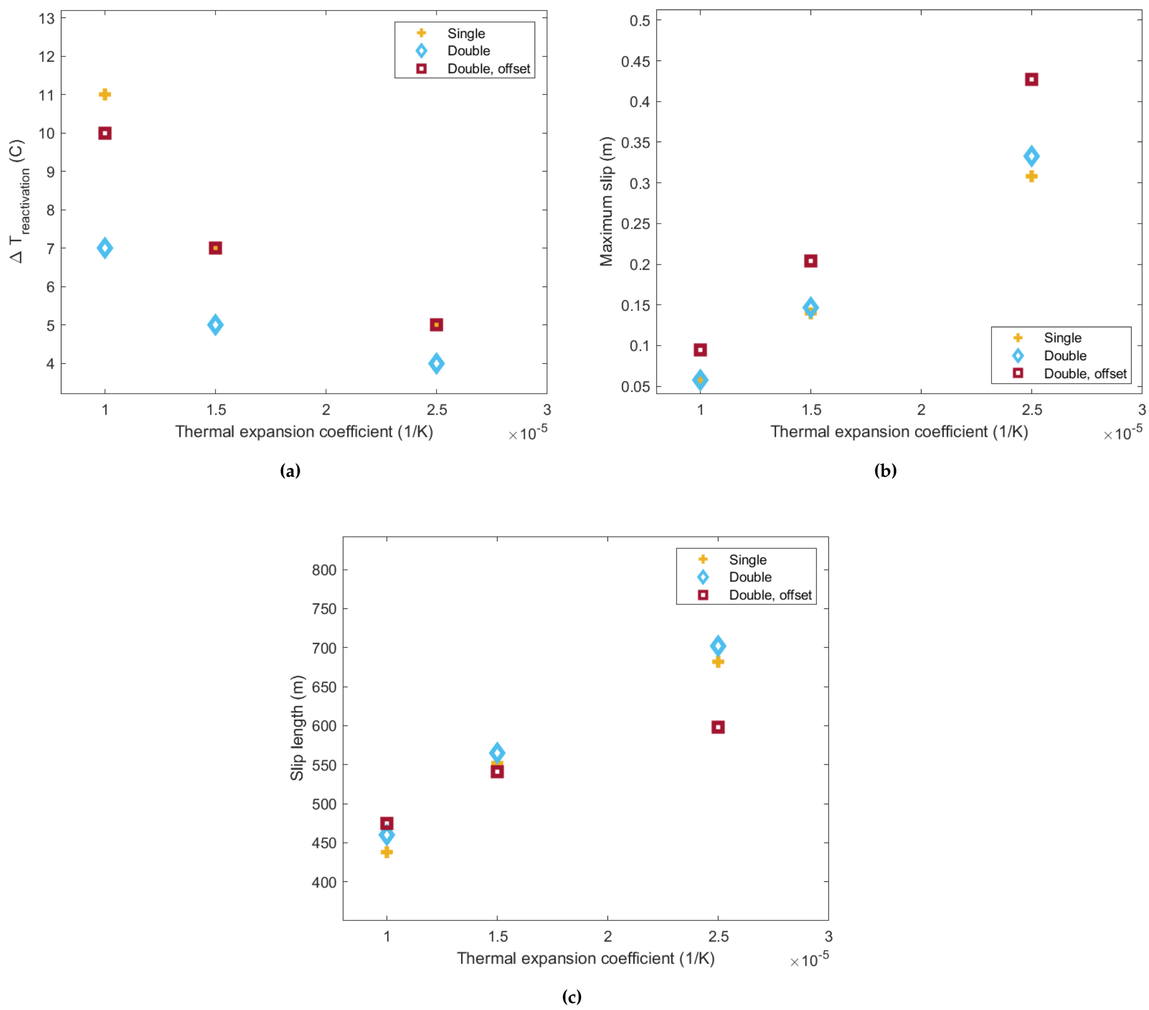

Figure 9.3: Varying thermal expansion coefficient against three metrics for each model scenario

9.4. Ratio sh/sv against metrics

All trends are similar to those previously described in the temperature change and maximum slip plots. The slip patch length is most sensitive in the case of single sided cooling, but all three model scenarios show relatively comparable behaviour.

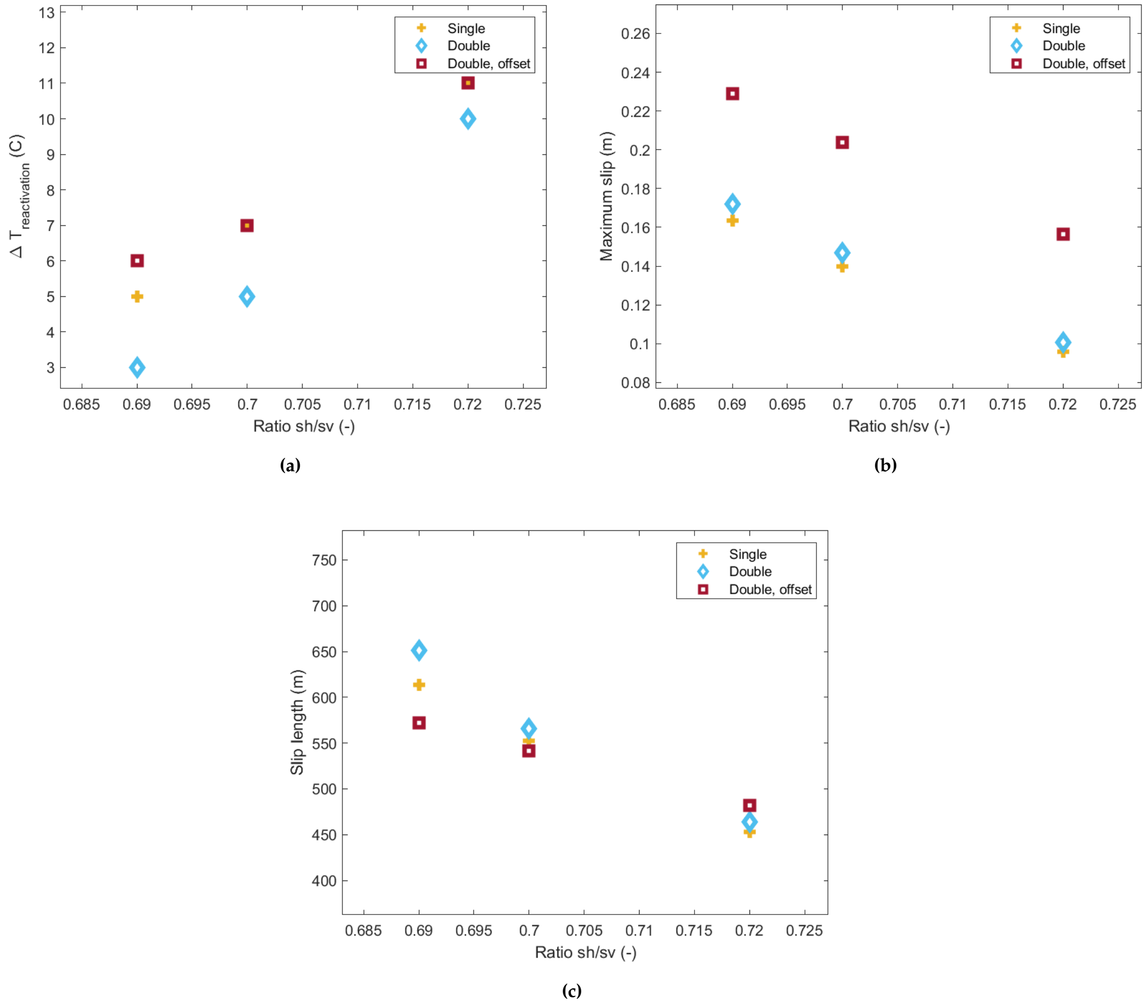

Figure 9.4: Varying sh/sv ratio against three metrics for each model scenario

9.5. Conclusion inclusion heterogeneous friction

The inclusion of heterogeneous friction decreased the temperature change needed for reactivation and increased both the maximum slip experienced by the fault and the slip patch lengths. This was as expected as there are now regions with a lower friction coefficient than before, which has a destabilizing effect on the fault.

10
Discussion

The results from the base case showed that the presence of fault offset results in a larger amount of maximum slip, and that this occurs along the reservoir-reservoir juxtaposed section. The shear stress concentrations are specifically located at the top of the hanging wall and the base of the footwall. Similarly, the double sided model scenario without fault offset experiences shear stress concentrations at these locations, but to a lesser extent and distributed along a longer section of the fault. The fault offset places the stress concentrations closer together, and the overlapping stress concentrations promote more aseismic fault slip. In the single sided cooling scenario, the shear stress concentrations reach a similar level, but only at the top of the hanging wall.

The sensitivity analysis indicated that the key parameters influencing stress changes and fault slip within the realistic value range are the Young's modulus, thermal expansion coefficient, static friction coefficient and the sh/sv ratio. A high stiffness of the rock affects the stress changes on the fault more, and more shrinkage per degree of cooling has the same effect. A decrease in static friction coefficient means that the Mohr-Coulomb failure line becomes less steep and the fault reactivates sooner for a leftward shift or growth of the Mohr-Coulomb circle. The larger the difference in the minimum horizontal and vertical stresses, the more slip on the fault, as is to be expected in a normal faulting regime. The first two were expected as they are part of the thermoelastic stress path parameter. The effect of the friction coefficient and sh/sv ratio were also referred to in other research as important parameters (Hofmann et al., 2024) (L. Buijze, van Bijsterveldt, et al., 2019).

The metrics (with homogeneous friction) showed that the model scenario containing a fault with offset consistently needed the least amount of cooling before reactivating. A similar trend is observed in the case of depletion induced fault reactivation and can be attributed to local stress concentration build up (L. Buijze et al., 2021) (Van den Bogert & van Eijs, 2020) (L. Buijze et al., 2017) (L. Buijze, Van den Bogert, et al., 2019). The resulting maximum slip, occurring at the sandstone-sandstone juxtaposed section as seen in the base case results, is also consistently highest. In terms of slip patch length there was no scenario which repeatedly generated the longest or shortest slip length. However, the slip patch length of the single sided cooling scenario is the most sensitive to changes in the key parameters. The longest slip length occurs for more critical values of the parameters in this case. At the other end of the value range, for more stabilizing values, the fault offset model scenario shows the longest slip patch length. For the same value of the key parameters, the temperature changes needed for fault reactivation are relatively similar for the three model geometries, generally within a range of 2 °C. Therefore, across the three model geometries the degree of cooling needed for reactivation is not hugely different, but the subsequent slip length and maximum slip of all three model scenarios are within a larger range.

One of the main questions that remained open after the above-discussed results was related to the effect of heterogeneous friction. The previously obtained results are all based on the assumption that the whole model has a single, sandstone-based friction coefficient. In reality, the reservoir and the surrounding rock have different frictional properties and within these media a certain degree of variation will exist as well. The incorporation of varying frictional properties along the fault plane is a valuable addition to the model and gives insight into the effect of realistically present features. The inclusion of heterogeneous friction made the fault across all scenarios more destabilized. The temperature decrease needed for fault reactivation was significantly lower (5 - 10°C) and both the maximum slip as well as the slip patch lengths increased. These results coincide with the expectations, as the claystone-based friction coefficient now given to certain regions which were originally populated with a higher, sandstone-based friction coefficient is more destabilizing. A finding that stood out from the metrics including friction variations was that the double sided cooling without offset now reactivates for the smallest temperature drop. This could be due to the fact that in this model scenario the lowest, claystone-based friction coefficient value is used at the location closest to the stress concentrations. In the single sided cooling case the friction coefficient used is slightly higher and in the model scenario with offset the low claystone-based friction coefficient is used in a region further away from the stress concentrations forming at the structural interfaces. The presence of clay in the fault gouge has been found to lubricate the fault, making it slip as a result of lower stress changes compared to coarser material, but with aseismic slip rather than seismic (Niemeijer & Spiers, 2005). However, the minimum horizontal stress tends to be slightly higher, especially at depths greater than 2 kilometers (Bakx, Wassing, & Buijze, 2022). This means that the sh/sv ratio takes on a more stabilizing value and since this study found this ratio to be a key parameter influencing stress changes, its effect could be important to keep in mind for future research.

A source of uncertainty in the data originates from the fault interpretation. PanTerra estimated the nearby fault to be at a distance of 350m, instead of the 450m Stefan Peeters interpreted, which means the cold front would reach the fault sooner. Therefore, the temperature at the fault after 35 years of injection will be lower than used in this work, meaning that the fault could be reactivated sooner. However, PanTerra also deviated from the interpretation used here in terms of the dip angle of the fault, a steeper fault of 75°is assumed by PanTerra. The results from the sensitivity analysis indicated that a fault with this dip angle is more stable than the 65°used in the Pijnacker base case.

The addition of heterogeneous friction to the model proved to be of great influence, therefore it would be interesting to expand on the understanding of the effect of variations in frictional properties on smaller scales. The Delft Sandstone Member, Alblasserdam Member and Rodenrijs Claystone Member are not pure sandstone or claystone but contain other lithologies as well. Gradual changes in frictional properties could be added to coincide with transitions and variations between and within the formations. Although the goal of this thesis is not to make a geologically representative model but to evaluate the effect of juxtaposition of sandstone and claystone, the incorporation of heterogeneities and evaluation of their effect would be an interesting extension in future research.

A limitation of this work is the exclusion of a contrast of properties between the reservoir and the surrounding rock. When elastic properties differ, additional stress concentrations tend to develop (Fokker et al., 2023), which has been found to promote fault reactivation in case of depletion (Mulders, 2003). As this study does not include these property contrasts, the results might underestimate the stress concentrations at the structural interfaces. A solution could be incorporating variations in properties through a similar method as used in this thesis for heterogeneous friction. Another limitation of the used model is the uniform temperature distribution over the reservoir compartments. In reality, the cold front will be coldest at the injection point and the temperature would gradually increase outwards until it reaches the original reservoir temperature. The temperature change used in the model was determined by calculating the radius of the cold front after 35 years of cold water injection, pinpointing the temperature at the presumed distance of the fault and prescribing this temperature to the whole reservoir. This introduces an overestimation of the temperature change in the footwall and an underestimation of the temperature change in the hanging wall.

An important note is that this thesis studies aseismic slip and does not investigate the seismic potential as a result of slip. Besides that, the model is not geologically representative. Thereforec, nothing can realistically be said about a potential seismic hazard. Although Panther is a simplistic model, it is very well applicable to the purpose of this thesis while omitting extra model complexity.

11
Conclusions and future research

This master thesis investigated the effect of juxtaposition of sandstone and claystone formations across faults on thermo-elastic stress changes and induced fault slip in geothermal projects targeting porous sandstone reservoirs.

This study shows that fault offset promotes the onset of fault reactivation due to cooling induced stress changes. The model scenario with double sided cooling (i.e., cooling in both hanging and footwall) with fault offset is the most unstable, needing the least amount of cooling before the onset of fault reactivation occurs (in the homogeneous friction case) and experiencing the largest amount of slip. The maximum slip occurs along the sandstone-sandstone juxtaposed section of the fault. In the double sided cooling case without fault offset the maximum slip occurs at the same location but to a lesser extent as the slip patches overlap less, leading to less destabilization. The model geometry experiencing single sided cooling (i.e., only cooling in hanging wall due to a sealing fault or very large offset) appears to be the most stable configuration, needing the largest degree of cooling to reach the onset of reactivation and having the lowest maximum slip. The location of maximum slip is at the top of the hanging wall as shear stress concentrates at that interface. The slip patch length of the single sided cooling case is most sensitive to changes in key parameters. Heterogeneous friction has a destabilizing effect and made the double sided cooling case reactivate the fastest, while the largest maximum slip is still experienced by the fault offset scenario. However, the higher sh/sv ratio expected in the claystone will likely counter this effect, the degree to which this happens needs to be investigated in further research.

The parameters with the highest influence on thermo-elastic stress changes and fault slip were found to be the Young's modulus, thermal expansion coefficient, static friction coefficient and the ratio sh/sv. These findings coincide with other literature on this topic.

These results imply that fault offset should be included when assessing stress changes and fault slip in geothermal projects, if an offset is present in the reservoir of interest, as the degree to which sandstone is juxtaposed against sandstone affects the amount of thermo-elastic stress changes and slip a fault experiences. Not including fault offset will likely underestimate the thermo-elastic stress changes and subsequent induced fault slip.

One topic worth investigating in future research is the fault interpretation, as this would decrease uncertainly around the fault dip angle, distance between the injector and the fault (reservoir width) and reservoir thickness. The latter two also influence the aspect ratio and are therefore significant. Another geology related potentially interesting aspect would be to incorporate heterogeneities in the model. In reality, geological formations are not purely composed of sandstone but will have some clay-rich layers and vice versa. It would be interesting to look into on what scale their effect on stress changes can be noticed. Besides that, the incorporation of contrasting elastic properties between the reservoir, base and seal could be considered. This could be done in a similar fashion as for the heterogeneous friction. It would be an additional step towards a more realistic model scenario. Moreover, more work could be done to look into the evolution of maximum slip and slip patch length in each model scenario. This work only shows the end result after 35 years of cold water injection and 40 degrees of cooling, but comparing the model scenarios at different time steps could be interesting. Even though the model is simplistic, it is able to capture the essential effects needed for this study.

References

Anderson, E. M. (1905). The dynamics of faulting. *Transactions of the Edinburgh Geological Society*, *8*(3), 387–402.

Bakx, E., Wassing, B., & Buijze, L. (2022). Formation, lithology and region-specific minimum horizontal stress field in the netherlands.

Bek, A., Jeftić, G., Strelec, S., & Jug, J. (2021, 12). Influence of shear rate on the soil's shear strength. *Environmental engineering*, *8*, 39-47. doi: 10.37023/ee.8.1-2.6

Blackwell, D. D., & Steele, J. L. (1989). Heat flow and geothermal potential of kansas. *Bulletin (Kansas Geological Survey)*(226), 267–295.

Buijze, A. J. L. (2020). *Numerical and experimental simulation of fault reactivation and earthquake rupture applied to induced seismicity in the groningen gas field* (Doctoral dissertation). Retrieved from `https://doi.org/10.33540/60`

Buijze, L., Fokker, P., & Wassing, B. (2021). Quantification of induced seismicity potential of geothermal operations: analytical and numerical model approaches 2021. *Scientific Report, TNO, Utrecht (Published in the framework of WarmingUp Theme 4B)*.

Buijze, L., van Bijsterveldt, L., Cremer, H., Paap, B., Veldkamp, H., Wassing, B. B., ... Jaarsma, B. (2019). Review of induced seismicity in geothermal systems worldwide and implications for geothermal systems in the netherlands. *Netherlands Journal of Geosciences*, *98*, e13.

Buijze, L., Van den Bogert, P., Wassing, B., & Orlic, B. (2019). Nucleation and arrest of dynamic rupture induced by reservoir depletion. *Journal of Geophysical Research: Solid Earth*, *124*(4), 3620–3645.

Buijze, L., Van Den Bogert, P. A., Wassing, B. B., Orlic, B., & Ten Veen, J. (2017). Fault reactivation mechanisms and dynamic rupture modelling of depletion-induced seismic events in a rotliegend gas reservoir. *Netherlands Journal of Geosciences*, *96*(5), s131–s148.

Buijze, L., & van der Heiden, V. (2024). *Panther repository.* Retrieved from `https://github.com/TNO/PANTHER` (Accessed 16-04-2024)

Buijze, L., Veldkamp, H., & Wassing, B. (2023). Comparison of hydrocarbon and geothermal energy production in the netherlands: reservoir characteristics, pressure and temperature changes, and implications for fault reactivation. *Netherlands Journal of Geosciences*, *102*, e7.

Clark, S. P. (1966). *Handbook of physical constants*. Geological Society of America.

Den Hartog Jager, D. (1996). Fluviomarine sequences in the lower cretaceous of the west netherlands basin: correlation and seismic expression. In *Geology of gas and oil under the netherlands: Selection of papers presented at the 1983 iternational conference of the american association of petroleum geologists, held in the hague* (pp. 229–241).

De Simone, S., Vilarrasa, V., Carrera, J., Alcolea, A., & Meier, P. (2013). Thermal coupling may control mechanical stability of geothermal reservoirs during cold water injection. *Physics and Chemistry of the Earth, Parts A/B/C*, *64*, 117–126.

DeVault, B., & Jeremiah, J. (2002). Tectonostratigraphy of the nieuwerkerk formation (delfland subgroup), west netherlands basin. *AAPG bulletin*, *86*(10), 1679–1707.

Donselaar, M. E., Groenenberg, R. M., & Gilding, D. T. (2015). Reservoir geology and geothermal potential of the delft sandstone member in the west netherlands basin. In *Proceedings world geothermal congress* (pp. 19–25).

Eshelby, J. D. (1957). The determination of the elastic field of an ellipsoidal inclusion, and related problems. *Proceedings of the royal society of London. Series A. Mathematical and physical sciences*, *241*(1226), 376–396.

Evans, K. F., Zappone, A., Kraft, T., Deichmann, N., & Moia, F. (2012). A survey of the induced seismic responses to fluid injection in geothermal and co2 reservoirs in europe. *Geothermics*, *41*, 30–54.

Eyre, T. S., Eaton, D. W., Garagash, D. I., Zecevic, M., Venieri, M., Weir, R., & Lawton, D. C. (2019). The role of aseismic slip in hydraulic fracturing–induced seismicity. *Science advances*, *5*(8), eaav7172.

Fokker, P., Buijze, L., & Pluymaekers, M. (2023). Srima: Background information of the python tool. *TNO Public*. Retrieved from `https://www.nlog.nl/sites/default/files/2023-11/tno2023_r11303_srima_background_information_of_the_python_tool.pdf`

Foulger, G. R., Wilson, M. P., Gluyas, J. G., Julian, B. R., & Davies, R. J. (2018). Global review of human-induced earthquakes. *Earth-Science Reviews*, *178*, 438–514.

Fuchs, S., Förster, H.-J., Norden, B., Balling, N., Miele, R., Heckenbach, E., & Förster, A. (2021). The thermal diffusivity of sedimentary rocks: Empirical validation of a physically based α- φ relation. *Journal of Geophysical Research: Solid Earth*, *126*(3), e2020JB020595.

Geertsma, J. (1973). Land subsidence above compacting oil and gas reservoirs. *Journal of petroleum technology*, *25*(06), 734–744.

Geothermie, S. P., & DAGO, S. W. (2021). Ebn, 2018. masterplan aardwarmte in nederland-een brede basis voor een duurzame warmtevoorziening. *Dutch. Available at https://www. geothermie. nl/images/Onderzoeken-en-rapporten/20180529-Masterplan-Aardwarmte-in-Nederland. pdf, last accessed*, *24*.

GPG. (2017). *Densities of sedimentary rocks.* Retrieved from `https://gpg.geosci.xyz/content/physical_properties/tables/density_sedimentary_rocks.html` (Accessed on 17-04-2024)

Heidbach, O., Barth, A., Müller, B., Reinecker, J., Stephansson, O., Tingay, M., & Zang, A. (2016). Wsm quality ranking scheme, database description and analysis guidelines for stress indicator.

Hincks, T., Aspinall, W., Cooke, R., & Gernon, T. (2018). Oklahoma's induced seismicity strongly linked to wastewater injection depth. *Science*, *359*(6381), 1251–1255.

Hofmann, H., Ji, Y., Cacace, M., Zang, A., Zimmermann, G., & Shapiro, S. (2024). Kem-15 a1 key parameters affecting induced seismicity in geothermal reservoirs across scale. *KEM-15.* Retrieved from `https://kemprogramma.nl/groups/view/401313ed-b831-402c-bc4c-0a27146077d7/research-questions/files/7937210c-ae7f-4049-9b02-e145789dd840`

Hunfeld, L., Niemeijer, A., & Spiers, C. (2017). Frictional properties of simulated fault gouges from the seismogenic groningen gas field under in situ p–t-chemical conditions. *Journal of Geophysical Research: Solid Earth*, *122*(11), 8969–8989.

Hutka, G. A., Cacace, M., Hofmann, H., Mathur, B., & Zang, A. (2023). Investigating seismicity rates with coulomb failure stress models caused by pore pressure and thermal stress from operating a well doublet in a generic geothermal reservoir in the netherlands. *Netherlands Journal of Geosciences*, *102*, e8.

Jaeger, J. C., Cook, N. G., & Zimmerman, R. (2009). *Fundamentals of rock mechanics*. John Wiley & Sons.

Jansen, J., Singhal, P., & Vossepoel, F. (2019). Insights from closed-form expressions for injection-and production-induced stresses in displaced faults. *Journal of Geophysical Research: Solid Earth*, *124*(7), 7193–7212.

Jeanne, P., Rutqvist, J., Dobson, P. F., Walters, M., Hartline, C., & Garcia, J. (2014). The impacts of mechanical stress transfers caused by hydromechanical and thermal processes on fault stability during hydraulic stimulation in a deep geothermal reservoir. *International Journal of Rock Mechanics and Mining Sciences*, *72*, 149–163.

Jeremiah, J., Duxbury, S., & Rawson, P. (2010). Lower cretaceous of the southern north sea basins: reservoir distribution within a sequence stratigraphic framework. *Netherlands Journal of Geosciences*, *89*(3-4), 203–237.

Kirk, S. S., & Williamson, D. M. (2012). Structure and thermal properties of porous geological materials. In *Aip conference proceedings* (Vol. 1426, pp. 867–870).

Kivi, I. R., Pujades, E., Rutqvist, J., & Vilarrasa, V. (2022). Cooling-induced reactivation of distant faults during long-term geothermal energy production in hot sedimentary aquifers. *Scientific reports*, *12*(1), 2065.

Manya, J. J., Antal Jr, M. J., Kinoshita, C. K., & Masutani, S. M. (2011). Specific heat capacity of pure water at 4.0 mpa between 298.15 and 465.65 k. *Industrial & engineering chemistry research*, *50*(10), 6470–6484.

Mathur, B., Hofmann, H., Cacace, M., Hutka, G. A., & Zang, A. (2024). Thermo-hydro-mechanical simulation of cooling-induced fault reactivation in dutch geothermal reservoirs. *Netherlands Journal of Geosciences*, *103*, e1.

Mijnlieff, H., de Vries, S., Jaarsma, B., & Vogelaar, B. (2023). Seismische dreigings- en risicoanalyse voor aardwarmteprojecten in nederland. Retrieved from `https://www.nlog.nl/sites/default/files/2023-11/20230922_hoofdrapport_sdra_aardwarmteprojecten_-_shra_for_geothermal_projects.pdf`

Mijnlieff, H., Obdam, A., van Wees, J., Pluymaekers, M., & Veldkamp, J. (2014). Doubletcalc 1.4 manual english version for doubletcalc 1.4. 3. *TNO: The Hague, The Netherlands*. Retrieved from `https://www.nlog.nl/sites/default/files/6ab98fc3-1ca1-4bbe-b0a2-c5a9658a3597_doubletcalc%20v143%20manual.pdf`

Mijnlieff, H. F. (2020). Introduction to the geothermal play and reservoir geology of the netherlands. *Netherlands Journal of Geosciences*, *99*, e2.

Moeck, I. S. (2014). Catalog of geothermal play types based on geologic controls. *Renewable and Sustainable Energy Reviews*, *37*, 867–882.

Mossop, A. P. (2001). *Seismicity, subsidence and strain at the geysers geothermal field*. Stanford University.

Mulders, F. M. M. (2003). Modelling of stress development and fault slip in and around a producing gas reservoir. Retrieved from `https://repository.tudelft.nl/islandora/object/uuid:be742135-10d7-4d69-bdee-f808b5926065?collection=research`

Muntendam-Bos, A. (2021). Geomechanical characteristics of gas depletion induced seismicity in the netherlands. In *Arma us rock mechanics/geomechanics symposium* (pp. ARMA–2021).

Muntendam-Bos, A. G., Hoedeman, G., Polychronopoulou, K., Draganov, D., Weemstra, C., van der Zee, W., ... Roest, H. (2022). An overview of induced seismicity in the netherlands. *Netherlands Journal of Geosciences*, *101*, e1.

Niemeijer, A. R., & Spiers, C. J. (2005). Influence of phyllosilicates on fault strength in the brittle-ductile transition: Insights from rock analogue experiments. *Geological Society, London, Special Publications*, *245*(1), 303–327.

Orlic, B., & Wassing, B. (2013). A study of stress change and fault slip in producing gas reservoirs overlain by elastic and viscoelastic caprocks. *Rock mechanics and rock engineering*, *46*(3), 421–435.

PanTerra. (2023, June). *Ammerlaan pijnacker gt: Seismic hazard analysis (update).* Retrieved from `https://mijnbouwvergunningen.nl/page/view/56c1cc01-4b0c-46df-8ded-7bc2d607add0/pijnacker-nootdorp-iv`

Parisio, F., Vilarrasa, V., Wang, W., Kolditz, O., & Nagel, T. (2019). The risks of long-term re-injection in supercritical geothermal systems. *Nature communications*, *10*(1), 4391.

Peeters, S. (2024). (Personal communication, 14-05-2024)

Pluymaekers, M., Kramers, L., Van Wees, J.-D., Kronimus, A., Nelskamp, S., Boxem, T., & Bonté, D. (2012). Reservoir characterisation of aquifers for direct heat production: Methodology and screening of the potential reservoirs for the netherlands. *Netherlands Journal of Geosciences*, *91*(4), 621–636.

Racero-Baena, A., & Drake, S. J. (1996). Structural style and reservoir development in the west netherlands oil province. In *Geology of gas and oil under the netherlands: Selection of papers presented at the 1983 iternational conference of the american association of petroleum geologists, held in the hague* (pp. 211–227).

Ruigrok, E., Spetzler, J., Dost, B., & Evers, L. (2019). Veendam event, 09-01-2019. *KNMI Technical report TR-268*. Retrieved from `https://www.knmi.nl/knmi-bibliotheek/publicaties/technisch-rapport`

Segall, P. (1989). Earthquakes triggered by fluid extraction. *Geology*, *17*(10), 942–946.

Segall, P., & Fitzgerald, S. D. (1998). A note on induced stress changes in hydrocarbon and geothermal reservoirs. *Tectonophysics*, *289*(1-3), 117–128.

Segall, P., Grasso, J.-R., & Mossop, A. (1994). Poroelastic stressing and induced seismicity near the lacq gas field, southwestern france. *Journal of Geophysical Research: Solid Earth*, *99*(B8), 15423–15438.

Soltanzadeh, H., & Hawkes, C. D. (2008). Semi-analytical models for stress change and fault reactivation induced by reservoir production and injection. *Journal of Petroleum Science and Engineering*, *60*(2), 71–85.

Soltanzadeh, H., & Hawkes, C. D. (2009). Induced poroelastic and thermoelastic stress changes within reservoirs during fluid injection and production. *Porous media: heat and mass transfer, transport and mechanics*, *27*, 27–57.

Soustelle, V., ter Heege, J., Buijze, L., & Wassing, B. (2022). Thermomechanical parameters of geothermal analogue reservoir sandstones in the west netherlands basin. Retrieved from `https://www.warmingup.info/documenten/thermomechanical-parameters-of-geothermal.pdf`

Terzagi, V. (1923). Die berechnung der durchassigkeitsziffer des tones aus dem verlauf der hydrodynamischen spannungs. erscheinungen. *Sitzungsber. Akad. Wiss. Math. Naturwiss. Kl. Abt. 2A*, *132*, 105–124.

Tesei, T., Collettini, C., Barchi, M. R., Carpenter, B. M., & Di Stefano, G. (2014). Heterogeneous strength and fault zone complexity of carbonate-bearing thrusts with possible implications for seismicity. *Earth and Planetary Science Letters*, *408*, 307–318.

Uenishi, K., & Rice, J. R. (2003). Universal nucleation length for slip-weakening rupture instability under nonuniform fault loading. *Journal of Geophysical Research: Solid Earth*, *108*(B1).

Van Adrichem Boogaert, H., & Kouwe, W. (1993). Stratigraphic nomenclature of the netherlands, revision and update by rgd and nogepa.
(Mededelingen Rijks Geologische Dienst 50: 180 pp.)

Van den Bogert, P. (2015). Impact of various modelling options on the onset of fault slip and fault slip response using 2-dimensional finite-element modelling. *Restricted, Report No. SR*, *15*.

Van den Bogert, P., & van Eijs, R. (2020). Why mohr-circle analyses may underestimate the risk of fault reactivation in depleting reservoirs. *International Journal of Rock Mechanics and Mining Sciences*, *136*, 104502.

Van Eijs, R. (2015). Neotectonic stresses in the permian slochteren formation of the groningen field. *KNMI Scientific Report. Report No. EP201510210531. NAM (Assen)*.

Van Wees, J.-D., Fokker, P. A., Van Thienen-Visser, K., Wassing, B. B., Osinga, S., Orlic, B., ... Pluymaekers, M. (2017). Geomechanical models for induced seismicity in the netherlands: Inferences from simplified analytical, finite element and rupture model approaches. *Netherlands Journal of Geosciences*, *96*(5), s183–s202.

Verweij, J., Boxem, T., & Nelskamp, S. (2016). 3d spatial variation in vertical stress in on-and offshore netherlands; integration of density log measurements and basin modeling results. *Marine and Petroleum Geology*, *78*, 870–882.

Vilarrasa, V., Olivella, S., Carrera, J., & Rutqvist, J. (2014). Long term impacts of cold co2 injection on the caprock integrity. *International Journal of Greenhouse Gas Control*, *24*, 1–13.

Vondrak, A., Donselaar, M. E., & Munsterman, D. (2018). Reservoir architecture model of the nieuwerkerk formation (early cretaceous, west netherlands basin): diachronous development of sand-prone fluvial deposits. *Geological Society, London, Special Publications*, *469*(1), 423–434.

Wassing, B., Candela, T., Osinga, S., Peters, E., Buijze, L., Fokker, P., & Van Wees, J. (2021). Time-dependent seismic footprint of thermal loading for geothermal activities in fractured carbonate reservoirs. *Frontiers in Earth Science*, *9*, 685841.

Weert, A., Ogata, K., Vinci, F., Leo, C., Bertotti, G., Amory, J., & Tavani, S. (2024). Multiple phase rifting and subsequent inversion in the west netherlands basin: implications for geothermal reservoir characterization. *Solid Earth*, *15*(2), 121–141.

Willems, C., Nick, H., Goense, T., & Bruhn, D. (2017). The impact of reduction of doublet well spacing on the net present value and the life time of fluvial hot sedimentary aquifer doublets. *Geothermics*, *68*, 54–66.

Willems, C. J., Vondrak, A., Mijnlieff, H. F., Donselaar, M. E., & Van Kempen, B. M. (2020). Geology of the upper jurassic to lower cretaceous geothermal aquifers in the west netherlands basin–an overview. *Netherlands Journal of Geosciences*, *99*, e1.

Willems, C. J., Vondrak, A., Munsterman, D. K., Donselaar, M. E., & Mijnlieff, H. F. (2017). Regional geothermal aquifer architecture of the fluvial lower cretaceous nieuwerkerk formation–a palynological analysis. *Netherlands Journal of Geosciences*, *96*(4), 319–330.

Winningsplan ammerlaan geothermie. (2019). Retrieved from `https://mijnbouwvergunningen.nl/page/view/56c1cc01-4b0c-46df-8ded-7bc2d607add0/pijnacker-nootdorp-iv` (Revised third time august 2020)

Xiong, J., Lin, H., Ding, H., Pei, H., Rong, C., & Liao, W. (2020). Investigation on thermal property parameters characteristics of rocks and its influence factors. *Natural Gas Industry B*, *7*(3), 298–308.

Zang, A., Hofmann, H., Hutka, G. A., Mathur, B., Cacace, M., Shapiro, S., ... others (2023). Stress and seismicity related to cooling of geothermal wells. In *Isrm congress* (pp. ISRM–15CONGRESS).

Ziegler, P. A. (1990). *Geological atlas of western and central europe.[hauptbd.](1990)*. Shell Internat. Petroleum Maatschappij.

Zoback, M. D. (2010). *Reservoir geomechanics*. Cambridge university press.

A

Sensitivity analysis results

A.1. Sensitivity analysis - hanging wall width

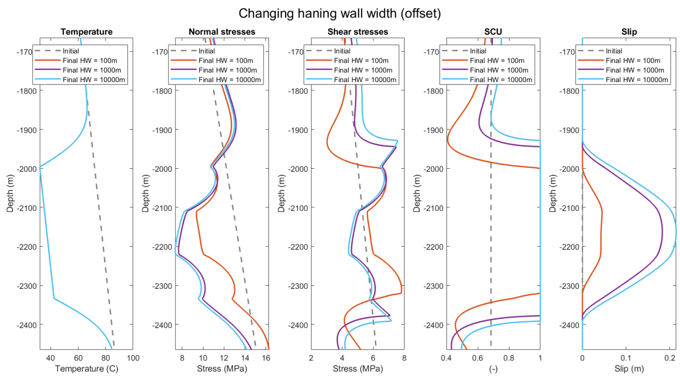

Figure A.1: Sensitivity hanging wall width double sided cooling with offset

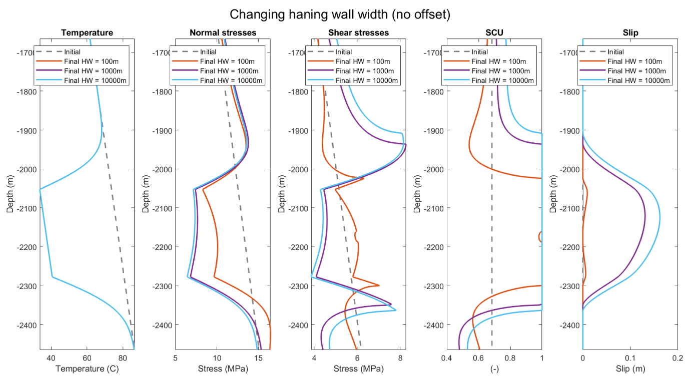

Figure A.2: Sensitivity hanging wall width double sided cooling without offset

A.2. Sensitivity analysis - reservoir thickness

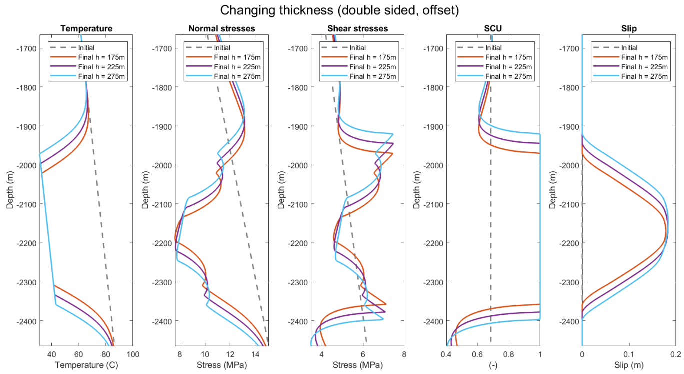

Figure A.3: Sensitivity reservoir thickness double sided cooling with offset

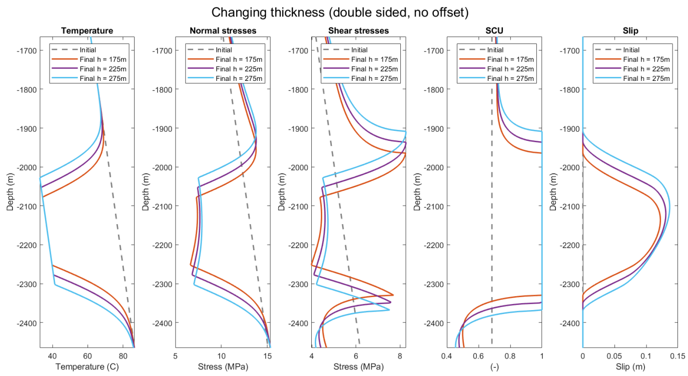

Figure A.4: Sensitivity reservoir thickness double sided cooling without offset

A.3. Sensitivity analysis - dip

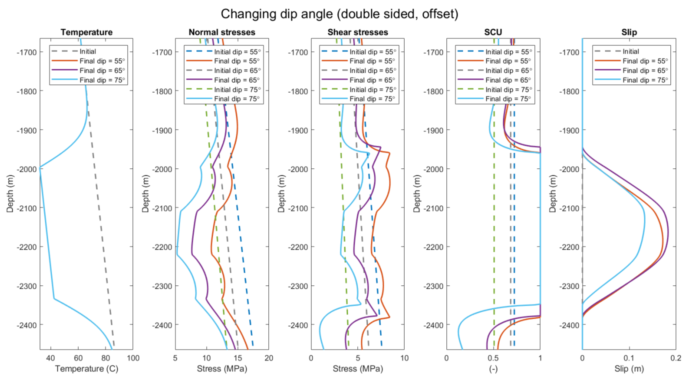

Figure A.5: Sensitivity dip double sided cooling with offset

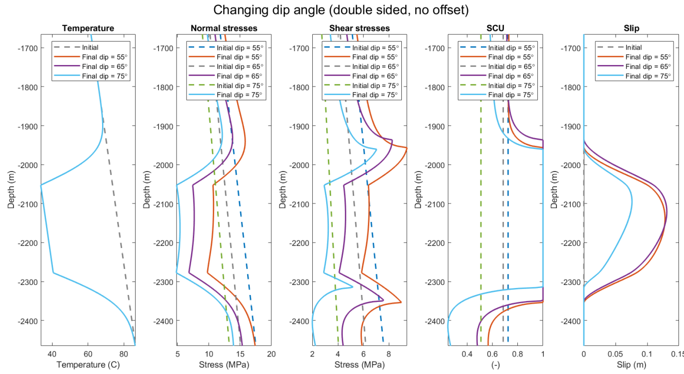

Figure A.6: Sensitivity dip double sided cooling without offset

A.4. Sensitivity analysis - static friction coefficient

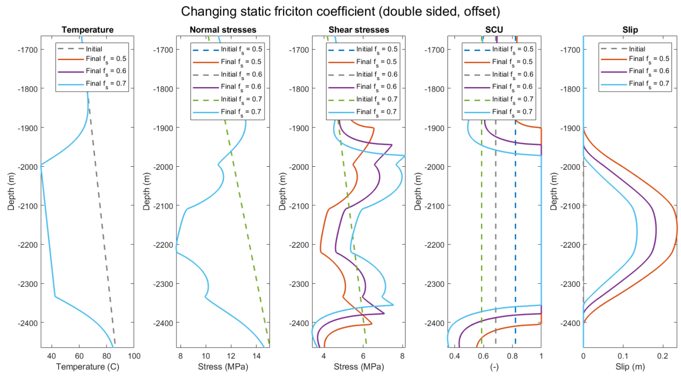

Figure A.7: Sensitivity static friction coefficient double sided cooling with offset

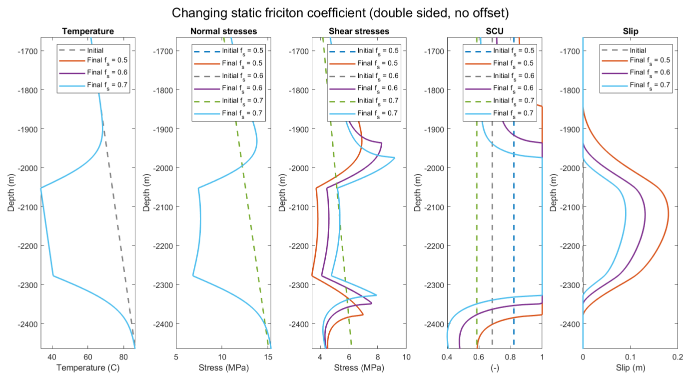

Figure A.8: Sensitivity static friction coefficient double sided cooling without offset

A.5. Sensitivity analysis - cohesion

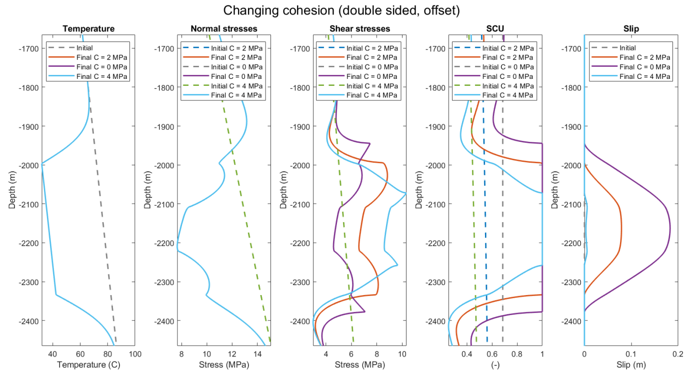

Figure A.9: Sensitivity cohesion double sided cooling with offset

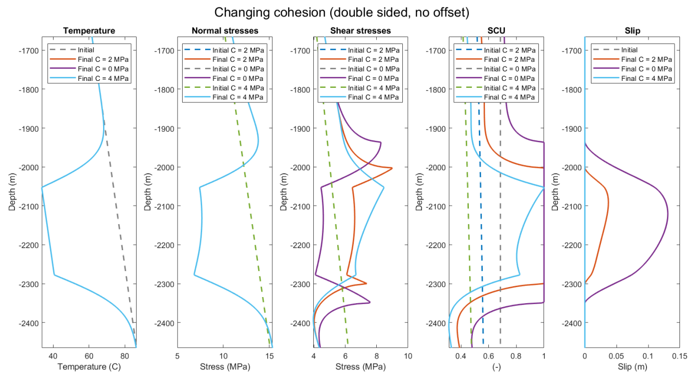

Figure A.10: Sensitivity cohesion double sided cooling without offset

A.6. Sensitivity analysis - Young's modulus

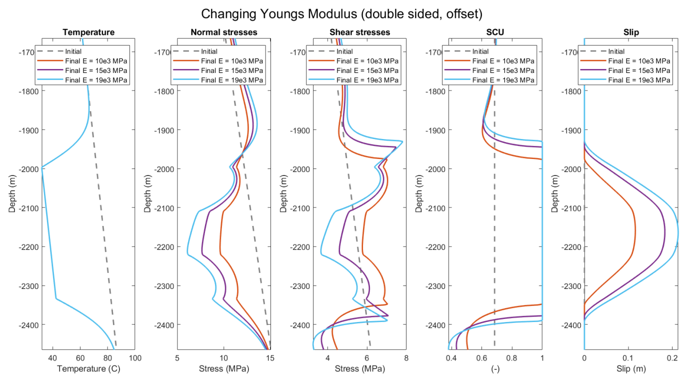

Figure A.11: Sensitivity Young's modulus double sided cooling with offset

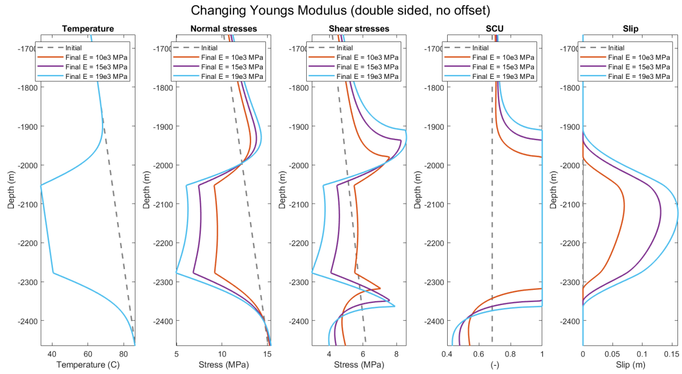

Figure A.12: Sensitivity Young's modulus double sided cooling without offset

A.7. Sensitivity analysis - thermal expansion coefficient

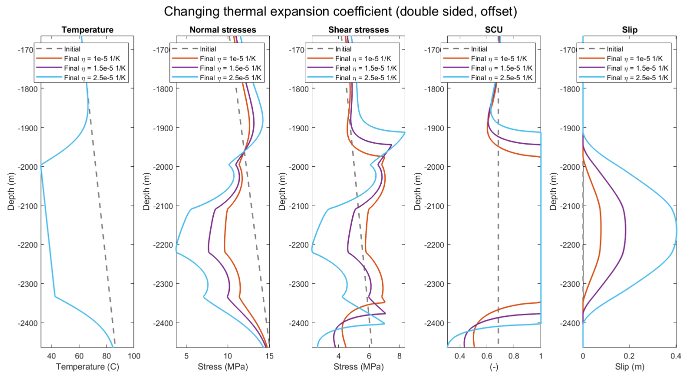

Figure A.13: Sensitivity thermal expansion coefficient double sided cooling with offset

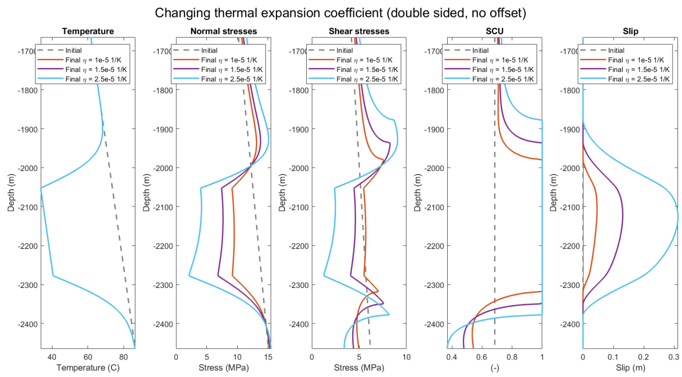

Figure A.14: Sensitivity thermal expansion coefficient double sided cooling without offset

A.8. Sensitivity analysis - Poisson's ratio

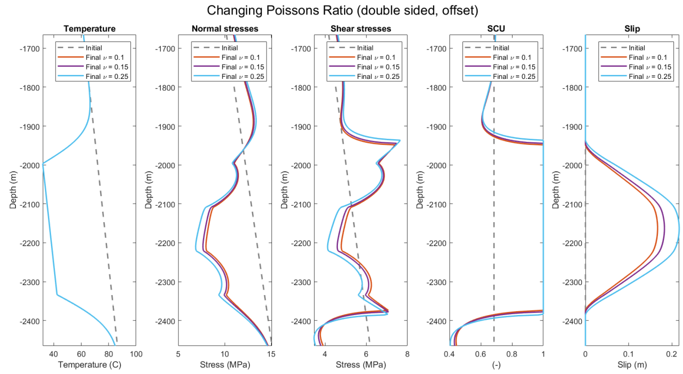

Figure A.15: Sensitivity Poisson's ratio double sided cooling with offset

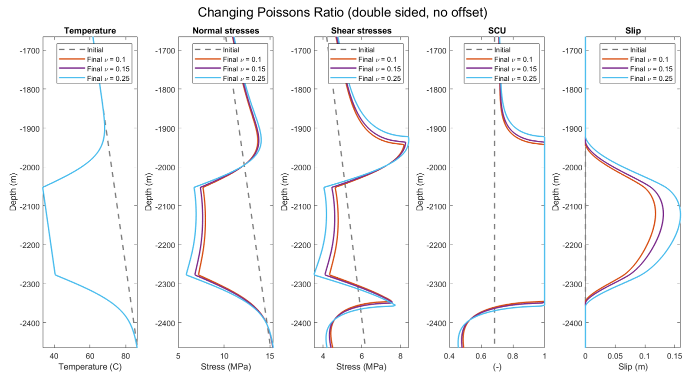

Figure A.16: Sensitivity Poisson's ratio double sided cooling without offset

A.9. Sensitivity analysis - thermal diffusivity

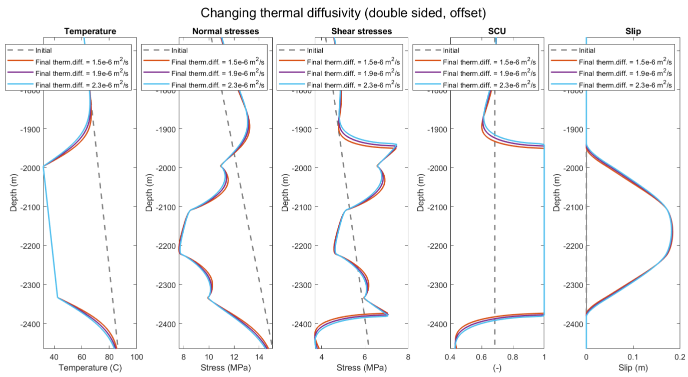

Figure A.17: Sensitivity thermal diffusivity double sided cooling with offset

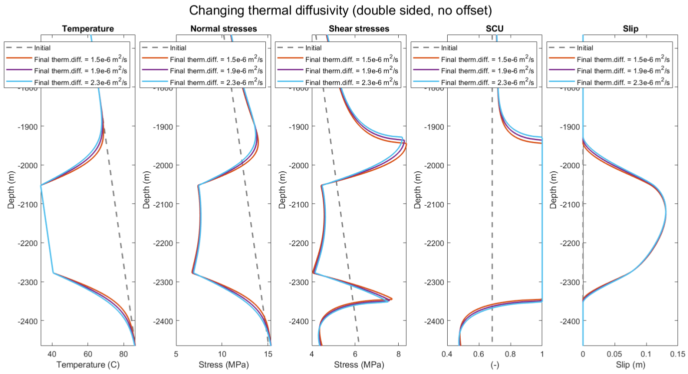

Figure A.18: Sensitivity thermal diffusivity double sided cooling without offset

A.10. Sensitivity analysis - ratio sH/sh

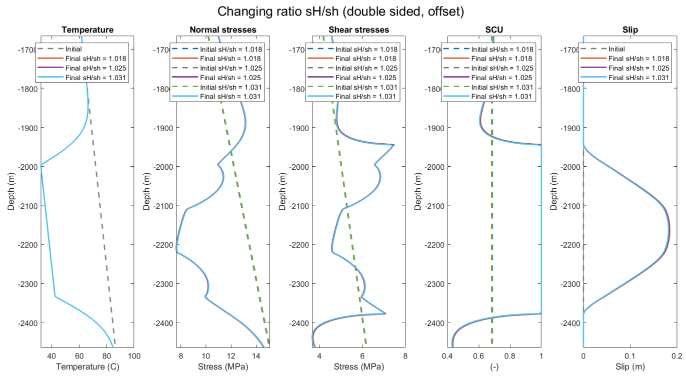

Figure A.19: Sensitivity ratio sH/sh double sided cooling with offset

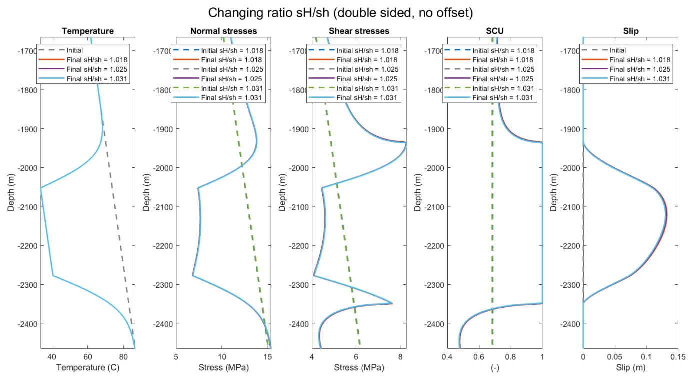

Figure A.20: Sensitivity ratio sH/sh double sided cooling without offset

A.11. Sensitivity analysis - ratio sh/sv

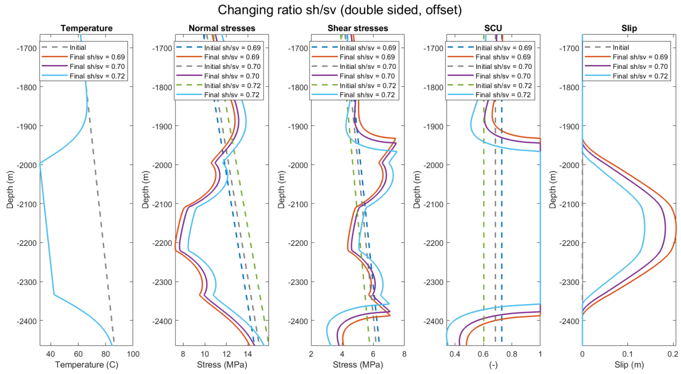

Figure A.21: Sensitivity ratio sh/sv double sided cooling with offset

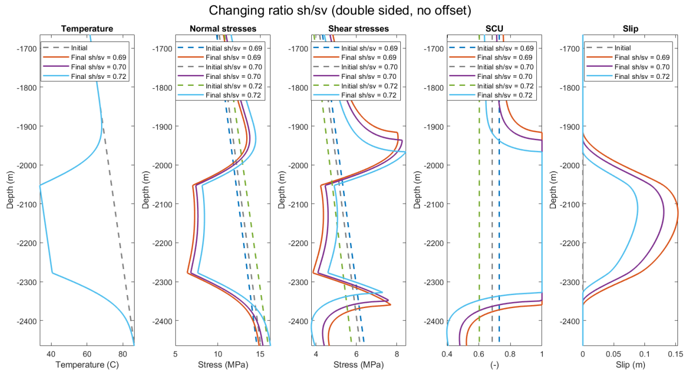

Figure A.22: Sensitivity ratio sh/sv double sided cooling without offset